Observation of the Large Scale Cosmic-Ray Anisotropy at TeV Energies with the Milagro Detector

by

Brian E. Kolterman

A dissertation submitted in partial fulfillment

of the requirements for the degree of

Doctor of Philosophy

Department of Physics

New York University

September, 2008

Thesis Advisor Peter Nemethy

Dedication

This work is dedicated to my mother, Billie Jane Kolterman, and my father, Gerald Kolterman.

Acknowledgements

First, I wish to thank my family and friends for the all of the support I have received over the years. There are too many to name here, but I am lucky to have had so many good people around me.

I also want to extend my gratitude to the members of the Milagro collaboration for all of the advice and assistance they have given me during the evolution of this research. I am especially indebted to my thesis advisor Peter Nemethy. I have learned a great deal from our frequent interactions and cannot thank him enough for my progress over the course of my graduate experience. I also wish to thank Allen Mincer whom I could consider a second advisor. Discussions, sometimes spirited, with both Peter and Allen were indispensable in the completion of this work. I would leave our meetings sometimes feeling smart, sometimes confused, sometimes irritated, but inevitably I would end up having a better understanding both of my work and of what makes a good scientist. For this I thank you both.

Finally, I would like to say I was honored to have professors Peter Nemethy, Allen Mincer, Andrei Gruzinov, David Hogg and Michael Blanton serve on my thesis committee.

Abstract

Cosmic-rays with energies in the range of 1 - 100 TeV are nearly isotropic in their arrival directions due to interactions with randomly scattered inhomogeneities in the Galactic magnetic field. Observation of the large scale anisotropy in the arrival direction of these cosmic-rays is therefore a useful tool in constraining theoretical models of cosmic-ray propagation, probing the magnetic field structure in our interstellar neighborhood, as well as providing information about the distribution of sources. In this work results are presented of a harmonic analysis of the large scale cosmic-ray anisotropy as observed by the Milagro observatory. A two-dimensional display of the anisotropy projections in right ascension is generated by the fitting of three harmonics to 18 separate declination bands.

Milagro is a water Cherenkov detector located at an elevation of 2630m in the Jemez mountains outside of Los Alamos, NM. With a live time $> 90\%$ and a large field-of-view (~ 2 sr), Milagro is an excellent instrument for measuring this anisotropy with high sensitivity at TeV energies.

The analysis is conducted using a seven year data sample consisting of more than 95 billion events. A sidereal anisotropy is observed with a magnitude around 0.1% for cosmic-rays with a median energy of 6 TeV. The dominant feature in this data set is a deficit region of depth $(-2.85 \pm 0.06$ stat. ± 0.08 syst.$) \times 10^{-3}$ in the direction of the Galactic North Pole with a range in declination of -10 to 45 degrees and 150 to 225 degrees in right ascension. The anisotropy also shows evidence of a time dependence, with a steady increase in the magnitude of the signal in this region over the course of seven years. An analysis of the energy dependence of the

anisotropy in this region is also presented showing possible deviation of the spectral index of the anisotropy signal from that of the nominal cosmic-ray background. The anisotropy of cosmic-rays in universal time is analyzed showing a dipole structure at the level of 3×10^{-4}, consistent with the Compton-Getting effect expected due to the Earth's motion around the Sun through the cosmic-ray ether.

Contents

List of Figures

List of Tables

Chapter 1

Introduction

When Victor Hess first discovered mysterious particles coming from outer space back in 1912 it opened a new window on the universe for astronomers. These particles came to be known as cosmic-rays and sparked the fields of particle physics and astrophysics. A great deal is known about cosmic-rays with the main topics being energy spectrum, composition and asymmetries in arrival direction (or anisotropy). However, there are still unanswered questions. The specific origins of these cosmic-rays are still a mystery and there are also questions about cosmic-ray propagation. In addition, since cosmic-rays are charged particles, they can be used as a probe of magnetic field structures not normally observable by other means. Answering these questions requires utilizing detailed measurements of the different aspects of cosmic-rays mentioned above. In an attempt to add to this knowledge, presented in this work is an analysis of the large scale cosmic-ray anisotropy.

1.1 Galactic Cosmic-Rays

1.1.1 Brief Overview

Cosmic-rays are observed over a wide range of energies from a couple MeV to more than 10^{20} eV. The energy spectrum of cosmic-rays has been extensively studied. Figure 1.1 shows the nominal cosmic-ray spectrum as observed on Earth.

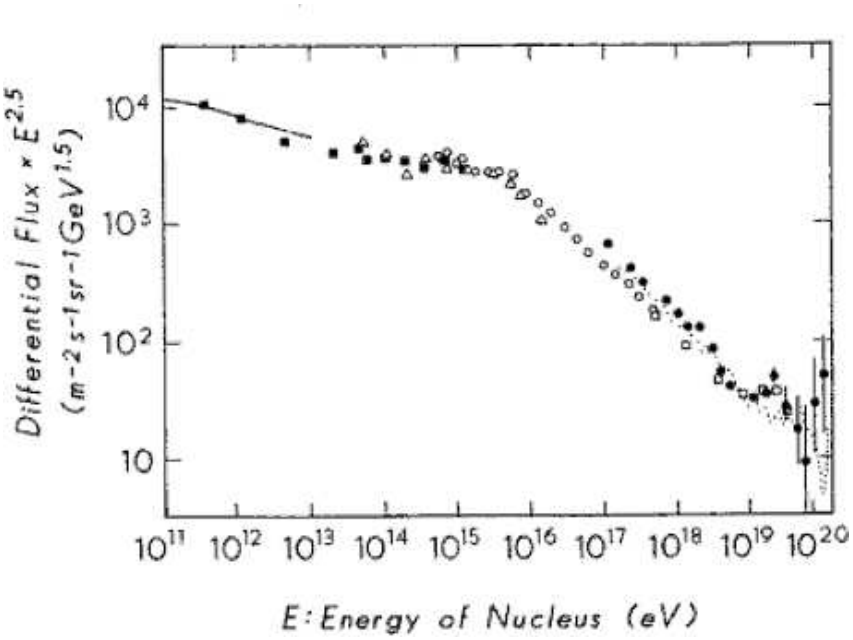

Figure 1.1: Differential nominal cosmic-ray spectrum. The slope is flattened by multiplying the flux by $E^{2.5}$. Figure taken from [1]

The lowest energy cosmic-rays can be produced by the Sun or originate from outside the solar system. The highest energy cosmic-rays are of unknown origins as of yet. Given that the rate of particles with energies $> 10^{19}$ eV reaching the Earth is about one per square kilometer per century, it is difficult to collect enough of them to tell where they came from with any statistical power, although currently it is

suspected that these cosmic-rays are from extragalactic sources. Cosmic-rays with energies up to about 10^{17} eV are believed to be almost entirely of galactic origin.

Galactic cosmic-rays (henceforth abbreviated as CRs) have an average energy density of $\sim 1 eV cm^{-3}$, similar to the energy density of interstellar radiation and magnetic fields [6]. For this reason, these CRs play an important part in the dynamics of the interstellar medium. The focus of this work is on cosmic-rays of energies between about 0.5 TeV to a couple hundred TeV and is the energy range to be assumed if not explicitly mentioned.

Another important aspect of CRs, which has been studied in detail, is the composition of cosmic-rays. About 98% of CRs are fully ionized nucleons (mainly protons) with the other 2% being electrons and positrons. Studies of the nuclear component involve determining both the elemental composition and the isotopic abundances of different particle species (as well as their energy spectra). The information gathered from these studies are indispensable for understanding the origin, acceleration, and propagation of CRs. One example, relevant to the isotropy observed in cosmic-rays, is the average time a CR spends in the galaxy before escaping. This can be determined from isotopic abundances of radioactive nuclei and is found to be on the order of 10 million years. For a detailed review of this subject see [7].

Sources of CRs at these energies are not entirely known. There a number of probable candidates for accelerators of CRs that have been studied including: supernovae, supernova remnants, and pulsars (see [8] for a detailed discussion). The main obstacle to determining the acceleration sites is the fact that the path of CRs, being charged particles, bend in the Galactic magnetic field. Therefore, the arrival

direction of a CR does not directly point back to its source. Information about the location of possible CR accelerators can be obtained through a combination (an exceedingly difficult one at that) of the CR energy spectrum and composition information, understanding of CR propagation, and cosmic-ray anisotropy.

1.1.2 Propagation and Isotropy

The propagation of CRs for a particular particle species can be written as [9]:

$$\frac{\partial \psi(\vec{r},p,t)}{\partial t} = q(\vec{r},p,t) + \vec{\nabla}\cdot(D_{xx}\vec{\nabla}\psi - \vec{V}\psi) + \frac{\partial}{\partial p}p^2 D_{pp}\frac{\partial}{\partial p}\frac{1}{p^2}\psi - \frac{\partial}{\partial p}[\dot{p}\psi - \frac{p}{3}(\vec{\nabla}\cdot\vec{V})\psi] - \frac{1}{\tau_f}\psi - \frac{1}{\tau_r}\psi \quad (1.1)$$

where $\psi(\vec{r},p,t)$ is the CR density per unit of total particle momentum p at position $\vec{r}$, $q(\vec{r},p)$ is the source term containing contributions of the particle's sources, other particle species decays, and spallation, D_{xx} is the spatial diffusion coefficient, $\vec{V}$ is the convection velocity, D_{pp} is the diffusion in momentum space (as can occur in CR reacceleration due to interactions with plasma waves during propagation), $\dot{p}$ is the rate of momentum gain (or loss), τ_f is the characteristic time scale for loss by fragmentation, and τ_r is time scale for radioactive decay.

Some of the factors in this equation are known, such as the spallation cross-sections, decay times, and gas densities (which can be obtained from atomic and molecular gas surveys). Others are model dependent. The source distribution and particle species abundances, for example, require an iterative technique to compare calculations using a given model with observational data.

The diffusion tensor plays an important role in CR propagation and partly encodes details of the magnetic field structures. The diffusion of CRs arises from the scattering of particles on random magnetohydrodynamic discontinuities and waves distributed throughout the Galaxy. Locally, the spatial diffusion follows along magnetic field lines and can therefore be very anisotropic. On large scales of ~ 100 pc, fluctuations in the random magnetic field can be much larger than the average field strength ($\sim 1\mu g$). Since CRs spend on the order of 10^7 years propagating in the Galaxy, these random fluctuations lead to a large degree of isotropy on these distance scales. The typical values of the diffusion coefficient (assuming an isotropic tensorial structure) for relativistic particles is $\sim 10^{29} cm^2/s$ as determined from analysis of CR composition data [10]. The diffusion coefficient can also be energy dependent, varying depending on the theoretical model.

1.2 Cosmic-Ray Anisotropy

1.2.1 Diffusion and Source Distribution

In the diffusion approximation, the amplitude of the anisotropy is dependent on the spacial gradient of the number density of cosmic-rays and can be calculated as [11]:

$$A = \frac{3D}{v}\frac{\nabla N}{N} \tag{1.2}$$

where D is the diffusion tensor, N is the number density of cosmic-rays, and v is the velocity of the cosmic-rays (which at these energies is essentially c). The diffusion tensor is generally assumed to be isotropic in practical calculations; there

is no reason for this to be true but, lacking detailed knowledge of the structure of the local Galactic magnetic field, it cannot be calculated explicitly. The isotropic approximation is reasonable on scales larger than ~ 100 parsecs due to randomness in the large-scale Galactic magnetic fields.

Anisotropy caused by a gradient in CR density can arise from diffusion of cosmic-rays into the Galactic halo, the distribution of cosmic-ray sources and interactions with local magnetic field configurations.

The diffusion of CRs into the Galactic halo can be examined using the three-dimensional diffusion equation. This can take into account the spatial distribution of atomic and molecular gas clouds, CR sources, and convection [12]. A simplified model of the galaxy is as a thin disk with a uniform distribution of interstellar gas and CR sources. Surrounding the disk is a halo with a much smaller density of matter and sources and in general will have a higher diffusion coefficient. Cosmic-rays produced in the Galactic disk will tend to diffuse out into the Galactic halo creating an anisotropy in the direction perpendicular to the disk. This can be approximated by [11]:

$$A_{halo} = \frac{3zn_g}{x_l} \tag{1.3}$$

with z equal to the perpendicular distance from the Galactic disk, n_g the density of gas in the disk ($\sim 1cm^{-1}$), and x_l the average thickness of interstellar matter passed through by the CRs ($\sim 3\times 10^{24}cm^{-2}$). Using $z \approx 10$ pc gives an anisotropy on the order of 10^{-5} but it is noted that this approximation does not take into account the particular magnetic field configurations, source distributions, or asymmetries in

the size of the Galactic halo between the Northern and Southern hemispheres, all of which complicate this calculation.

The density of CR sources is expected to be higher in the plane of the Galaxy. The exact calculation of the anisotropy due to these sources is not possible without knowing the specific distribution, intensity, and age of the sources but, some simple approximations have been examined. Using the isotropic diffusion model, a number of studies have been conducted predicting the anisotropy arising from a distribution of possible cosmic-ray sources such as supernova remnants and pulsars near the Earth (for details see [13], [14], and [15]). In these studies a more sophisticated simulation of the diffusion process is conducted including escape of CRs from the Galaxy through the halo, reacceleration of CRs, and discrete known source candidates. In general these simulations tend to over estimate the anisotropy but are within an order of magnitude of observations ($\sim 10^{-3}$). In addition the possible sources found to be the most important for producing an anisotropy similar to observations lie within about 1-2 kiloparsecs from Earth.

1.2.2 Heliospheric Magnetic Fields

Since CRs at energies of 1-100 TeV tend to propagate along the local magnetic field, there is expected to be an enhancement coming from the direction of the heliotail. The heliotail is the part of the heliosphere opposite to the Sun's direction of motion formed from the interactions between the solar wind, interstellar plasma, and interstellar and interplanetary magnetic fields. Figure 1.2 shows the shape of the magnetic field lines in the heliosphere. As is seen, the magnetic field lines become more parallel in the direction of the heliotail. This could allow more cosmic-rays

to propagate from this direction rather than from directions where the CRs would have to propagate perpendicular to the magnetic field.

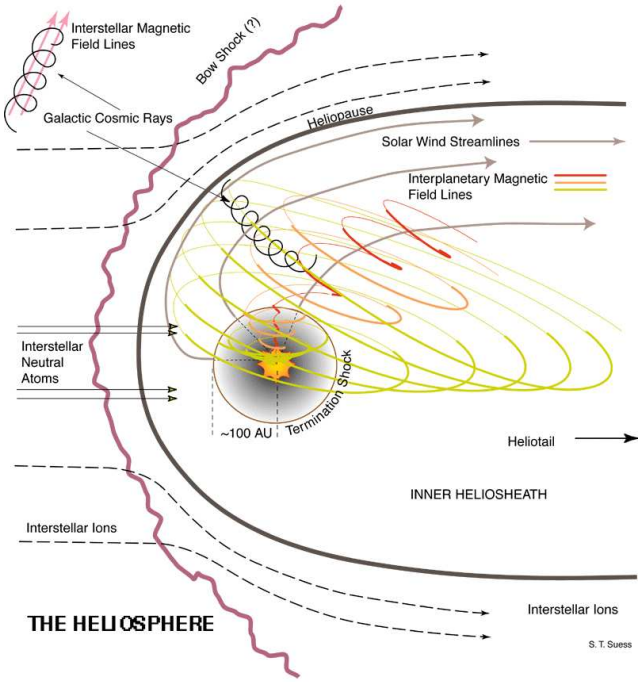

Figure 1.2: Schematic view of the magnetic field structures of the heliosphere. Figure taken from [2].

The magnetic fields in the heliosphere are not large enough to significantly modulate CRs at TeV energies. The gyroradius for a TeV particle in the local magnetic field is around 0.1 pc (or 100 AU), approximately the size of the heliosphere. However, according to a recent derivation of the diffusion tensor [16], it appears that perpendicular diffusion can become significant. This could have implications for the modulation of TeV cosmic-rays in the outer heliosphere due to the changes in the heliosphere coming from varying solar output (e.g. the 11 year solar cycle). At this point in time, understanding how this could arise requires more theoretical

work and simulations of the heliosphere.

1.2.3 Compton-Getting Effect

In addition to the spatial gradient leading to anisotropy, there is also the momentum gradient. In 1935 Arthur Compton and Ivan Getting proposed a theory of cosmic-ray anisotropy based on the motion of the Earth through space [17]. Assuming an isotropic and homogeneous cosmic-ray sea in the vicinity of the solar system, this anisotropy would manifest as a dipole with a maximum in the direction of motion. Figure 1.3 shows a schematic view in the case of the Earth's motion around the Sun.

The anisotropy, defined as the fractional difference from the mean cosmic-ray rate, is calculated to be [18] (assuming the observer's speed is small compared to the speed of the light):

$$A(\theta) = (2+\alpha)\frac{v}{c}cos(\theta) \tag{1.4}$$

where θ is the angle between the direction of the Earth's motion and the CR arrival direction, α is the spectral index of the CRs, v is the speed of the Earth relative to the isotropic CR background, and c is the speed of light. It is noted that although this effect is dependent on the spectral index of the CRs, it is not dependent on their specific energies.

In the case of the Earth's motion around the Sun, $v = 29$ km/s, an using a value of $\alpha = 2.7$, the anisotropy is expected to be of the order of 10^{-4}. Also necessary to consider is the variation in magnitude and direction of the anisotropy due to the Earth's tilt on its axis and orbital eccentricity.

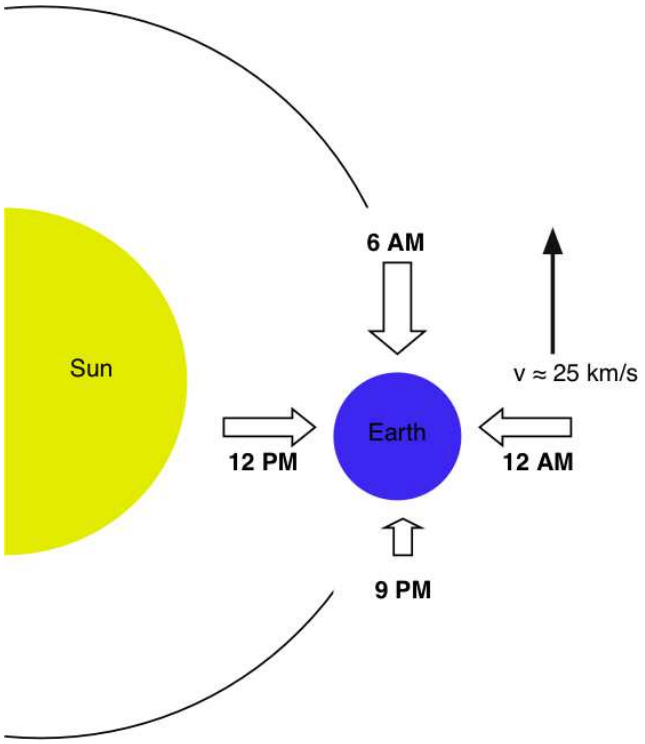

Figure 1.3: Schematic picture of the Compton-Getting effect due to the Earth's motion around the Sun. The size of the arrows indicates the magnitude of the cosmic-ray flux.

This calculation may also be done for the motion due to the solar system around the Galactic center. In this case there is the possibility that the CR sea co-rotates with the local Galactic magnetic fields. This complicates the prediction of this effect. But, one can make an estimate of the maximal effect by assuming a static rest frame for the CRs relative to the Sun's velocity which is about 225 km/s in the direction of Vega. This gives an expected anisotropy on the order of 10^{-3}.

1.2.4 Previous Observations

There have been many observations of the large scale cosmic-ray anisotropy in the TeV energy range. Many of these observations come from underground cosmic-ray muon experiments. In general these observations assume the CRs arrive from directly overhead the experiment and so do not have information in the declination direction. The data is analyzed by fitting harmonics to the distribution in the right ascension direction. A summary of the fundamental harmonic amplitude and phase information from a variety of experiments is given in Chapter 6. These observations show an anisotropy with a magnitude on the order of 10^{-3} with the maximum being roughly in the direction of the heliotail. This excess is sometimes referred to as the "tail-in" region. The anisotropy is also observed, by the KASCADE experiment [19], to decrease with increasing energy up to $\sim 10^{15}$ eV.

In addition there have been two-dimensional displays of the CR anisotropy published recently. The Tibet Air Shower Array, with a modal energy of 3 TeV [20], and Super-Kamiokande-I, with a median energy of 10 TeV [21], have identified two coincident regions of interest in their sidereal observations. They observe the excess or "tail-in" region, as well as a deficit at $\sim 200^{\circ}$ right ascension sometimes called the "loss-cone". This is a historical term coming from a theory that this deficit is caused by a conical magnetic field structure [22].

The Tibet array also looked at the time and energy dependence of the anisotropy. They found no time dependence by comparing data split into two five-year periods, 1997-2001 and 2001-2005. It is noted that if the anisotropy has a time dependence based on the solar cycle it might not be seen this way given the solar maximum

overlaps both of these sets. They also see the anisotropy remain constant up to about 12 TeV at which point it decreases in magnitude.

The Earth-motion Compton-Getting effect has been observed as well and corresponds well with theory. However, a Galactic Compton-Getting effect has not been seen.

Chapter 2

The Milagro Detector

The Milagro gamma-ray observatory is an extensive air shower (EAS) detector located in the Jemez Mountains outside of Los Alamos, NM at a latitude of 35.88°N and a longitude of 106.68°W. The altitude of the detector is 2630 m above sea level giving an atmospheric overburden of $750 g/cm^2$. The detection of EASs is achieved using a water Cherenkov technique. Using this technique makes it easier (and cheaper) to build a detector having a large area with the ability to collect a large number of incident EASs. The Milagro detector has a field of view of ~ 2 sr and detects ~ 1700 EAS events per second, the majority of which are due to hadronic initiated showers. In addition the detector has a live-time of $> 90\%$. These characteristics make Milagro an excellent instrument for the measurement of both localized sources and larger scale phenomena.

2.1 Physical Principles

2.1.1 Extensive Air Showers

The direct detection of gamma-ray and cosmic-ray (hadronic) particles is impossible for ground based detectors since the large atmospheric overburden is opaque to these particles. However, this overburden can be used as an integral part of a detection device for very high energy particles. When a primary cosmic-ray particle enters the atmosphere it initiates a secondary particle cascade called an extensive air shower (EAS). Properties of the EAS can then be used to determine the direction, energy, and type of incident particle. The development of EAS is a complicated process but has been thoroughly studied (e.g. in [23]). A simplified model is given here.

The initiation of an EAS is dependent upon the type of incident particle. In the simpler case of a gamma-ray primary, the interaction of the photon with a molecule in the atmosphere creates an electron-positron pair. This electron-positron pair then produces high energy photons through bremsstrahlung which interact with the atmosphere creating more electron-positron pairs etc. This secondary particle cascade grows geometrically until the mean energy of the particles fall below a critical energy (about 85 MeV). At this point ionization losses predominates and the rate of fermionic pair production decreases dramatically. After reaching this point (called the "shower maximum"), the number of secondary particles decrease on the way down to the ground.

Since the secondary particles are ultrarelativistic, the shower develops as a front, perpendicular to the incident particle's direction, with a thickness of about $1m$. It

is this perpendicular development of the EAS that allows for the detection of the primary particle's direction through the measurement of PMT timing information. The largest concentration of particles is in the center of the front and is termed the "shower core". This shower front is slightly curved given that particles at the edges tend have less energy and are therefore more susceptible to Coulomb scattering. This scattering also leads to the lateral extent of the shower being quite large ($\sim$ 100m).

For showers initiated by cosmic-rays, the evolution has some similar features as above. In this case however, there are more possible reactions including a hadronic cascade, caused by the scattering and spallation of primaries interacting with atmospheric nuclei and molecules, and the production of $\pi^{\pm}$ and π^{0} particles. The π^{0} particles can decay into photons which then proceed as in the above case. The $\pi^{\pm}$ decay process produces muons and neutrinos. A muon can then decay into an electron or positron, depending on the muon type, and a neutrino. Figure 2.1 shows a schematic view of a cosmic-ray initiated EAS. For both gamma-ray and cosmic-ray initiated showers, the dominant particles reaching ground level are electrons, positrons, and photons.

2.1.2 Cherenkov Radiation

A common method of detecting the high energy charged particles present in EASs is through the observation of Cherenkov radiation. When a charged particle with velocity $\vec{v}$ moves through a dielectric medium with a speed larger than the propagation speed of light in that medium, Cherenkov radiation is produced. This radiation is emitted as the atoms and molecules of the medium return to equilibrium after

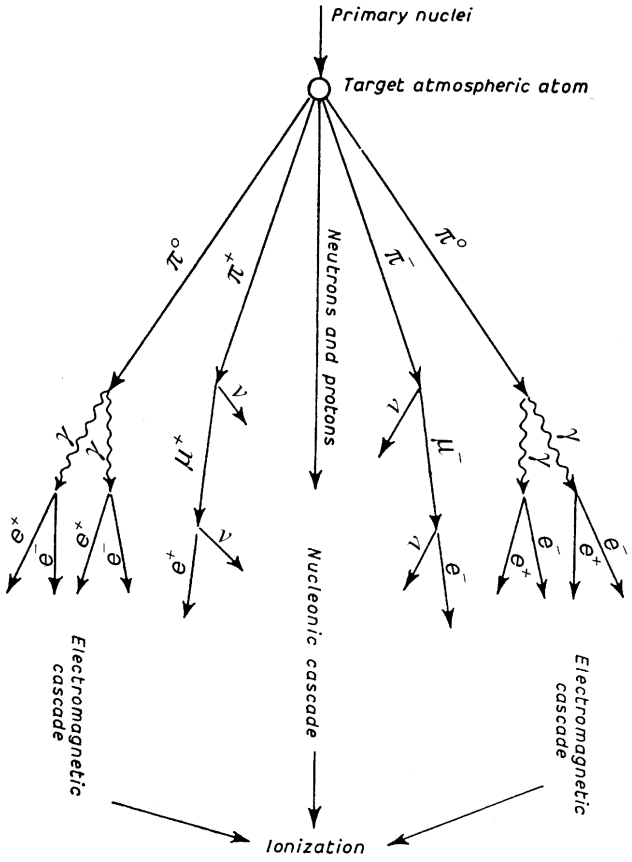

Figure 2.1: Schematic view of a cosmic-ray initiated extensive air shower. Figure taken from [3].

being polarized by the moving charged particle. The photons emitted will constructively interfere as long as the polarizing particle is moving faster than the speed of light in the medium. This emission propagates as a cone of light with an opening angle relative to the direction of $\vec{v}$ equal to:

$$\theta = cos^{-1}(\frac{c}{vn}) \tag{2.1}$$

where c = speed of light, v = speed of the charged particle, and n = index of

refraction of the medium. In water $n = 1.35$, giving an opening angle of about 42° for ultrarelativistic particles ($v \approx c$).

For this phenomena to occur at all, a moving particle with rest mass m, must satisfy the following relation:

$$E_{particle} > \frac{mc^2}{\sqrt{1 - \frac{1}{n^2}}} \tag{2.2}$$

Using this relation it is easy to show that in water the threshold energy for Cherenkov radiation production of an electron is 0.76 MeV, for a muon it is 0.16 GeV, and for a proton it is 1.4 GeV. This is, by extension, the threshold energy required for detection of these particles by the photomultiplier tubes in the Milagro detector.

2.2 Physical Layout of the Milagro Detector

2.2.1 Pond

Figure 2.2 is an overhead view of the Milagro detector showing the covered pond and the "outrigger tanks" in red. The pond is located in the center and has dimensions of $80m \times 60m$ at the surface. The depth is $8m$ and the sides slope to a dimension of $50m \times 30m$ at the bottom (see Figure 2.3 for a schematic diagram). The pond is protected by a light-tight cover allowing for operation regardless of weather conditions or time of day. This cover can be inflated for repairs. A lightning protection system was also constructed around the detector consisting of a network of wires suspended above the pond. The pond is filled with about 24 million liters of purified

Figure 2.2: Aerial view of the Milagro detector. The rectangular area in the center is the pond. The red disks show the location of the outrigger tanks.

water which is recirculated at a rate of $\sim 750 l/min$. The recirculated water flows through a filtration system to remove particulate matter and also through a UV filter to prevent biological growth. This system is implemented to maintain clarity of the water which is important for the accurate reconstruction of EASs. The quality of the pond water can be gauged by measuring the attenuation length of the water. The most recent measurement shows an attenuation length of $13m$ at a wavelength of $325nm$, the wavelength of Cherenkov radiation with peak detection sensitivity in Milagro.

The pond is instrumented with 723 photomultiplier tubes (PMTs) manufactured by Hamamatsu (model #R5912SEL) and arranged in two layers: the top, or "air-shower" (AS) layer, consisting of 450 PMTs at a depth of 1.5 meters; and the bot-

tom layer, or “muon” (MU) layer, consisting of 273 PMTs at a depth of 6 meters (see schematic in Figure 2.3). The AS layer is used for event triggering and reconstruction. The MU layer can be used for background rejection (when looking for gamma-ray sources). The PMTs in both layers are buoyant and arranged in a $2.8m \times 2.8m$ grid with the MU layer grid offset from the AS layer grid by half the grid distance. This grid distance was chosen as it is close to the distance of the Cherenkov cone size at the level of the PMTs. The depth of the AS is approximately five radiation lengths giving Milagro the ability to detect gamma-rays (which outnumber electrons-and positrons by about five to one in an EAS at ground level) that will have converted into electron-positron pairs by the time they reach the AS layer. Figure 2.4 shows the PMT grid under the cover. Each buoyant PMT is tethered in such a way so the photo-cathode faces upwards. Each PMT is also surrounded by a conical “baffle”. The baffle is in place to both block horizontal and upward traveling photons (mainly from large zenith angle muons), and increase the collection area of the PMTs. Originally these baffles were constructed from aluminum, but tended to corrode over time leading to reduced photon collection capability and the degradation of water quality. These were therefore replaced by polypropylene baffles. These replacements were done in two sessions in 9/2003 and 9/2005.

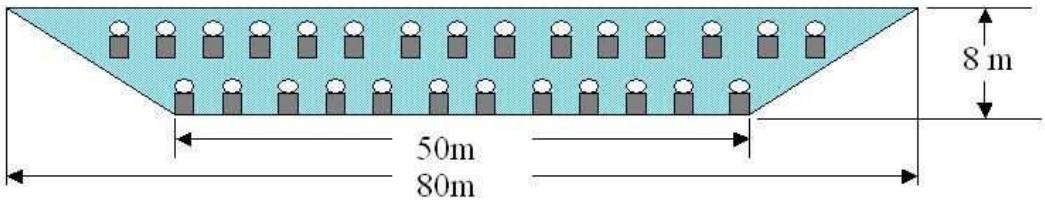

Figure 2.3: Schematic view of the Milagro pond.

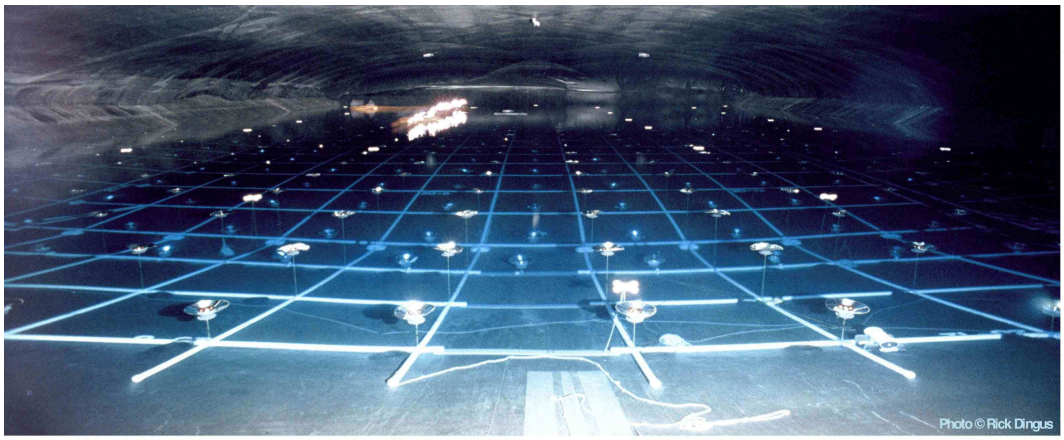

Figure 2.4: View of the pond showing the PMT grid from under the inflated cover.

2.2.2 Outrigger Array

The number of PMT hits in the pond cannot be used as a good measure of particle energy if nothing is known about the core location. A low energy air-shower with its core on the pond can have the same number of PMTs hit as a high energy shower hitting far away from it. In order to better determine the core location the an outrigger array was installed. The Milagro pond is surrounded by this outrigger array, consisting of 173 outrigger tanks, which expands the collection area of the detector to $40,000m^2$ (although with sparser sampling). This array was installed incrementally starting in 1999 and was completed in 2003. Each outrigger tank is cylindrical with a height of $1m$ and a diameter of $2.4m$. These tanks are filled with water and instrumented with a single, downward facing PMT. To increase the light collection capability of the PMT, the inside of the tank is lined with Tyvek (a white, reflective material). This large outrigger array allows for the more accurate determination of

EAS cores leading to an improvement in the angular reconstruction of an event. In addition, the outrigger array is used in the estimation of primary particle energy.

2.3 Electronics

The electronic system is responsible for taking the raw PMT data and converting it to useful information regarding individual primary particles. To do this there needs to be a mechanism for interpreting the large amount of data received from the PMTs as well as quickly selecting candidate signals to be analyzed. This section describes the main electronic subsystems of the Milagro detector used to accomplish this task.

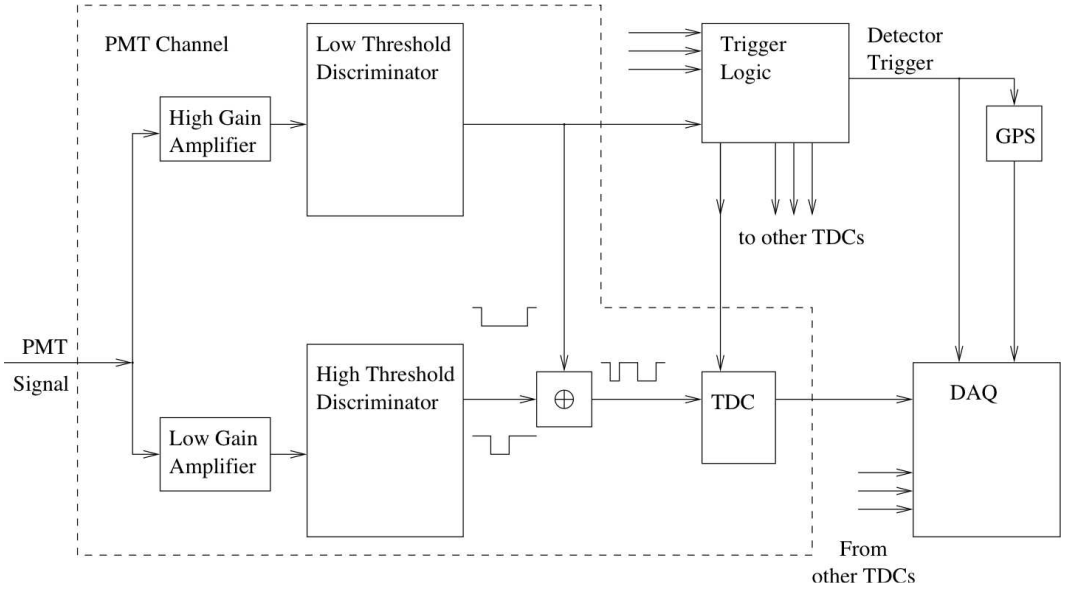

Figure 2.5: Schematic of the Milagro electronics system. Figure taken from [4]

2.3.1 PMT Pulse Processing

The PMTs are grouped into sets of 16, each with its own high voltage (HV) power supply and front end board (FEB) used to process the PMT signals. The signal received by the FEB from a given PMT consists of a pulse. The information one wishes to extract from a given pulse is the time it was detected and the intensity of the collected light. This information is collected using the time-over-threshold (ToT) method. The ToT method is used rather than analog-to-digital converters which would have seriously increased the expense.

The method works by taking the PMT pulse and sending it through both a low gain ($\sim 1\times$) and high gain ($\sim 7\times$) amplifier. The output of each of these signals runs to a discriminator. The output of the discriminator is digitized and is equal to zero until the pulse height crosses a threshold where the signal changes state creating an "edge". When the pulse falls back below the threshold (decaying in the manner of an RC circuit) the signal reverts to zero creating another edge. There are two thresholds used: one at about 0.25 photoelectrons (PEs) (using the output from the high gain amplifier) and the other about 5 PEs (using the output from the low gain amplifier). The output takes two forms (see Figure 2.6) depending on pulse height. Also from this figure it is easy to see that a larger pulse height results in a longer time between edges (this is where the term ToT comes from). Since the pulse height is proportional to the intensity of the incident light on the PMT, the ToT can be used as a measure of this intensity. The ToT is recorded using a LeCroy FASTBUS time-to-digital converter (TDC) and is sent along with the edge train to the triggering mechanism. The time of the event is taken to be the time at the first

low threshold crossing. Since each PMT can differ in their operating characteristics (PE to ToT relationship, time of pulse propagation through the cable), a pulsed laser system is periodically used to calibrate the output of the PMTs in the pond.

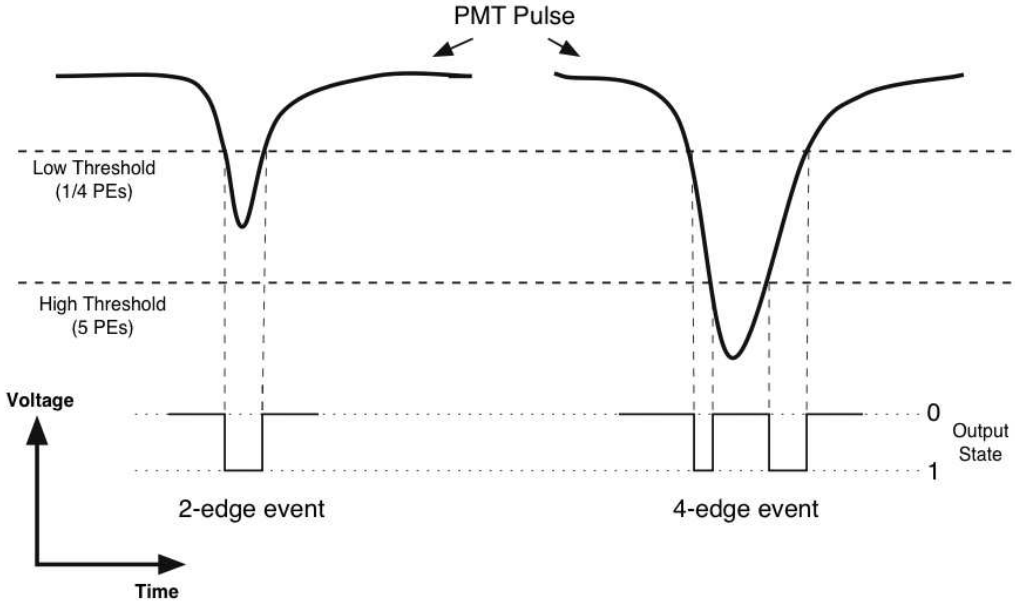

Figure 2.6: Visualization of the translation between a PMT pulse and time-over-threshold (ToT) for two pulse sizes.

2.3.2 Triggering

To accommodate the large number of events coming from different directions an event trigger was needed. Milagro has used two different triggering mechanisms over its lifetime. From about 1/1999 through 3/2002, Milagro utilized a simple multiplicity trigger. The multiplicity trigger counts the number of PMTs hit in the AS layer (N_{AS}) over some time window. This window was set to $\sim 300ns$ which is approximately the propagation time of a horizontally moving shower through the

pond. In order for a shower to trigger an event ,which results in data from the TDC modules being sent to the data acquisition system (DAQ), it must have hit at least 60 PMTs in the AS layer within the time window. This threshold was chosen in order to lower the energy threshold of the detector while restricting the number of single, large zenith-angle muons triggering the detector. This threshold also keeps the event rate below the maximum that the DAQ can handle ($\sim 2000Hz$).

The rejection of the single muon triggers can be done during the angular reconstruction. Since the Cherenkov light from an event triggered by an EAS will follow a planar path through the detector, this can be discriminated from an event triggered by a single muon for which the Cherenkov light will not be planar but rather conical. However, it is desirable to be able reject these muons with the trigger rather than the more computationally intensive angular fit. To this end a custom VME card was installed in 3/2002 which could differentiate between the different time profiles created by EASs and large zenith-angle muons.

The different time profiles are parameterized by a quantity called "risetime". The risetime is defined as the time elapsed during the collection of $10\% - 90\%$ of total hits for a given event. A uniform plane of Cherenkov light, such as that from an EAS, passing through the detector will have a lower risetime than that of a muon. Given this difference in risetimes, the VME card was programmed to include this in the event trigger and was initially set up with the following parameters:

- $N_{AS} > 20$ & risetime $< 50ns$
- $N_{AS} > 53$ & risetime $< 87.5ns$
- $N_{AS} > 74$

The VME card also operated with a smaller time window of $\sim 180ns$. Around 4/2006 the VME trigger card failed. Since that time a new triggering system which operates on the same principle but with an even smaller time window of $\sim 80ns$ has been in use. Over the entire Milagro lifespan the triggers have been adjusted to maintain a event rate that was around $1700Hz$.

2.3.3 Data Acquisition System

When the conditions for a triggered event are met, the raw TDC data along with a time stamp of the event, recorded from a GPS clock, are sent to a VME memory module. These data are then read out and processed by the DAQ system. This system consists of a series of "workers", which is responsible for reconstructing the raw event data, and the main DAQ computer, which serves the raw data to the workers and collects the reconstructed event data for storage. This reconstructed event data includes, but is not limited to, information such as: the arrival direction of the primary particle, the arrival time in MJD, the location of the shower core, and the number of PMTs hit in each of the three layers. This reconstructed data is stored in a RAID array on-site and is also saved at the University of Maryland. The amount of reconstructed event data comes to about 5 GB per day.

Monitoring of the DAQ system (and Milagro in general) is performed to ensure continuity of data collection (within reason) and data quality. Irregularities in the data taking are recorded daily as are individual problems when they arise in an online logbook by a member of the collaboration who is on shift.

2.4 Event Reconstruction

As described is Section 2.1.1, a primary particle produces an EAS which has a larger concentration of secondary particles along the shower axis, called the shower core, and a curved shower front surrounding it. The relative advancement of the shower front particles through the pond (i.e. the PMT hit times) is used to determine the original direction of the primary particle (see Figure 2.7). However there is an uncertainty inherent in this determination due to the core location, thickness of the shower front (about $1m$), and due to its curvature.

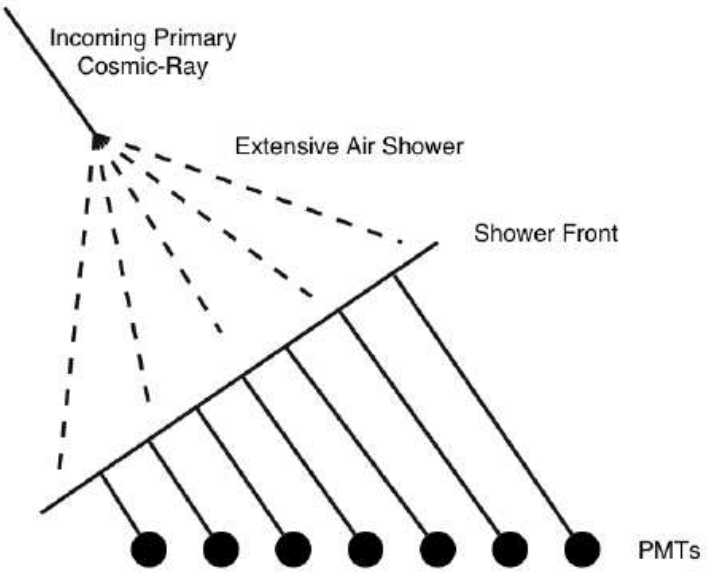

Figure 2.7: Visualization of the advancement of a shower front through the Milagro pond. The relative hit times of the PMTs can be used to reconstruct the direction of the primary particle initiating the air shower.

2.4.1 Timing Corrections

The shower thickness has the effect of skewing the relative timing of the AS PMT hits. The reason for this is that the time of a PMT hit is recorded when the first photoelectron (PE) is detected. Since detection of a PE is a probabilistic event, a volume of the shower front with higher density of particles will, on average, record an earlier detection time than that with lower density. This time difference can be corrected using the number of PEs measured in each individual PMT hit determined from a method developed using monte carlo simulation comparisons with data.

The shower curvature also skews the relative timing of the PMT hits. A direct fit of a curve to the shower front is far too slow to be effective given the high event rate and complexity of the fit function. For this reason the relative timing is corrected with a linear function (cylindrically symmetric around the shower axis) of fixed slope determined by monte carlo simulation. The value of this correction is determined to be about $0.7 ns/m$, where the distance is measured from the core location to the PMT for which this time correction will be added. Having these PMT timing corrections, the angular reconstruction can be performed. The first step required is determining the core location.

2.4.2 Core Location

The determination of the core location has been accomplished using a number of different methods since Milagro first started running. At the heart of all of the earlier methods was a simple “center of mass” calculation defined as follows:

$$x_{core} = \frac{\sum_{i=1}^{N} x_i \sqrt{PE_i}}{\sum_{i=1}^{N} \sqrt{PE_i}} \tag{2.3}$$

$$y_{core} = \frac{\sum_{i=1}^{N} y_i \sqrt{PE_i}}{\sum_{i=1}^{N} \sqrt{PE_i}} \tag{2.4}$$

where i runs over all PMTs hit for the event (1...N), x_i and y_i giving the coordinates of the ith PMT, and PE_i the number of PEs recorded in the ith PMT. The weighting of $\sqrt{PE_i}$ was chosen to keep PMTs with a large number of PEs hit from completely dominating the fit. Before the addition of the outrigger (OR) array, only the AS PMTs are used. This clearly has a disadvantage given it is more likely that the core would have landed outside of the pond given the small size and indifference of cosmic-ray showers to its location. Methods were developed to estimate whether or not the core landed on or off the pond. If the core was determined to be off the pond, the distance was set to be $50m$ from the center of the pond in the direction given by the center of mass. Otherwise, the above equation was used.

After the addition of the OR array, the ratio of the number of OR PMTs hit to the number of AS PMTs hit was a good estimator of whether or not the core was on the pond or not. If the core was on the pond, the above equation again would be used, if not, the above equation would be used with the OR PMTs used in the calculation instead of the AS PMTs.

The latest method of determining core location uses a 2-D Gaussian χ^2 minimization. The center of this Gaussian gives the location of the shower core. In this minimization, both the AS PMTs and the OR PMTs are used.

2.4.3 Angular Reconstruction

Using the core location the relative PMT hit times are corrected. The corrected PMT timing information is then fit to a plane using a weighted χ^2 fit. Each PMT is weighted according to the number of detected photons. The fit is iterated five times. In the first fit, PMTs with a small number of PEs are not included. In subsequent iterations, PMTs with poor residuals are discarded and the number of PEs required for a PMT to be included in the fit is reduced. After the fifth iteration, if the arrival direction is unphysical or the fit fails, the event is thrown out. For a successfully reconstructed event, the number of PMTs participating in the fit is also recorded (N_{fit}). This parameter turns out to be useful in event selection and will be used to improve the quality of cosmic-ray data. This will be discussed in a later section. The angular resolution of Milagro using this procedure is better than 1° with $\sim 90\%$ of triggered events being successfully fit.

2.5 Monte Carlo Simulation of the Detector

Lacking any controllable TeV sources located outside the Earth's atmosphere, the only way to estimate the response of the detector is through the use of monte carlo (MC) simulations. These MC simulations can be used to estimate various parameters useful to the operation of Milagro such as: EAS impact parameters, angular resolution, energy determination, and effective area.

The MC has two main components: simulation of an EAS in the atmosphere, and simulation of the shower front through the Milagro detector. The simulation of the air shower is accomplished using the CORSIKA (Cosmic Ray Simulations

for Kascade) package[24]. This part of the MC first simulates the interaction with the atmosphere of a primary particle with some energy, direction, and type. The secondary particles produced in this interaction are then propagated through an atmosphere of nitrogen, oxygen, and argon (78.1%, 21.0%, and 0.9% volume proportions respectively) down to the detector level. The energies of the simulated particles can extend to 10^{20}eV. The types of particles simulated are gamma-ray photons and nuclei as heavy as iron. These particles are thrown with a power-law spectrum of the form $dN/dE = E^{-2.0}$. The events can be re-weighted during later analysis to conform to the proper spectral indices for the particle type.

After the simulation of the shower is complete, the motion and types of secondary particles in the shower front are input to the GEANT4 (GEometry ANd Tracking) package[25]. The GEANT software takes this information and simulates the propagation of these particles through a virtual Milagro detector. The shower fronts are distributed over an area 1000 m around the detector. The output of the software mimics that of the actual detector with the addition of the true direction, energy, and particle type of the primary particle. This output can then be used to test detector response as well as various analysis methods.

2.5.1 Gamma-Hadron Separation

Since Milagro was designed specifically with the observation of gamma-rays in mind, the ability to separate gamma and hadronic initiated EASs is important. MC simulation is an indispensable tool in creating techniques capable of doing this. However, given the focus of this work is on the hadronic component of cosmic-rays, this separation will not be discussed here. For an in-depth study of these

techniques see [26].

2.5.2 Energy Estimation

There are a couple of energy estimation algorithms that have been used with Milagro. There is an event-by-event estimator which is based on gamma-ray simulations and is discussed in detail in [27]. For the analysis in this thesis the energy estimation is based on an the natural log of an energy dependent parameter(ln(fOut)). The parameter fOut is defined as the fraction of live outrigger PMTs hit for a given event. In practice the data is split into eight bins of width 0.5 in ln(fOut). The first bin has ln(fOut) < -3.5 and the last $-0.5 \leq$ ln(fOut) ≤ 0.0. Since all of the analyses in this thesis are based on data that use the same quality cuts, this discussion will include the same cuts which are: $N_{fit} \geq 50$ and zenith angle $\leq 50^{\circ}$. The reasons for these specific constraints will be discussed in the data analysis section. With these cuts, Figure 2.8 shows the event rate for the four years of Milagro data after the outrigger array was installed as a function of the eight ln(fOut) bins as well as the correlation between ln(fOut) and energy determined by MC. The MC uses the fluxes and spectral indices for Hydrogen to Iron as determined by the ATIC experiment [28]. The median energy of triggers is found using the MC simulation to be 6 TeV. As can be seen the energy resolution is quite poor at low ln(fOut) and improves slightly at higher ln(fOut).

2.5.3 Effective Area

The detection area of Milagro is not explicitly defined by its physical size due to the size of the showers and the fact that the shower core need not land within the detector boundaries in order to trigger an event. For this reason the concept of effective area is defined which gives a measure of the efficiency of particle detection as a function of energy and zenith angle. The effective are is defined as:

$$\frac{dN}{dt} = \int\int\int d\Omega dA dE A_{eff}(E,\theta)\Phi(E,\theta) \tag{2.5}$$

where $\Phi(E,\theta)$ is the differential primary flux as a function of energy and zenith angle.

This effective area is calculated from MC simulation in an energy range E to $E+\delta E$, and a zenith angle range θ to $\theta+\delta\theta$ using:

$$A_{eff}(E,\theta) = A_{throw}\frac{N_{trig}(E,\theta)}{N_{thrown}(E,\theta)} \tag{2.6}$$

where A_{throw} is the area over which the simulated particles were thrown , N_{thrown} is the total number of simulated particles, and N_{trig} is the total number of simulated particles which actually trigger an event in the detector.

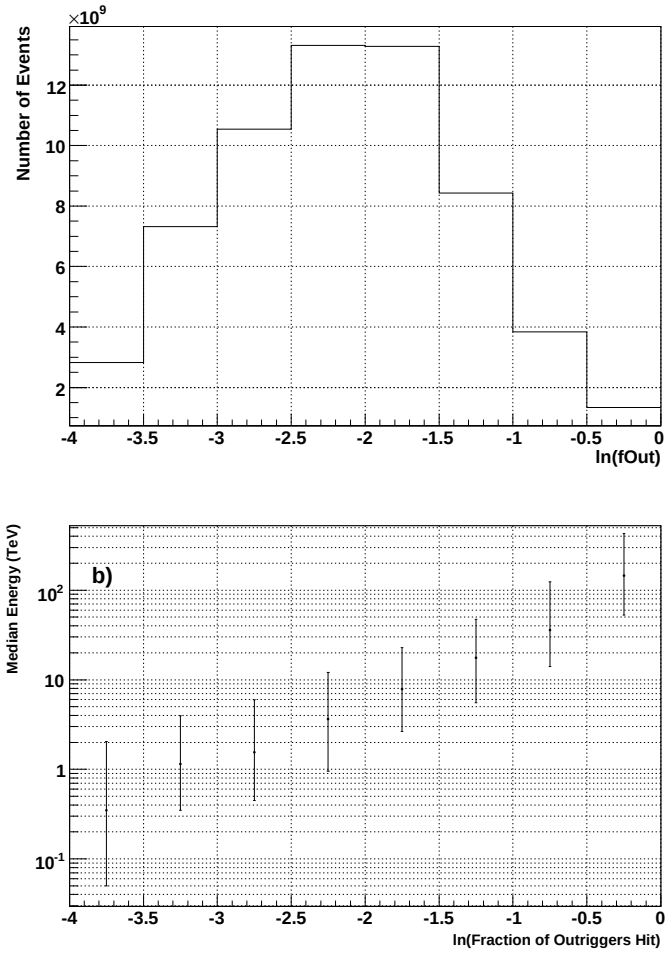

Figure 2.8: Top: Number of events vs. the eight ln(fOut) bins for actual Milagro data taken from 2004-2007. Bottom: The monte carlo simulated correlation between the eight ln(fOut) bins and median energy. The asymmetric error bars are calculated using the inner 68% of simulated data.

Chapter 3

Data Analysis

3.1 Celestial Coordinate Systems

The distance to astronomical objects outside the solar system is sufficiently large with respect to the Earth's size and orbit that they appear to lie on the surface of an imaginary sphere termed the "Celestial Sphere". There are a number of different coordinate systems that astronomers have defined to describe the location of objects on this sphere. The equatorial coordinate system is the most relevant to future discussion in this work and will be discussed now.

3.1.1 Equatorial Coordinate System

The equatorial coordinate system, a star-fixed or "sidereal" coordinate system, can be thought of as the projection of the Earth's coordinate system (latitude and longitude) onto the Celestial Sphere at a specific instant in time (See Figure 3.1). The projection of the equator defines the Celestial Equator (CE) and the projection of

the poles defines the North and South Celestial Poles (NCP and SCP).

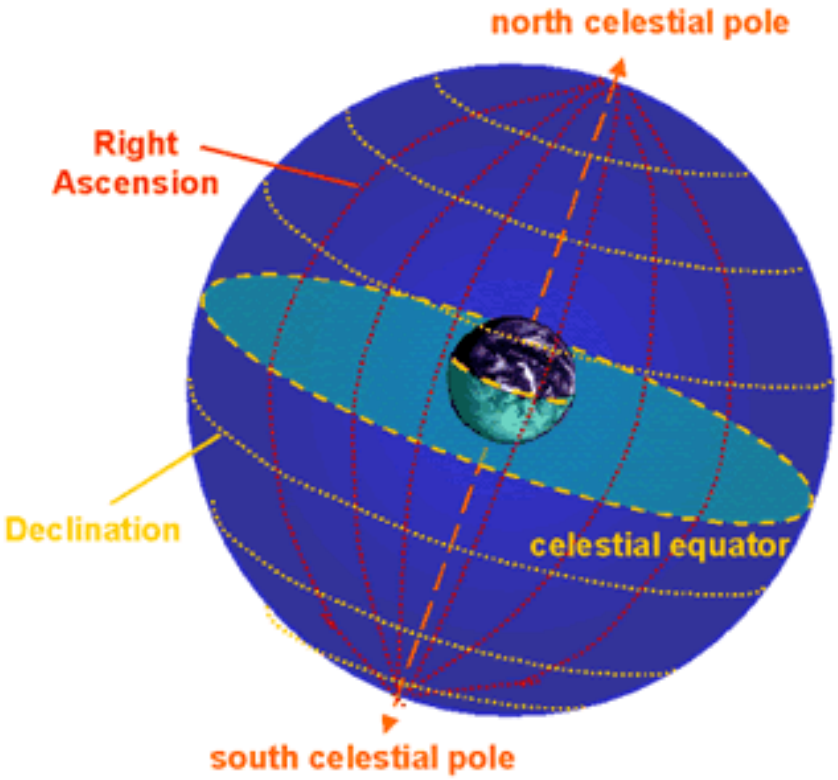

Figure 3.1: Diagram of the equatorial coordinate system. Figure taken from [5].

The two coordinates of the equatorial system are: right ascension (r.a.), and declination (dec.). The dec. of a point on the Celestial Sphere is simply the analog of latitude on Earth. The dec. of the NCP is $90°$, the dec. of the SCP is $-90°$ and the dec. of the CE is $0°$. Right ascension is the analog of Earth's longitude with zero right ascension fixed by the apparent position of the Sun on the Celestial Sphere at the vernal equinox. The vernal equinox occurs around March 21st and is the point when the Sun crosses the CE moving south to north. Right ascension increases from west to east, following the unfolding of the sky from an astronomer's point of

view on Earth as time passes. For this reason r.a. is often given in units of hours, minutes, and seconds. It is also acceptable to use units of degrees (with 24 hours being equivalent to 360°) which will be the convention used here.

Since the stars fixed on the Celestial Sphere appears to move from the perspective of an observer on Earth as the Earth rotates, it is also convenient to define another equatorial coordinate system which follows the rotation of the Earth called local hour angle (HA). This system uses the same definition of declination as the previous one. The longitudinal coordinate is now called hour angle. As the Earth rotates, a star, fixed at some r.a. and dec., will follow its fixed declination but change in hour angle. To define HA it is necessary to introduce the concept of local sidereal time (LST). Sidereal time (ST) is equivalent to r.a. and can be used interchangeably, local sidereal time on the other hand is defined as being the right ascension of the celestial meridian for an observer at a given point in time. The celestial meridian being the semi-circle of right ascension running from the NCP to the SCP containing the point at which the line extending from an observer's location on the surface of the Earth in the direction opposite to the force of gravity, intersects with the Celestial Sphere (this point is also called the "zenith"). The relationship between HA and ST (or r.a.) and LST is then defined as: HA = LST - ST. The HA-DEC coordinate system, thus defined, rotates with the Earth and is a fixed coordinate system for an observer or observatory (e.g. Milagro) at a fixed location on Earth.

3.1.2 J2000 Reference

The equatorial coordinate system, being based on the projection of the Earth's coordinate system, is not fixed in time. The apparent position of an object in the sky

from Earth changes over time due to changes in the Earth's orientation relative to the Celestial Sphere. These changes are caused by processes such as: precession, nutation etc. These are admittedly slow changing effects but need to be corrected for. The way this problem is solved is by fixing the equatorial coordinates with respect to the Earth's orientation at a specified moment in time which is called an epoch. Every epoch is 50 years long. The current epoch is called J2000 and is defined by the position of the Earth at noon on January 1st, 2000. In this work, all coordinates will be given with respect to this J2000 reference.

3.1.3 Modified Julian Date

To standardize the notion of date, independent of any specific calendar, the Julian Date (JD) convention was introduced. The JD is defined as the number of days since noon (Greenwich mean) January 1st, 4713 BC. Given more than 2 million days have passed since this time, another definition is used called Modified Julian Date (MJD) which is calculated as: MJD = JD - 2400000.5. Since this number also tends to have leading digits which do not change for decades, it is common to truncate the MJD. For example, midnight September 9th 2008 has a MJD of 54718.0. This is the convention that will be used henceforth.

3.2 Overview of Forward-Backward Asymmetry Method

The size of the effect we are looking for is around 1 part in a thousand. The varying detector conditions alone lead to rate variations around 100 times larger than this expected signal. For this reason the forward-backward asymmetry method, also used in particle physics (e.g. a search for CP violation using collider data in [29]) but easily adapted for use in this context, is used to remove problems arising from the short term variations in trigger rates due to effects which cannot be accurately modeled (weather, detector etc.).

Since Milagro scans the sky with the rotation of the Earth, the analysis method was designed to search for a coherent modulation of the cosmic-ray rate in the direction of this rotation. Figure 3.2 and Equation 3.1 define the forward-backward asymmetry (FB).

The quantity $R_{\Theta,\delta}(\xi)$ is defined as the number of cosmic-ray events collected during a particular time interval (Θ) in an angular bin at a given declination (δ) and local hour angle (ξ). The asymmetry is measured by subtracting two bins which are symmetric, in ξ, with respect to the local meridian. For a pair of bins centered at ξ, $-\xi$, and δ, the asymmetry is:

$$FB_{\delta}(\Theta,\xi) = \frac{R_{\Theta,\delta}(+\xi) - R_{\Theta,\delta}(-\xi)}{R_{\Theta,\delta}(+\xi) + R_{\Theta,\delta}(-\xi)} \tag{3.1}$$

The time intervals are parameterized by an angle Θ which specifies the relative advance of the local meridian through the sky for three different time frames:

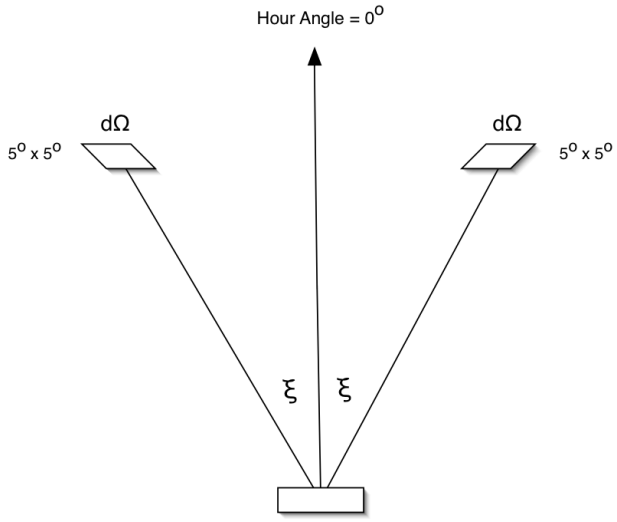

Figure 3.2: Diagram showing the definition of ξ used in the calculation of the forward-backward asymmetry for a single declination band and a given 30 minute histogr am. ξ is in the direction of hour angle.

$$\Theta = 3.75^\circ + 7.5^\circ \times IST$$

$$\Theta = 3.75^\circ + 7.5^\circ \times IUT$$

$$\Theta = 3.75^\circ + 7.5^\circ \times IAST$$

IST, IUT, and IAST are integers, from zero to 47, denoting half hour intervals of sidereal time, UT, and anti-sidereal time (defined below). In the above equations, the constants convert an integration time interval (1/2 hour) into degrees (7.5°) with the angle given at the center of each interval.

FB, being independent of overall detector rate, allows for the removal of trigger

rate variations, which can be as large as 20%, arising from changing atmospheric conditions as well as detector thresholds. In addition, since the method was designed to look at the rotational modulation of FB, any inherent asymmetry in the detector response will be removed; it is in fact independent of the observed asymmetry of the detector response which is at the level of 10%. Finally, by averaging many full days, each tracing out a full 2π in Θ, the daily atmospheric and detector variations, which are assumed to be completely random, are averaged out while a coherent signal is preserved. This entire approach allows a search for coherent signals in the data set down to the level of $10^{-4} - 10^{-3}$.

Given that this method measures the modulation in the direction of Earth's rotation, the modulation in the declination (dec) direction can not be observed. For this reason the anisotropy results determined using the FB method will show projections of the anisotropy in the direction of right ascension (r.a.) rather than the full 2-D anisotropy of the sky. Projections can be created for any dec. band visible to the detector. Since each dec. band traces a completely independent circle of the sky and contains statistically independent data, each dec. band is treated as a separate observation and is analyzed separately from the others. Any model of the true 2-D anisotropy can be confronted with, or constrained by, our data (given in Table 4.1) by projecting the model along r.a. in our dec. bands. The next sections show how this method is implemented using Milagro data.

3.3 Data Selection

There are a number of cuts on the data that are performed in order to limit systematic effects and improve the quality of the data sets. Only events with a zenith angle $\theta \leq 50^{\circ}$ are accepted. This zenith angle cut is used to limit contamination from large zenith angle muons. In addition to the zenith angle cut, accepted events are required to have used at least 50 PMTs in the angular fit. This particular cut was settled upon as it gives better agreement with Monte Carlo simulation of trigger rates and reduces the systematic effects dramatically due to the rejection of the lowest energy events.

Before the data are analyzed we also look for trouble spots which will be excluded from the analysis. Beyond the obvious times where there were repairs we look for large deviations in the zenith and azimuthal (ϕ) angle distributions. The way this is accomplished is by reading through the data and creating histograms of the θ and ϕ distributions, forcing each histogram to contain an equal number of events. The number of events is fixed to avoid picking out periods of dead time and is determined by calculating the number of events in a $\sim$ 30 minute interval given our average trigger rate of $\sim$ 1700Hz. These intervals are collected over a period consisting of about three days. The individual phi and theta distributions are then compared to the three day average by computing the chi square difference between them after normalization. If the chi square is larger than 23 for the θ dist. or larger than 5 for the ϕ dist. the failing histogram is sent to a file along with the time interval it corresponds to. These cutoffs were chosen because they give a reasonably low number of false failures without missing the problem spots. This procedure is

repeated for the entire data set. The output intervals can then be inspected by hand and compared to entries in the daily Milagro shift log. Many times these intervals will have associated log entries involving hardware failures, extreme weather etc. If the interval appears to be legitimately corrupted, determined from the log book or by visual inspection of the distributions, it is excluded. Cuts made in this fashion correspond to $\sim 5\%$ of the total number of events collected.

3.4 Organization of Event Data

The cosmic-ray events are binned in 2-D histograms according to their arrival direction (in local coordinates) from -10° to 80° in declination and -50° to $+50^\circ$ in hour angle (see Fig. 3.3 for an example). The events are collected over 30 "minute" periods, where "minute" is defined in the following three time frames: sidereal (366.25 days/year), universal (365.25 days/year), anti-sidereal (364.25 days/year). The events are placed into histograms with $5^\circ \times 5^\circ$ bins giving us 48 half hour histograms per day (in one of the three time frames). Each of the 48 histograms are binned the same for each day and can be summed over any number of days. This averaging scheme is used with the forward-backward asymmetry method described earlier in order to remove random anisotropies induced by changing atmospheric and detector conditions.

The time frames mentioned above correspond to different views of the sky. Universal time (UT) shows the sky in sun fixed coordinates (i.e. at Milagro longitude noon is at 195°). Sidereal time (ST) is the usual equatorial coordinate system of r.a. and dec. Anti-sidereal time (AST) corresponds to no physical viewpoint. As such

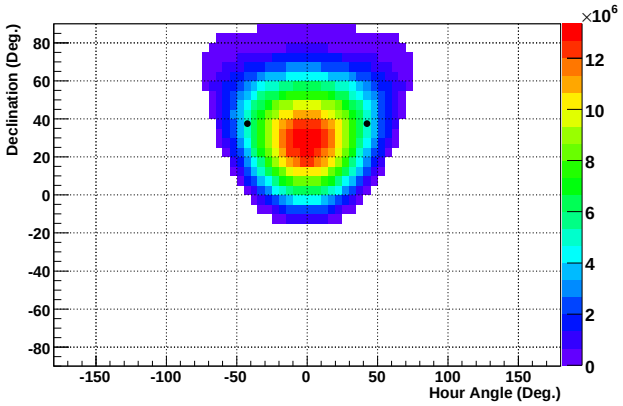

Figure 3.3: Sample of a histogram showing the number of events as a function of dec. vs. hour angle for a single 30 minute period. The black disks show an example pair of pixels shown in Fig. 3.2 for $\xi = \pm 42.5^{\circ}$ used in the calculation of the FB defined by Eq. 3.1

it should have no signal present but is included for symmetry and as a check on systematics (more on this later). A ST day is 3 minutes and 56.56 seconds longer than a UT day. An AST day is shorter than a UT day by the same amount.

In order to minimize contamination of the signal between the three time frames the data should be analyzed in sets of an integral number of years. For example, a fixed signal in sidereal time, this signal's position in UT shifts by about 4 minutes per day returning to the original position after exactly one year. When the analysis is done the mean value is subtracted out and therefore this fixed ST signal will average to zero in the UT map. The same holds true for AST except in AST a fixed sidereal signal will transit twice in one year.

3.5 Harmonic Fit

While the method used is FB, the desired result is the anisotropy in the cosmic-ray rates. The anisotropy ($A_\delta(\Theta)$) is defined as the fractional difference from the mean cosmic-ray rate. The assumption is made that the large-scale anisotropy in any given dec. band can be modeled by a Fourier series and that it is a small modulation of a nearly isotropic signal. Three harmonics are used in this analysis which allows us to see large-scale effects having a width in r. a. of greater than $\sim 40^\circ$.

For this model, the equation for the (normalized) rate becomes:

$$R_{\Theta,\delta}(\pm\xi) = 1 + A_\delta(\Theta) = 1 + \sum_{n=1}^{3} \gamma_{\delta,n} \cos n(\Theta \pm \xi - \Phi_{\delta,n}) \tag{3.2}$$

Using this model for the cosmic-ray rates, the expected FB is calculated and used in the fit to data in order to obtain the anisotropy parameters in 3.2.

The first step in finding the fourier coefficients ($\gamma_{\delta,n}$ and $\Phi_{\delta,n}$) is calculating the FB asymmetry (Eq. 3.1) for each half hour histogram (parameterized by Θ) as a function of ξ. The values of ξ used range from 2.5° to 47.5° in 5° steps. The observed values of FB are binned in a 2-D histogram of ξ vs. Θ which then has the mean value of the FB for each slice in Θ subtracted out to remove any constant bias in the detector response (See Fig. 3.4 for an example).

The fourier coefficients are obtained from these histograms by fitting to the following function, predicted by the model, obtained by substituting (3.2) in (3.1), applying the appropriate trigonometric identities and using the fact that $\gamma_n \ll 1$.

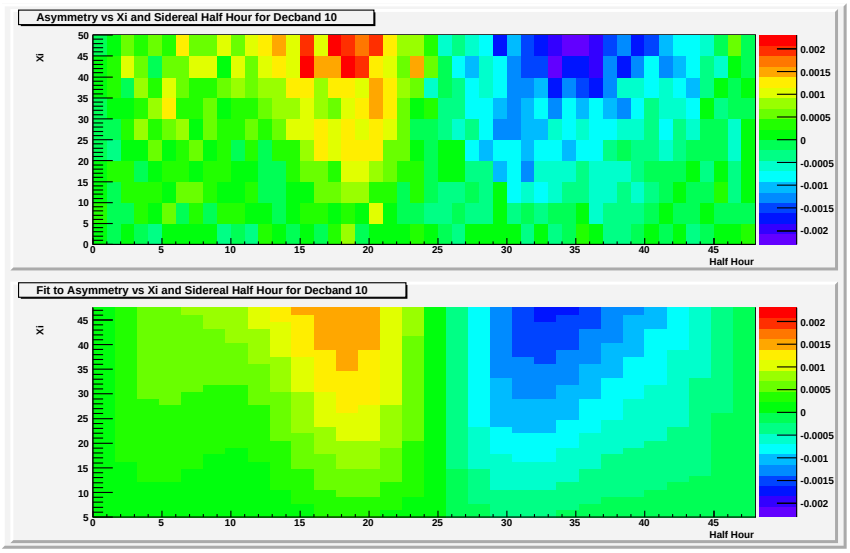

Figure 3.4: Sample histograms showing the forward-backward asymmetry as a function of ξ and hour angle for a single dec. band. The top plot shows the data and the bottom shows the result of the fit. A modulation of the FB as a function of Θ is clearly seen.

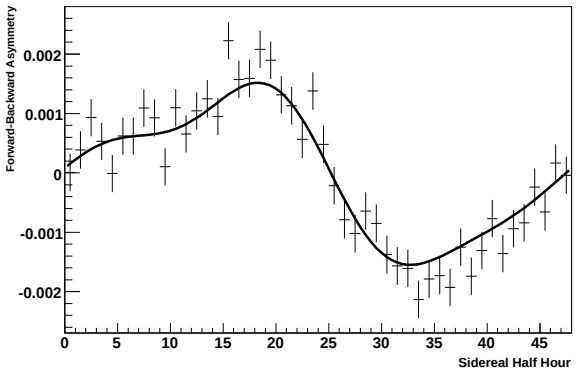

Figure 3.5: Sample histogram showing the result of the 2-D fit to the forward-back ward asymmetry (shown in the previous Figure) for a single slice in $\xi = 40^\circ - 45^\circ$ and a single slice in declination $\delta = 35^\circ - 40^\circ$.

$$FB_\delta(\theta,\xi) \approx \sum_{n=1}^{3} -\gamma_{\delta,n}\sin(n\xi)\sin(n(\theta-\phi_{\delta,n})) \tag{3.3}$$

A measurement can be made for any fixed ξ. The values of ξ described above were chosen to make each measurement statistically independent. Given this independence and the fact that each ξ is sampling the same sky, the above equation may then be used to fit all ξ as well as r.a. at the same time in a 2-D fit.

The result of the full 2-D FB fit and a sample for a single slice in ξ is shown here for actual data (Figs. 3.4 & 3.5). The output of the fit is the set of coefficients corresponding to the amplitude and phase of the three Fourier harmonics describing the anisotropy.

It is noted that this method averages over different ξ_i and that this translates into an averaging over any difference of energy in the data due to the dependence of atmospheric depth on ξ. An examination of this dependence is discussed in a later

section (5.0.2) and shows that this averaging is well justified.

3.6 Reconstruction

The six Fourier coefficients thus obtained in the fit are used to reconstruct the anisotropy projection as a fractional difference from isotropic in a given dec. band as follows:

$$A_\delta(\theta) = \sum_{n=1}^{3} \gamma_{\delta,n} \cos(n(\theta - \phi_{\delta,n})) \tag{3.4}$$

This reconstruction is performed for all 18 dec. bands independently which can then be combined to give a 2-D display of the anisotropy projection in the sky.

3.7 Number of Harmonics

The optimal number of fourier harmonics was determined by examining the chi square per degree of freedom for the 2-D fits as a function of declination. These results are plotted in Fig. 3.6. As can be seen the three harmonic fit gives a chi square/ndf of ~ 1 with no significant improvement for four harmonics and therefore was deemed sufficient.

3.8 Statistical and Systematic Errors

The statistical errors are obtained by the usual propagation method. Assuming the error during event collection obeys a poisson distribution, for a bin with a large

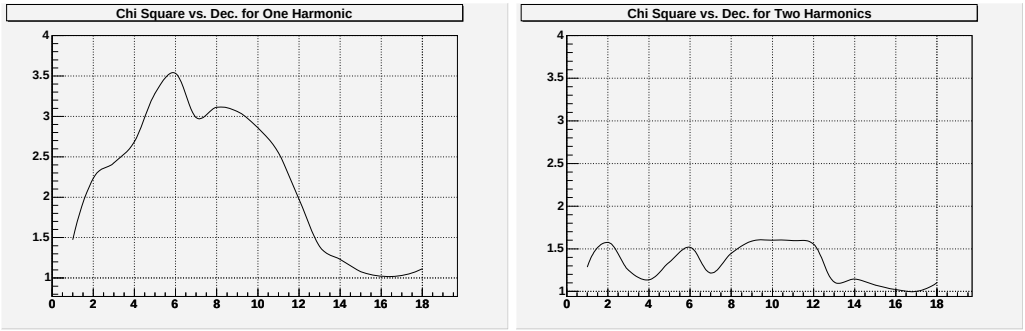

(a) One Harmonic (b) Two Harmonics

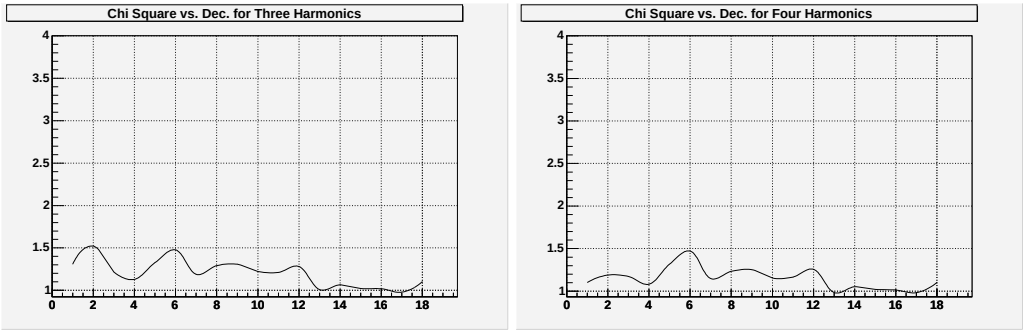

(c) Three Harmonics (d) Four Harmonics

Figure 3.6: χ^2/ndf vs. dec. for different number of fit harmonics.

number of N events the error is $\sqrt{N}$. From the fit we obtain the errors on the fit parameters from which the error in the reconstructed signal is calculated using:

$$\sigma^2_{signal}(\theta) = \sum_{n=1}^{3} \left[\sigma^2_{\gamma_n} \left(\frac{\partial A(\theta)}{\partial \gamma_n} \right)^2 + \sigma^2_{\phi_n} \left(\frac{\partial A(\theta)}{\partial \phi_n} \right)^2 \right] \tag{3.5}$$

The systematic errors are estimated by examining the AST time plots for an integral number of years. For an integral number of years a static signal in one time frame will not affect the others. The reason for this is explained in Section 3.4. Monte Carlo simulations show that if there is a time varying signal in one frame it will induce a signal in the adjacent frames since it doesn't average out over

the course of the year. The induced signal is attenuated greatly for slowly varying signals. Furthermore, MCs show that if the signal varies in universal time it will affect both anti-sidereal and sidereal time with equal magnitude but not necessarily the same phase. Given that anti-sidereal time corresponds to no physical frame of reference we expect to see no signal here. If a signal does appear here the cause is assumed to be due to random, residual variations, left over after averaging over many days, in the universal time signal. We can rule out the sidereal time variation as the origin of the AST signal because the sidereal signal, although not constant, only varies on the order of a factor of two over the entire seven year data set and therefore cannot induce the AST variations at the level we do see. Since we know this same AST signal will be superimposed on the sidereal signal but with unknown phase, we use the r.m.s. of these fluctuations to estimate the systematic errors of the sidereal anisotropy. The Monte Carlos mentioned above and a more detailed investigation of systematic errors is given in Section 5.0.6.

Chapter 4

Results

4.1 Sidereal Map

The results of the analysis for seven years worth of data is shown in Figure 1. This figure is constructed by placing the anisotropy projections for 18 declination bands, each band having a width of 5°, in their respective positions. Figures 4.2 & 4.3 show the individual declination projection profiles with the width of the curves corresponding to the statistical error. Table 4.1 contains the amplitude and phase fit parameters for each of the 18 declination bands. The $\chi^2/d.o.f.$ and the number of events is also given in this table.

Figures 4.4 & 4.5 show six years worth of data split (2000 - 2007) into two three-year periods. The main features are still present but there appears to be an increase in the magnitude of the anisotropy in the second three years.

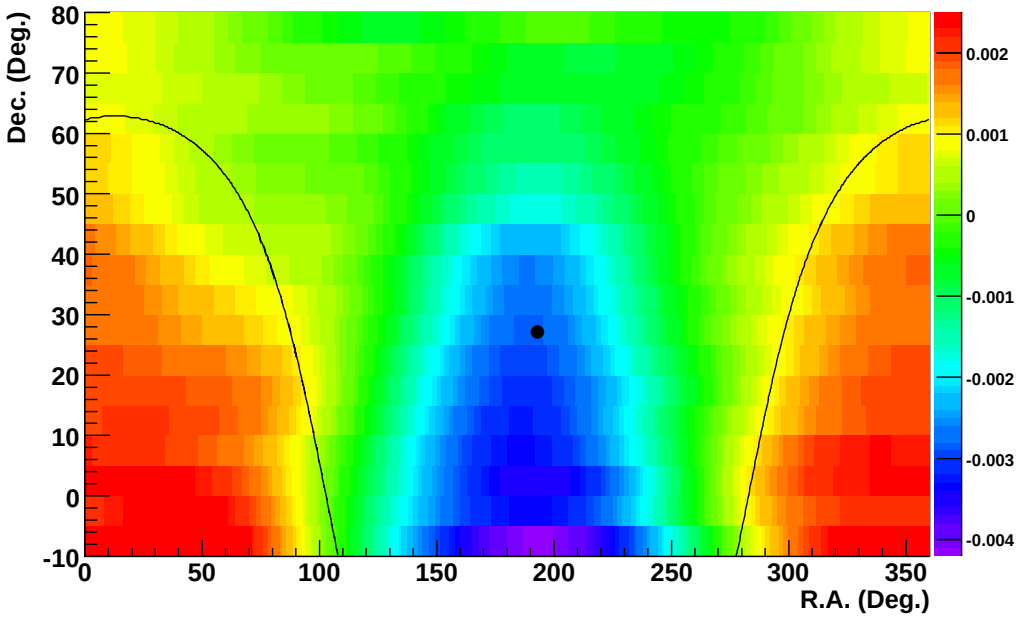

Figure 4.1: Measured Anisotropy: fractional deviation from isotropic cosmic ray flux in r.a. vs. dec. for data collected from 7/2001 through 7/2007. The solid line shows the Galactic Equator and the disk shows the location of the North Galactic Pole. The width of the color gradations is the size of the average statistical error ($\sim 1 \times 10^{-5}$).

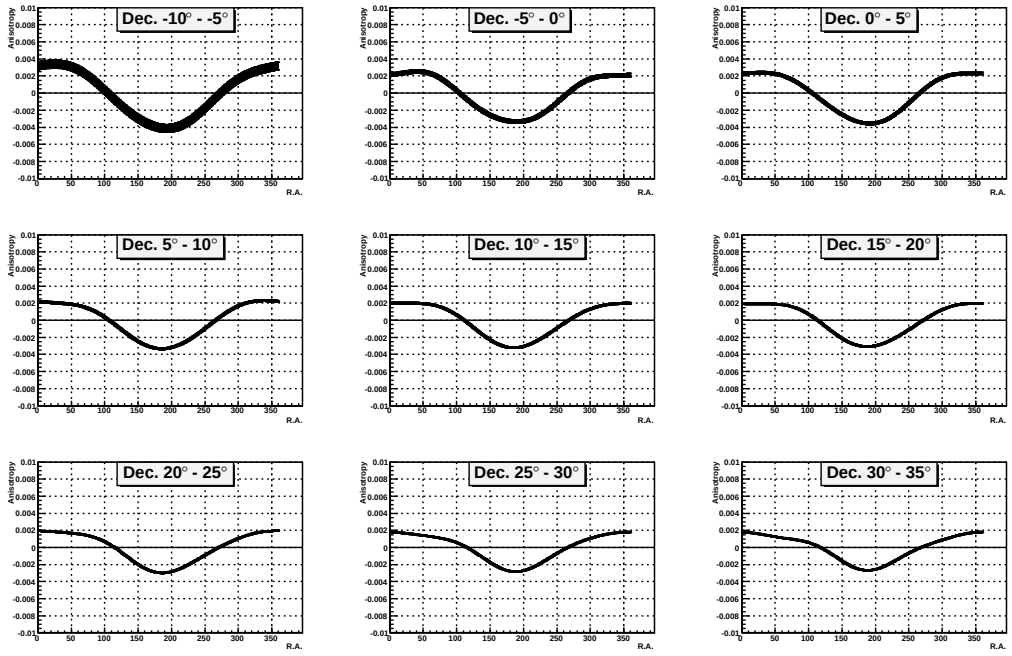

Figure 4.2: Anisotropy vs. r.a. for individual dec. bands from -10° to 35°. The dec. bands are arranged in increasing order from upper left to lower right. Each band represents 5° of dec. The line width corresponds to the statistical error.

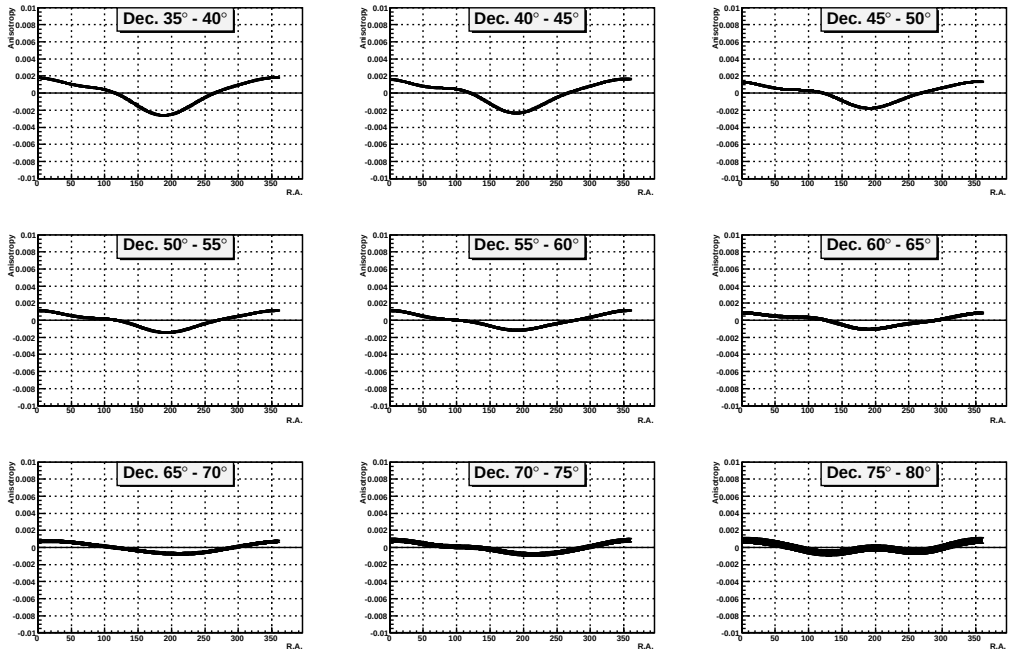

Figure 4.3: Anisotropy vs. r.a. for individual dec. bands from $35^\circ - 80^\circ$. The dec. bands are arranged in increasing order from upper left to lower right. Each band represents 5° of dec. The line width corresponds to the statistical error.

Dec. (mean)	1st Harm. Amplitude ($\times 10^{-3}$)	1st Harm. Phase (deg)	2nd Harm. Amplitude ($\times 10^{-3}$)	2nd Harm. Phase (deg)	3rd Harm. Amplitude ($\times 10^{-3}$)	3rd Harm. Phase (deg)	χ^2/d.o.f.	Number of events ($\times 10^9$)
77.5	0.54±0.26	2±27	0.37±0.14	13±11	0.10±0.11	-39±19	262.57/234	0.65
72.5	0.73±0.14	22±11	0.19±0.08	-25±12	0.06±0.06	11±19	266.50/282	1.38
67.5	0.72±0.09	23±7	0.06±0.05	-24±26	-0.01±0.04	208±116	308.67/330	2.39
62.5	0.83±0.07	19±5	0.12±0.04	-65±10	0.15±0.04	-2±4	355.61/330	3.63
57.5	0.99±0.06	6±3	-0.12±0.03	-312±8	0.15±0.03	3±4	379.61/378	4.98
52.5	1.10±0.05	8±3	0.22±0.03	-60±4	0.17±0.03	6±3	406.42/378	6.31
47.5	1.31±0.04	8±2	0.33±0.03	-63±2	0.21±0.02	2±2	498.02/426	7.51
42.5	1.71±0.04	8±1	0.44±0.02	-68±2	0.26±0.02	1±2	475.85/426	8.46
37.5	1.95±0.04	6±1	0.45±0.02	-73±1	0.24±0.02	3±2	472.71/426	9.07
32.5	2.04±0.04	10±1	0.47±0.02	-76±1	0.20±0.02	1±2	520.47/426	9.28
27.5	2.17±0.04	9±1	0.53±0.02	-78±1	0.14±0.02	0±3	551.53/426	9.07
22.5	2.39±0.04	11±1	0.52±0.02	-81±1	0.12±0.02	-12±3	564.14/426	8.44
17.5	2.56±0.05	12±1	0.57±0.03	-81±1	0.10±0.02	-32±5	523.45/378	7.45
12.5	2.62±0.06	9±1	0.61±0.03	-85±2	-0.05±0.03	-208±9	397.37/330	6.17
7.5	2.81±0.07	5±1	0.58±0.04	-80±2	0.08±0.03	-39±7	355.24/282	4.74
2.5	3.05±0.10	7±2	0.61±0.05	-80±3	0.14±0.04	54±5	280.00/234	3.31

Table 4.1: The six fit parameters, χ^2/d.o.f. and number of events for each dec. band. The quoted errors are statistical and are included in the calculation of χ^2.

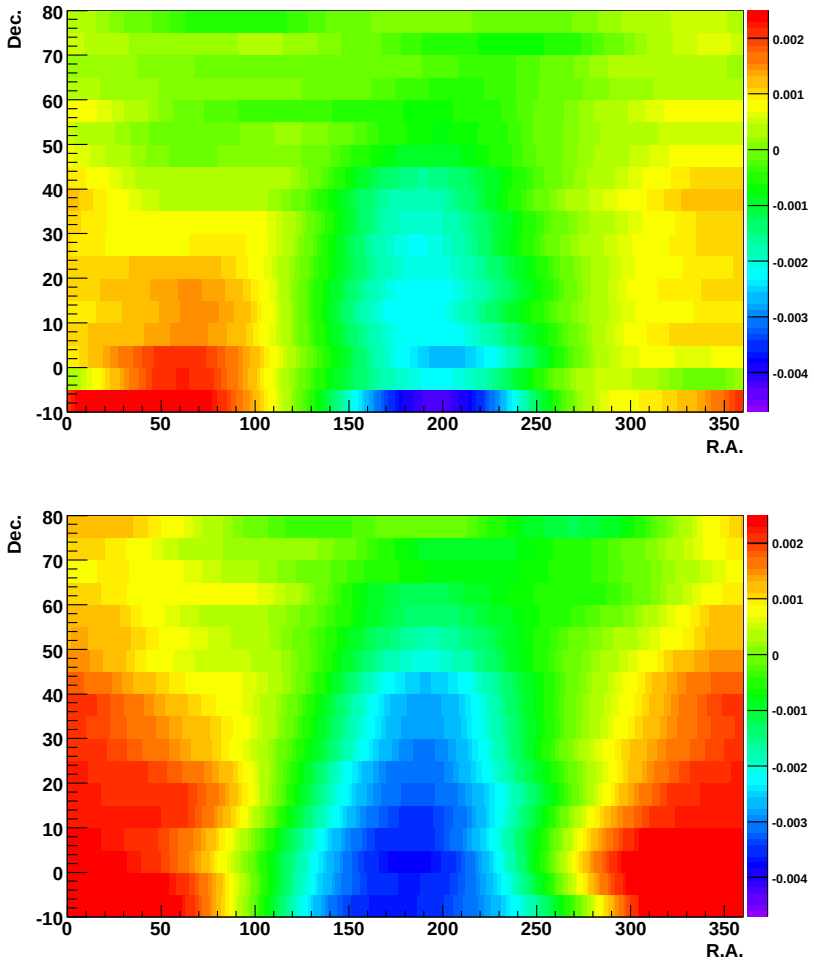

Figure 4.4: Anisotropy in r.a. vs. dec. for the first and second three year periods (2000-2003 and 2003-2006 respectively).

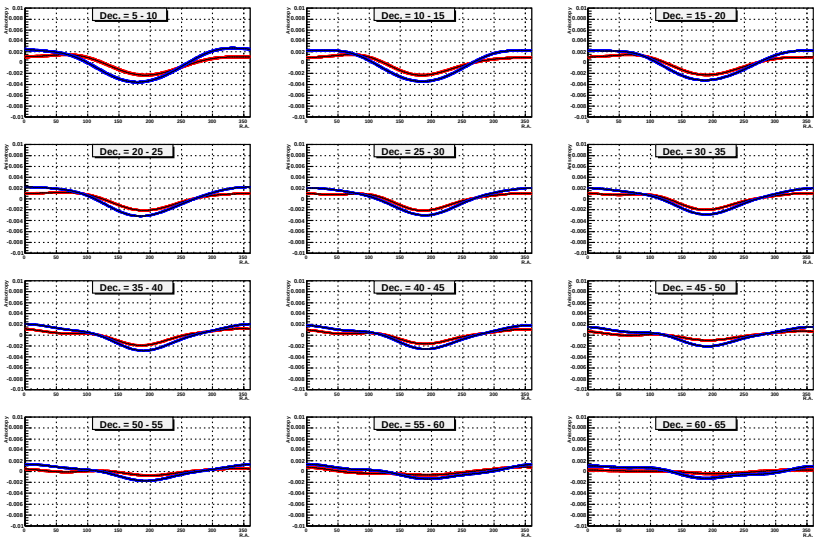

Figure 4.5: Anisotropy vs. r.a. profiles for the first and second three year periods. The profiles are given in 5° dec. bands increasing from top left to bottom right. The first and last three bands are not included for brevity. The red curve denotes the first three years and the blue the second.

In order to investigate this time dependence further, the data were split into sets corresponding to two month and one year averages. Using these data sets, we can examine the amplitude and stability of the position of the dominant feature in our data, the "central-deficit" region, located at approximately 190° right ascension. This deficit region has also been observed by other studies and is a good marker to focus on given its large area, seemingly small variation in its position over time, and coherent behavior in adjacent dec. bands. The central-deficit region was chosen by eye and is defined as the area from $5^\circ - 35^\circ$ in declination and $160^\circ - 210^\circ$ in r.a. Averaging over this region in the seven year data set gives a value of (-2.85 $\pm$ 0.06 stat. $\pm$ 0.08 syst.)$\times 10^{-3}$ corresponding to a 19.9σ signal after the systematic and statistical errors are added linearly to be conservative.

4.2 Temporal Evolution

The apparent stability in position of the central deficit region over time is examined by plotting the average minimum in the declination bands corresponding to $5^\circ - 35^\circ$ for two month and yearly periods. The results are shown in Figures 4.6 & 4.7. The error bars on each minimum are calculated from a distribution containing 100,000 minima obtained by monte carlo simulation. The simulation takes the six parameters given by the fit to actual data for the dec. bands used above as the means of six gaussians with widths given by their associated errors. These gaussians are in turn used to randomly generate a new set of parameters which are used to create a simulated curve in which the minima are found and histogrammed. The r.m.s. of each histogram is calculated and interpreted as the statistical error on the minimum.

The systematic error is estimated as being equal to the statistical error which is approximately true for all of the data as is discussed in Section 5.0.6.

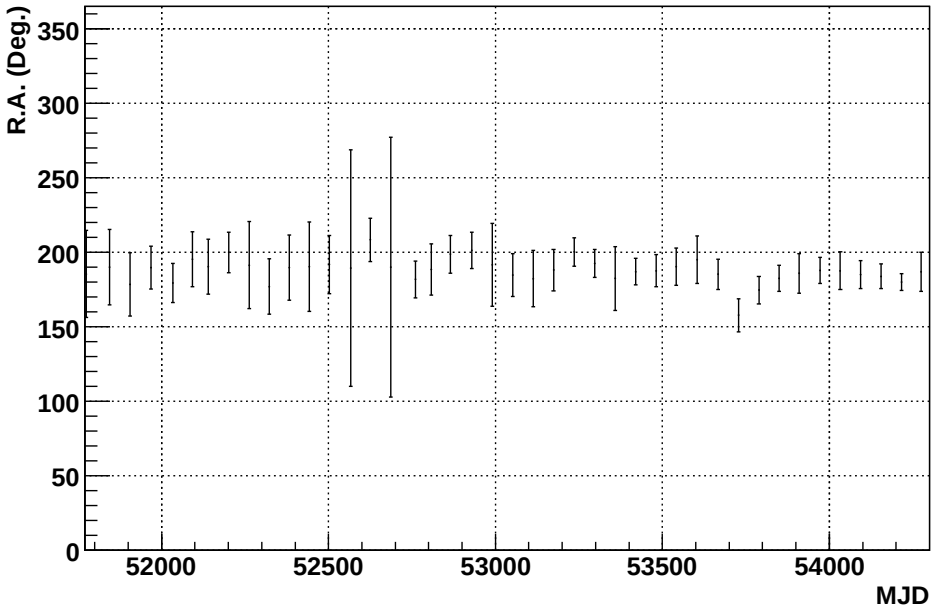

Figure 4.6: Position of minimum in degrees vs. median date of two month averages for a seven year period. The error bars are the linear combination of statistical & systematic.

As can be seen in Figure 4.6 the position of the valley is fairly stable throughout the seven year period. Fitting a constant to Figure 4.7 results in a mean of $188^\circ \pm 2^\circ$ with a $\chi^2/d.o.f. = 3.6/6$. This small variation over the yearly periods is what one would expect from a true sidereal feature.

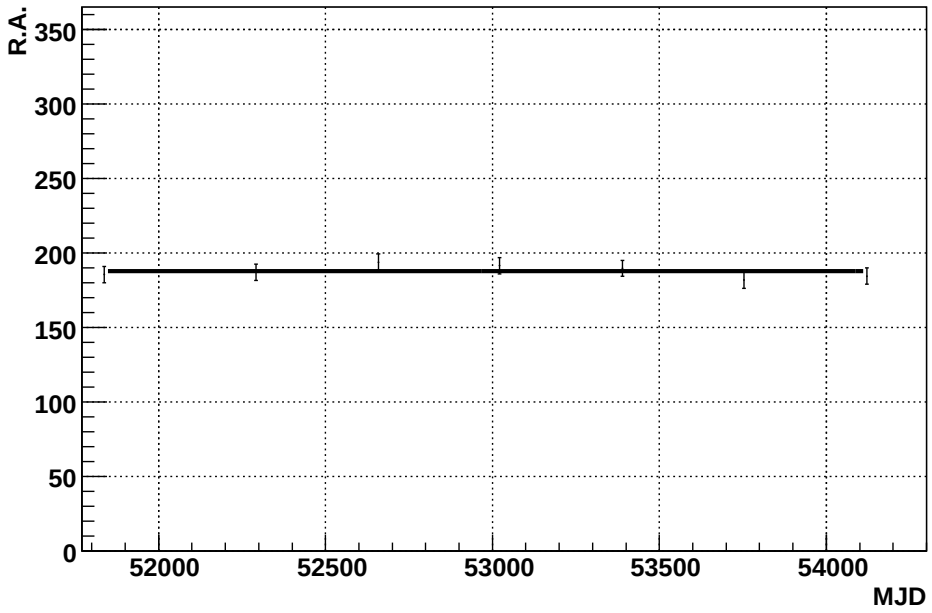

Figure 4.7: Position of the minimum anisotropy in r.a. averaged over declinations 5° to 35° for yearly sets from 2000-2007. The error bars are the linear combination of the statistical & systematic errors. The fit to a constant value is $188^\circ \pm 2^\circ$ The χ^2/ndf is 3.6/6.

Given this stability in position it is natural to examine the variation of the depth of the central-deficit region w.r.t. time. Figure 4.8 shows the variations for two month averages. In each of these plots the error bars are calculated by adding the statistical and systematic errors linearly in order to be conservative. The systematic errors are estimated using the procedures shown in Section 5.0.6. The errors make

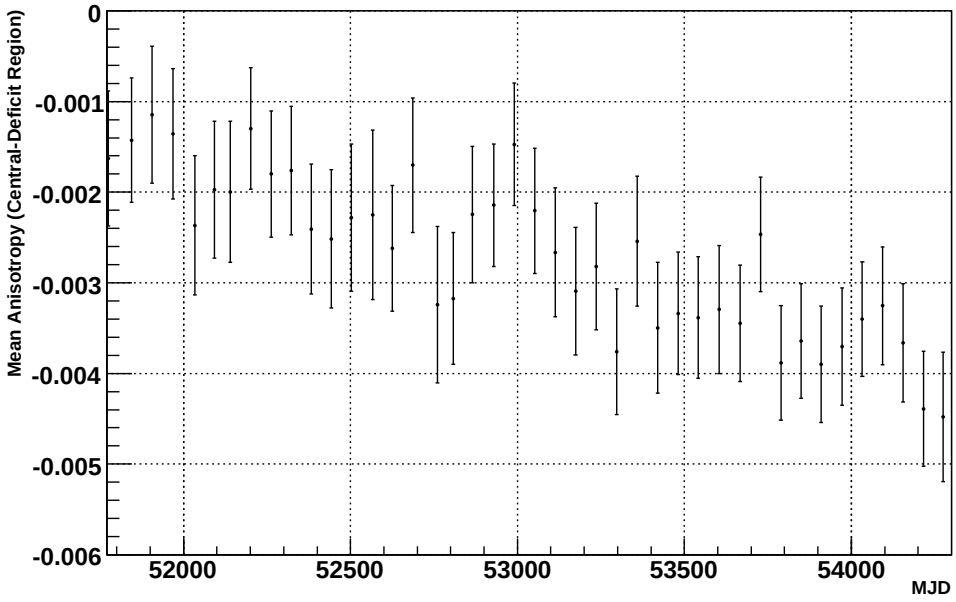

Figure 4.8: Average depth of the central valley vs. time for data sets consisting of two month periods.

it difficult to make any definitive statement about time evolution on this time scale although a definite trend is seen. For this reason we choose to focus on the yearly averages given that the contamination from other effects should be minimized as explained in Sec. 3.8. The central-deficit depth for the yearly averages are plotted in Figure 4.9. Included in this figure are the the results of a fit to a constant as well as a fit to a two-parameter linear function. Given the difference in χ^2 for the two fits it is clear that the two-parameter fit is much better and implies a definite temporal dependence.

Although it was stated in Section 3.2 that each declination band is to be treated as an independent observation, the averaging done in this temporal analysis is rea-

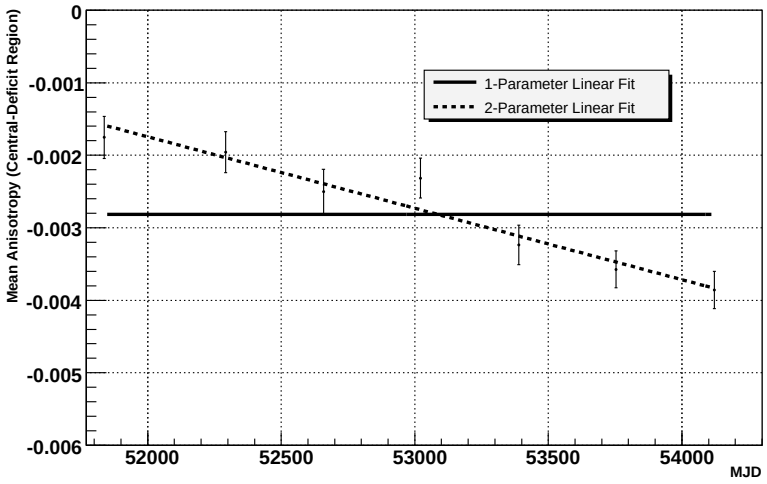

Figure 4.9: Mean depth of the central-deficit region vs. MJD for yearly sets from 2000-2007. The error bars are the linear sum of the stat. & sys. errors. The mean is taken from 5° to 35° in dec. and 160° to 210° in r.a. The solid line is the fit to a constant value and the dashed is the linear two-parameter fit. The χ^2/ndf for the fits are 54.6/6 and 3.4/5 respectively. The fit parameter in the flat case is $(-2.81 \pm 0.10) \times 10^{-3}$; the two fit parameters to the function $A(MJD) = p_0(MJD - 53000) + p_1$ are: $p_0 = (-9.85 \pm 1.38) \times 10^{-7}$ and $p_1 = (-2.73 \pm 0.10) \times 10^{-3}$.

sonable given that the depth and position in the various dec. band correlates with one another very well. This correlation can be seen in the position of the minimum for each independent dec. band (for yearly sets) seen in Figure 4.10 and in the time evolution of the depth for the same bands seen in Figure 4.11.

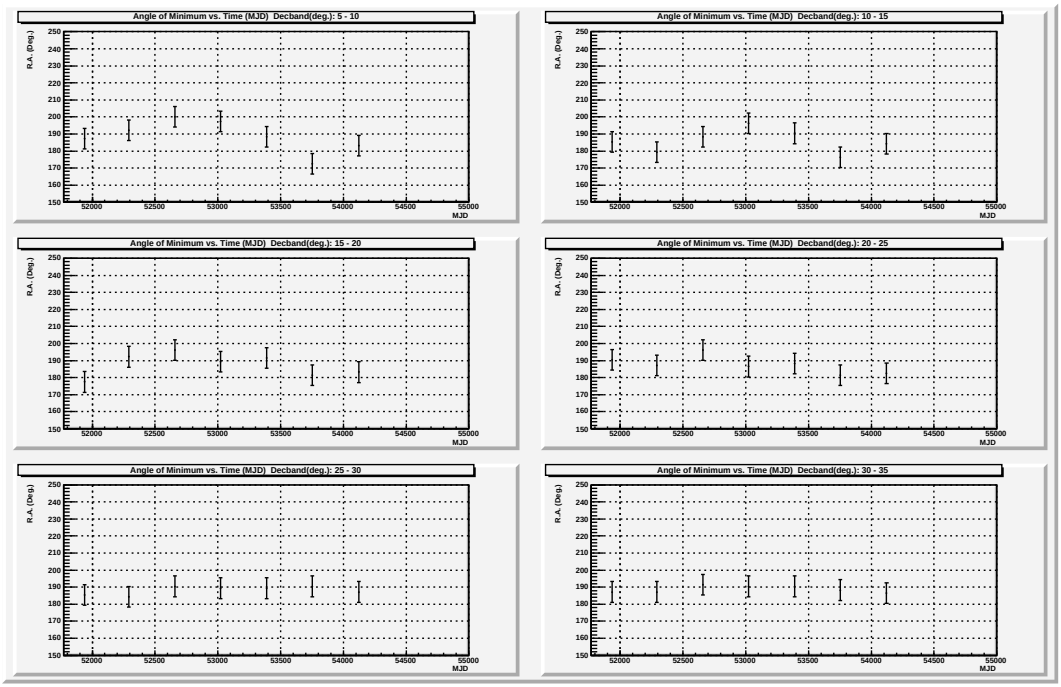

Figure 4.10: Position of minimum anisotropy in r.a. for the six individual dec. bands used in the calculation of the central-deficit region. The error bars are statistical + systematic.

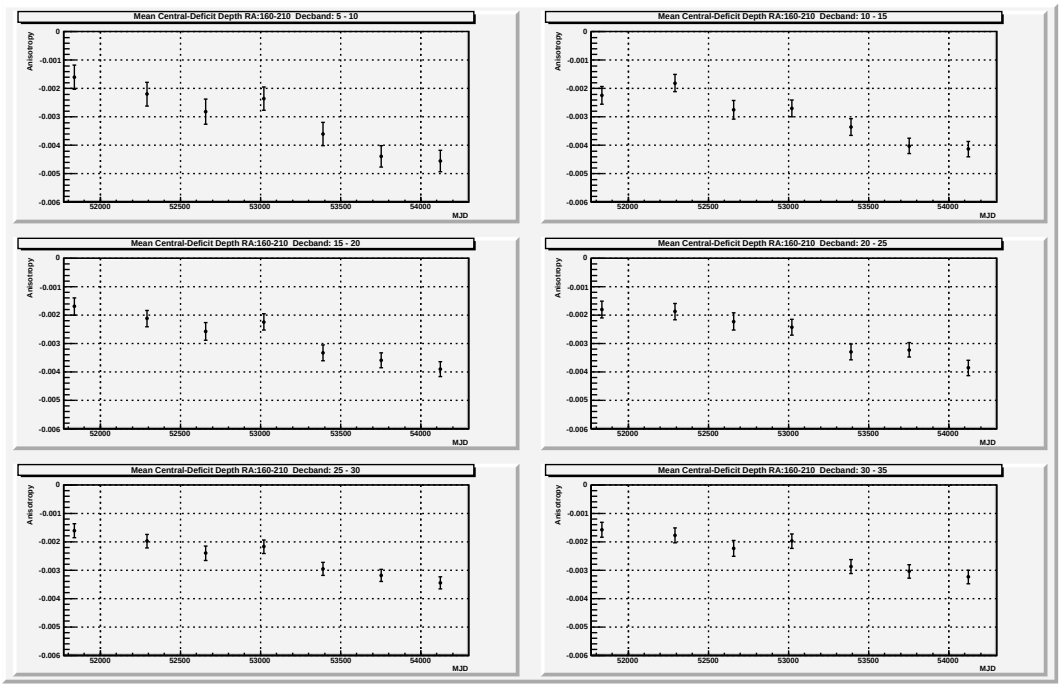

Figure 4.11: Value of the anisotropy at the minimum for the six individual dec. bands used in the calculation of the central-deficit region. The error bars are statistical + systematic.

In all of the plots there is a "deepening" of the anisotropy in this region while not showing a shift in position. There are two main concerns about these results:

- The yearly averages show a definite increase of almost a factor of two over the seven years. This is not consistent with the expectation of a time-invariant sidereal sky anisotropy.
- Are these results actually indicative of some "sky-physics" or are they the result of systematic effects?

These questions will be explored in Section 5.0.7.

4.3 Energy Dependence

In order to see whether the anisotropy depends on energy we bin the data according to an energy dependent parameter, natural log of the fraction of outriggers hit (ln(fOut)). Only the last four years of data can be included in this energy analysis given the outrigger array was not completed until 2003.

More specifically, the data is split into eight bins of width 0.5 in ln(fOut). The first bin has ln(fOut) < -3.5 and the last $-0.5 \leq$ ln(fOut) ≤ 0.0. In the calculation of fOut only the fraction of live photomultiplier tubes is considered.

The anisotropy is reconstructed for each of the eight ln(fOut) bins and the value of the central-deficit region is found as before. The result is shown in Figure 4.12(a).

In order to determine the correlation of ln(fOut) with energy a Monte Carlo simulation is performed. This Monte Carlo (outlined in Section 2.5) simulates the Milagro detector's observation of an event produced by cosmic-ray primaries composed

of elements from Hydrogen to Iron assuming fluxes and spectra given by the ATIC experiment [28]. For each ln(fOut) bin the simulated events are histogrammed according to energy. The median energy can then be calculated as well as the error on the median. The error is asymmetric and is calculated by finding the highest and lowest energies contained within the inner 68% of events. The correlation between ln(fOut) and energy is shown in Figure 4.12(b).

Visual inspection of the dependence of the central-deficit depth on ln(fOut) and of ln(fOut) with energy suggests an energy dependence of the anisotropy signal. If the fractional anisotropy in this region were independent of energy one would expect the data in Figure 4.12(a) to have a constant value, that is they should not depend on ln(fOut). Fitting Figure 4.12(a) to a constant gives a $\chi^2/d.o.f. = 50.5/7$ which is clearly a poor fit. The data are thus not consistent with no energy dependence.

The suspected energy dependence is examined by assuming a model of the total cosmic-ray flux composed of a background component, which is constant over the entire sky, and an anisotropic component; each of these components are assumed to have an energy dependence given by a power law. The equation for this model (for a given declination band) is therefore:

$$dN(E,\Theta)/dEd\Omega = \Phi_{CR}E^{-\gamma_{CR}} + \Phi_{Ani}E^{-\gamma_{Ani}}f(\Theta) \tag{4.1}$$

$N(\Theta,E)$ is the observed cosmic-ray counts as a function of r.a. (Θ) and energy (E) in a single dec. band. Φ_{CR}, γ_{CR} and Φ_{Ani}, γ_{Ani} are the fluxes and spectral indices for the cosmic-ray background and the anisotropy respectively. $f(\Theta)$ contains

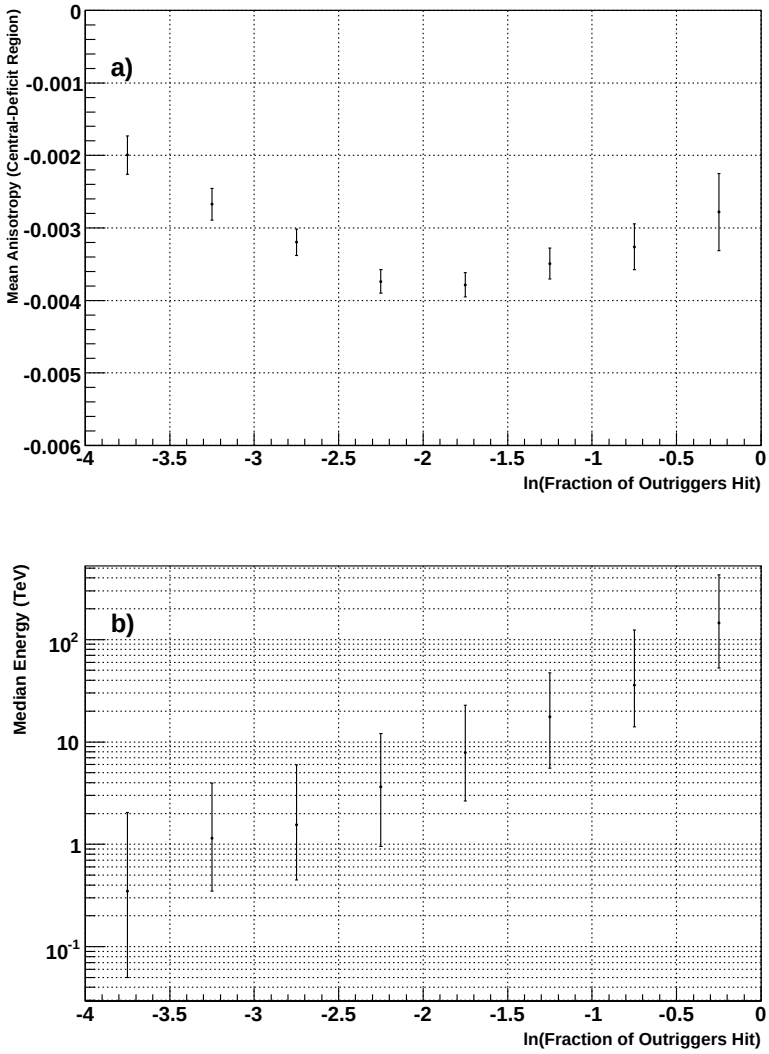

Figure 4.12: a) Mean depth of the central-deficit vs. ln(fOut) for data collected f rom 2004-2007. b) Median energy of Milagro triggered events passing cuts for the ln(fOut) bins shown above obtained from simulation. The asymmetric error bars are calculated by finding the highest and lowest energy containing the inner 68% of the total simulated events.

the r.a. dependence of the anisotropy component for a given dec. band. Since the central-deficit region we average over has a small extent in r.a. compared to the full sky, $f(\Theta)$ will be considered to have a constant value F.

This can be easily converted into a form giving the fractional difference from isotropic for the central-deficit region $A(E)$:

$$dA(E)/dE = \frac{dN(E,\Theta)/dE\,d\Omega}{\Phi_{CR}E^{-\gamma_{CR}}} - 1 = \frac{\Phi_{Ani}}{\Phi_{CR}}E^{-\delta}F \tag{4.2}$$

Where $\delta = \gamma_{Ani} - \gamma_{CR}$. As can be seen explicitly from this equation, if the spectral indices are equal the fractional anisotropy should be a constant. From the equation and the figure, the anisotropy in this region appears to be flatter than the cosmic-rays at lower energies and steeper at higher energies. In order to make a more quantitative statement we can perform a Monte Carlo simulation assuming a broken power-law (two different power-laws spliced together at some break energy) for the anisotropy in the equation given above. The output of this simulation gives the shape of the ln(fOut) distribution for different values of the break energy and δ above and below the break. A χ^2 optimization is then performed for the four fit parameters. The fourth parameter, $\frac{\Phi_{Ani}}{\Phi_{CR}}F$, is the normalization which is of no physical interest in this discussion and subsequently is always set to the value which gives the lowest χ^2 for any given triple of the other parameters. Since the correlation between ln(fOut) and energy is poor, especially at low energies, the determination of the break energy and power-law parameters is not highly significant. Figure 4.13 shows the one sigma χ^2 contours of the Monte Carlo simulated anisotropy fit to the observational data for different values of δ above and below, using the mini-

mum χ^2 of all break energies. Figure 4.14 shows the χ^2 vs. break energy as well as the χ^2 contours of the individual parameters vs. break energy. The best fit for this model gives a break energy of $E_{break} = 2^{+1.3}_{-1.0}$ TeV, $\delta = -2.7^{+2.1}_{-0.3}$ for energies below the break, and $\delta = 0.1 \pm 0.07$ for energies above the break (these errors are the single-parameter errors). Although these errors deviate from zero at less than two sigma, the anisotropy spectrum deviates from that of the nominal cosmic-ray background ($\delta_{below} = \delta_{above} = 0$) at the level of $\sim 5\sigma$. Repeating the simulation assuming a power law without a break, the fit becomes much worse. Figure 4.15 shows the observational data as well as the best fit to data for the broken power-law and non-broken power-law simulations. The optimal fit to the observed distribution for the broken spectrum gives a $\chi^2/d.o.f. = 0.33/4$ while the non-broken spectrum gives a $\chi^2/d.o.f. = 24.62/6$. An F-test yields a probability of 1×10^{-3} that the improvement in this χ^2 is due to random chance.

To see if there is a correlation between the temporal and energy dependencies, the last four years of data were split into five sets with integral ln(fOut), each containing events with ln(fOut) $\geq$ the following: -3.0, -2.0, -1.5, -1.0, -0.5. The yearly time dependence of the central-deficit region is calculated for these different integral ln(fOut) sets. The results are shown in Figures 4.16 through 4.20. In these plots the χ^2/ndf values are shown for a fit to a constant and a fit to a line of fixed slope. The fit to a constant is expected to become better as the median energy increases if the cause of the temporal dependence becomes less dominant at higher energies. The fit to a fixed slope is expected to remain good if the temporal dependence is completely independent of energy. The assumption made in this case is that the cause of the temporal evolution amounts to a modulation of the anisotropy over

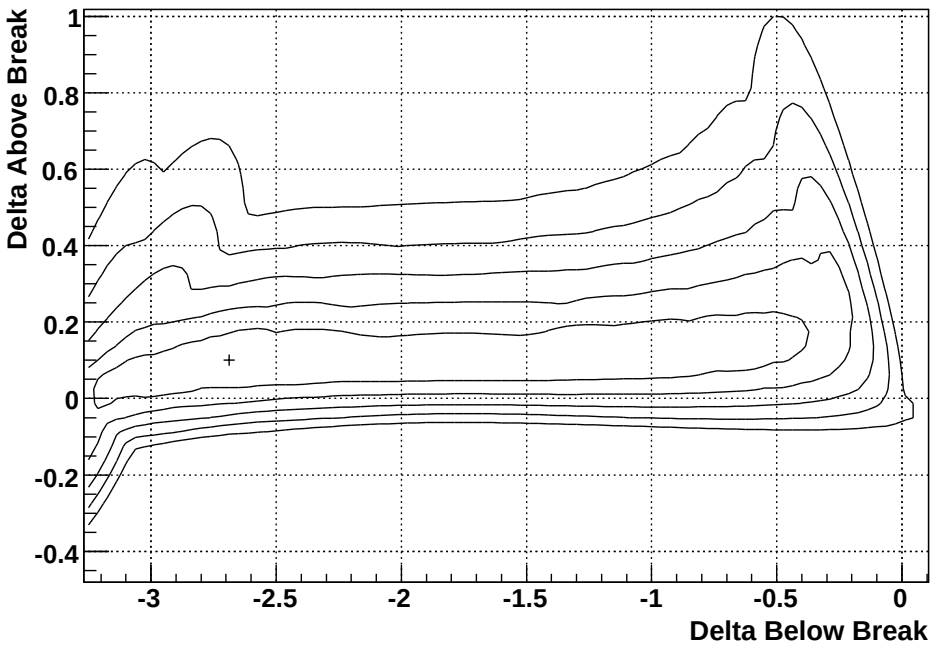

Figure 4.13: χ^2 contours corresponding to a probability content of 1 to 5 σ for 2 parameters ($\chi^2 - \chi^2_{min} = 2.3, 6.2, 11.8, 19.3, 28.7$) obtained from the fit of simulated fractional anisotropy vs. eight ln(fOut) bins to observational data. The delta parameter is defined as being the difference between the spectral indices of the nominal cosmic-ray background and the simulated anisotropy. The crosshair shows the location of the best fit.

time which results in the same percent change in the anisotropy for each ln(fOut) set. The slopes are calculated as following: the slope for the data with ln(fOut) $\geq$ -3.0 is fixed to be the value determined by the seven year data (given in Figure 4.9). In the subsequent four ln(fOut) sets, the slope in a given plot is calculated by scaling the slope of the seven year data by the ratio of the average value of the anisotropy in the plot of interest vs. the average value in the initial plot.

As can be seen in the figures, the fit to a line of fixed slope is always better than

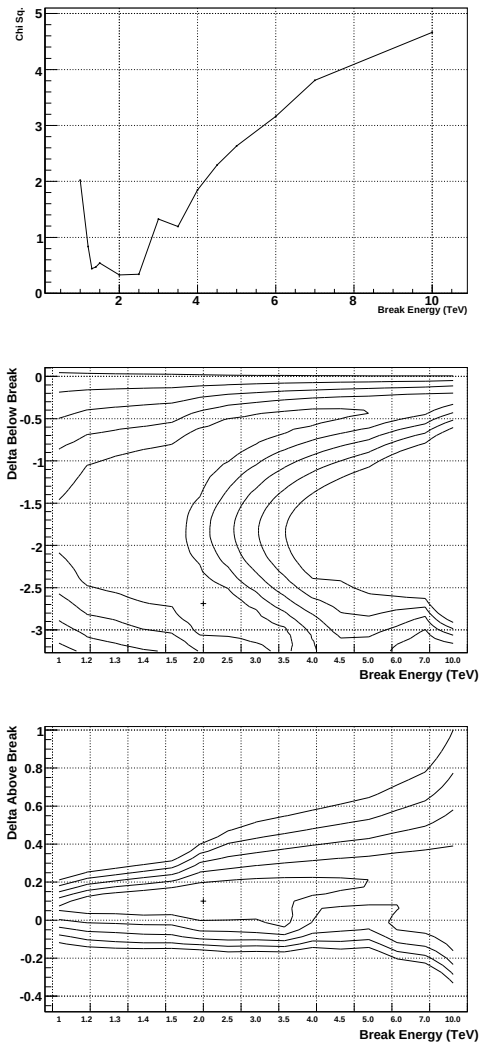

Figure 4.14: Top: χ^2 vs break energy. Middle: One sigma χ^2 contours (as defined in the previous figure) for delta below the break vs. break energy. Bottom: One sigma χ^2 contours for delta above the break vs. break energy. The crosshairs show the location of the minimum χ^2.

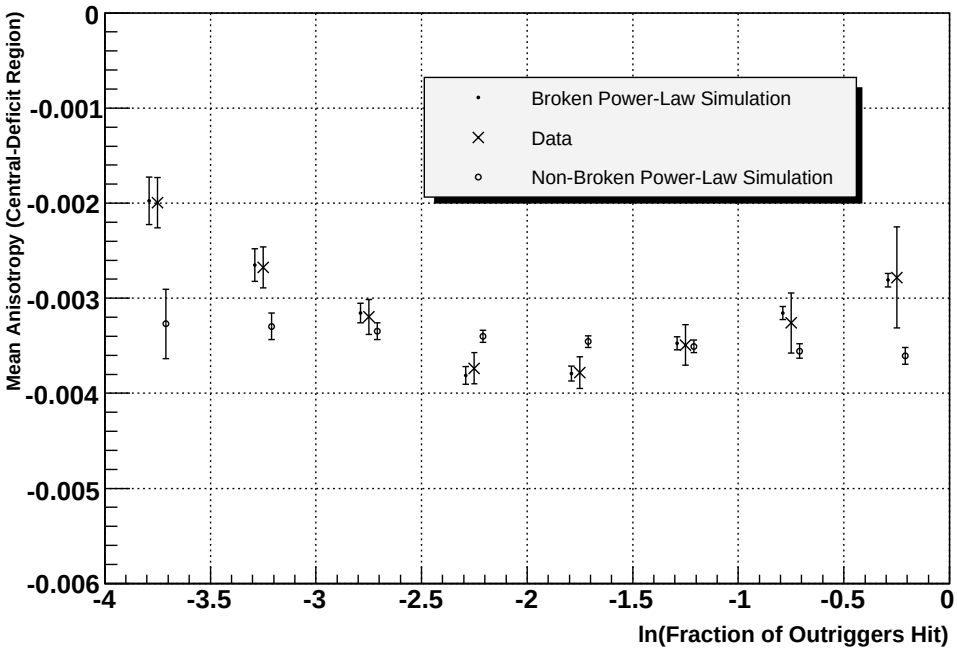

Figure 4.15: The best fit from simulation to observational data as well as the fit with no break (Note: the small separation of the values in the ln(fOut) direction is for visual purpose only). The values of the best fit are: $E_{break} = 2^{+1.3}_{-1.0}$ TeV; $\delta = -2.7^{+2.1}_{-0.3}$ below the break energy; and $\delta = 0.10 \pm 0.07$ above the break energy (all quoted errors are the single-parameter errors).

a fit to a constant. This implies that the cause of the temporal dependence is not dependent on the ln(fOut) parameter. However, since the errors grow large, this is not a very statistically significant observation.

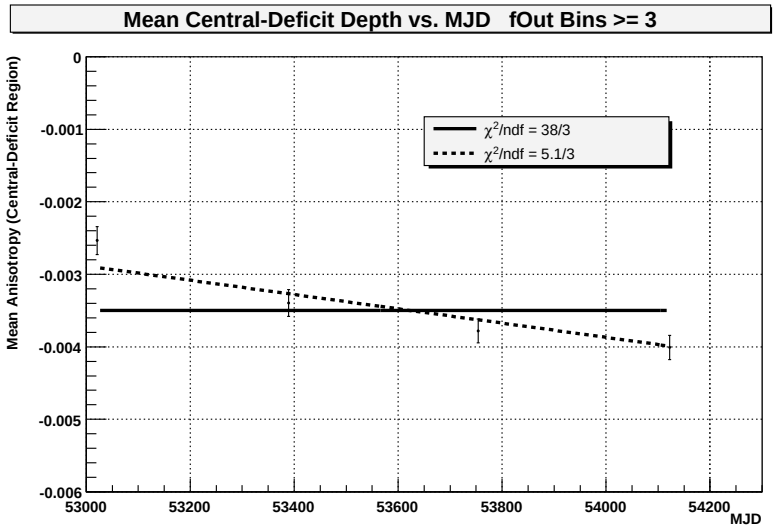

Figure 4.16: Mean anisotropy for the central-deficit region for the last four years of data consisting of events having ln(fOut) $\geq$ -3.0.

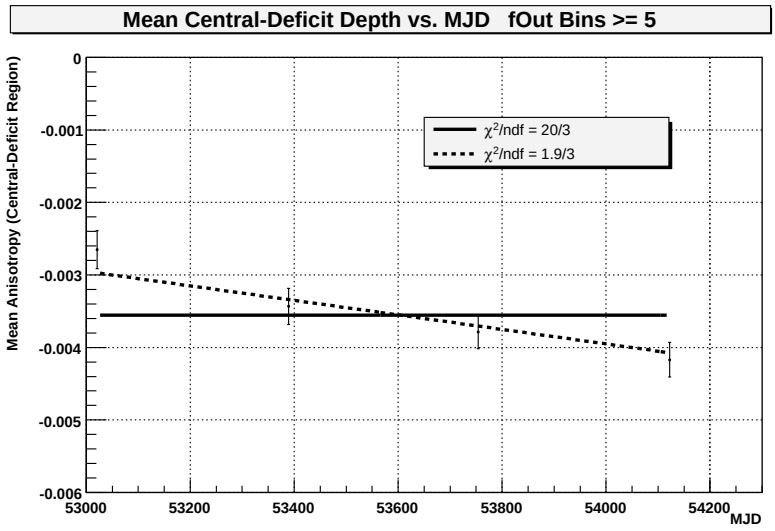

Figure 4.17: Mean anisotropy for the central-deficit region for the last four years of data consisting of events having ln(fOut) $\geq$ -2.0.

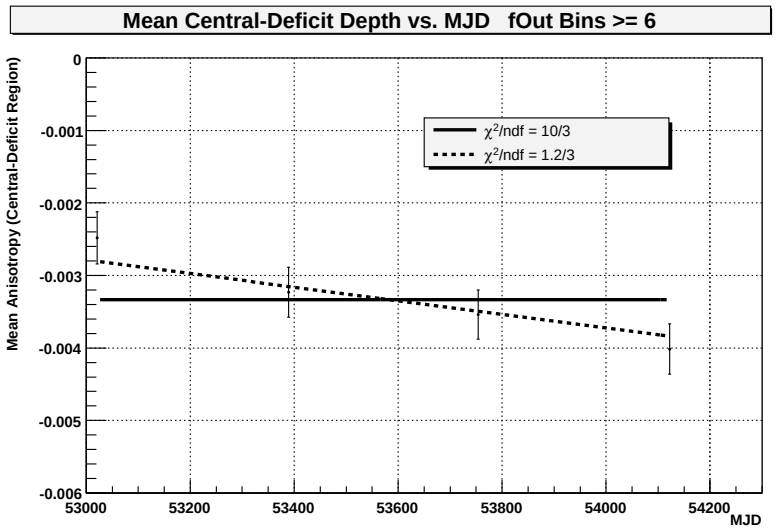

Figure 4.18: Mean anisotropy for the central-deficit region for the last four years of data consisting of events having ln(fOut) $\geq$ -1.5.

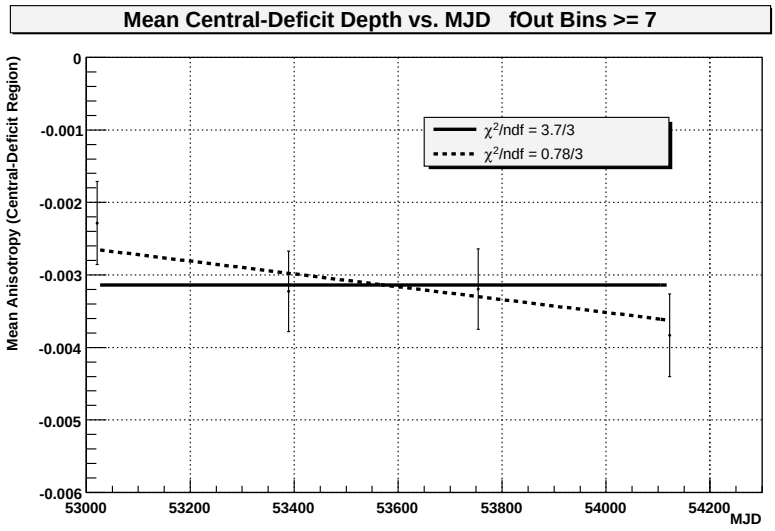

Figure 4.19: Mean anisotropy for the central-deficit region for the last four years of data consisting of events having ln(fOut) $\geq$ -1.0.

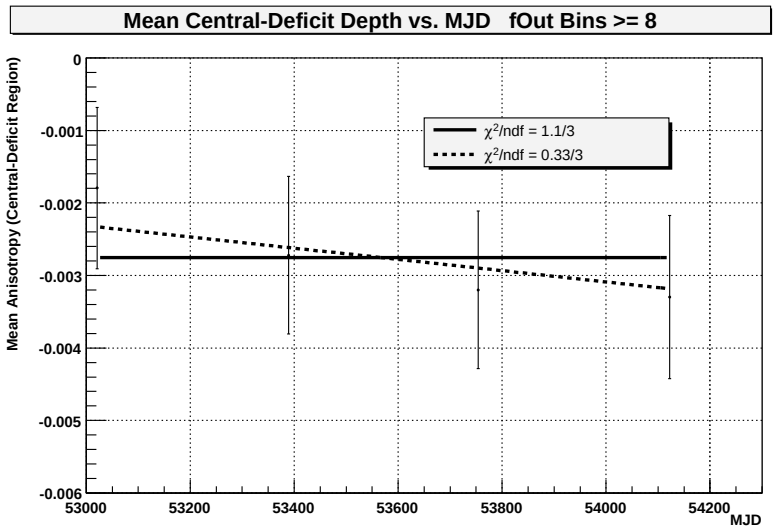

Figure 4.20: Mean anisotropy for the central-deficit region for the last four years of data consisting of events having ln(fOut) $\geq$ -0.5.

4.4 Compton-Getting Effect

Assuming an isotropic and homogeneous sea of cosmic-rays, the Compton-Getting (C-G) effect amounts to an anisotropy induced by the motion of the Earth around the Sun or the Sun around the Galactic center with an enhancement of the cosmic ray flux in the direction of motion (see Sec. 1.2.3). The C-G effect due to the Earth's motion around the Sun will appear as a UT dipole effect and is calculated to be 3.8×10^{-4} at Milagro's zenith (dec. of 36°) with a maximum at 6h universal time and a minimum at 18h.

As can be seen in Figures 4.21 and 4.22, the data shows an effect with an amplitude consistent with the solar C-G expectation. The phase is off slightly by about 1.5 hours. This could be due to day-night effects for which there is no cancellation. An observed UT anisotropy is always a superposition of the average daily variations due to atmospheric effects and the expected C-G effect from the Earth's motion around the Sun. It is noted that the expected and observed amplitude of the UT anisotropy is about an order of magnitude smaller than the amplitude of the observed sidereal anisotropy while the magnitude of the sidereal systematic effects are around the same size. A more thorough analysis of UT systematic effects is therefore needed to understand the phase difference. This analysis is deferred at this time.

In the case of the Sun's motion around the Galactic center the effect is more complicated. The Galactic cosmic-ray sea could in principle co-rotate with the Galactic magnetic field affecting the magnitude and direction of the C-G effect. In the instance of full co-rotation there would be no Galactic C-G effect. A measure-

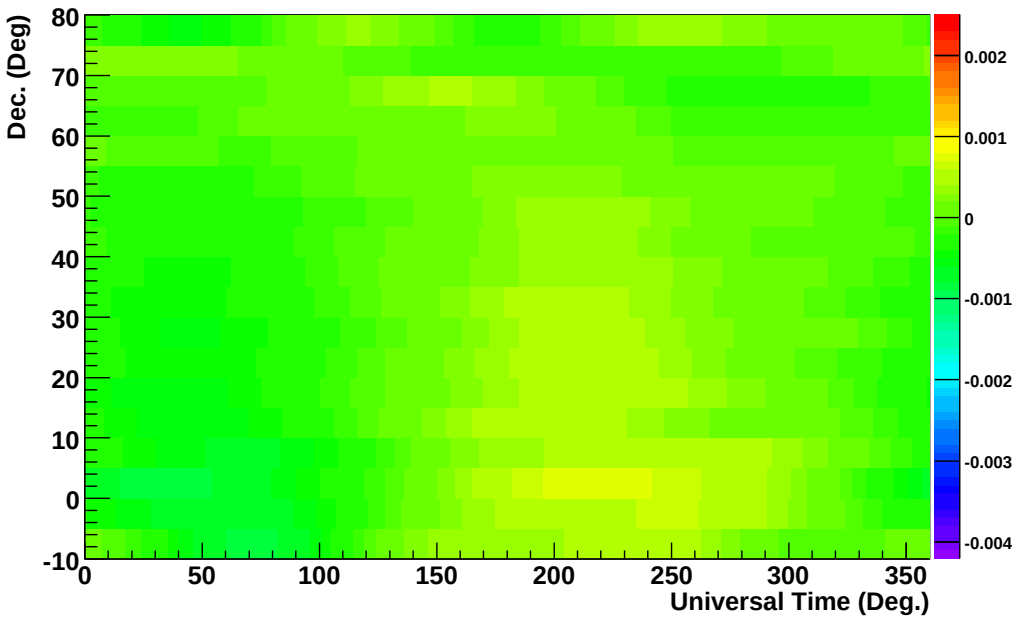

Figure 4.21: Map of the universal time anisotropy for seven years worth of data.

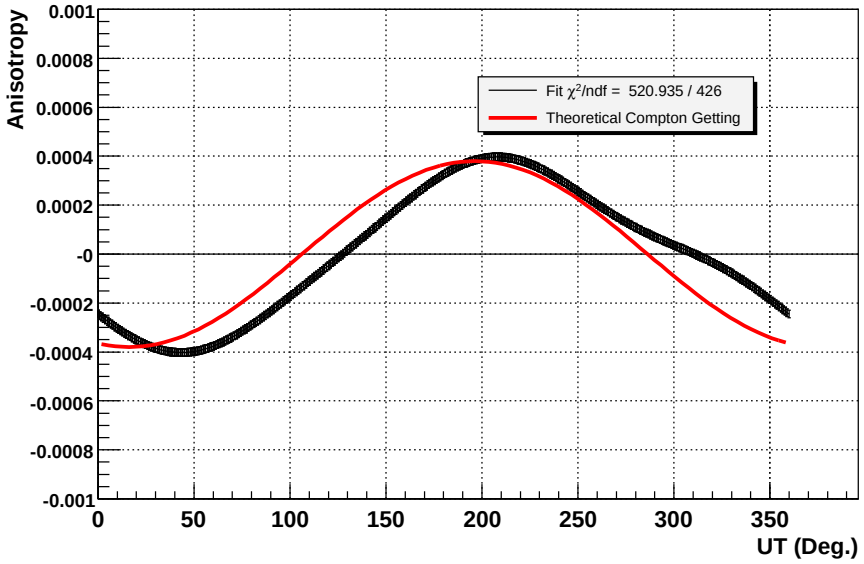

Figure 4.22: Anisotropy result for a fit to the all sky projection in universal time. The width of the black curve is the statistical error. The red line shows the theoretical prediction for the UT Compton-Getting effect and is calculated using the approximation that the CRs are observed only from Zenith (36° dec.).

ment of this Galactic C-G effect is more difficult given the fact that we see only measure the projection of the anisotropy in the r.a. direction. In order to understand how this affects the observation, a monte carlo was performed, using the technique outlined in Appendix A, for one possible set of parameters.

For this example the assumption is made that the cosmic-rays are isotropic and do not co-rotate with the Galaxy. Therefore the Sun's velocity in the Galaxy is the velocity used in the calculation of the C-G effect. In this case the magnitude of this anisotropy is calculated to be 0.35% given our speed of $\sim$ 220km/s. This dipole should then have a maximum at r.a. = 315° and dec. = 48°, and a minimum at r.a. = 135° and dec. = $-48°$. Figure 4.23 shows the theoretical value of the anisotropy with these parameters for the sky observable to Milagro.

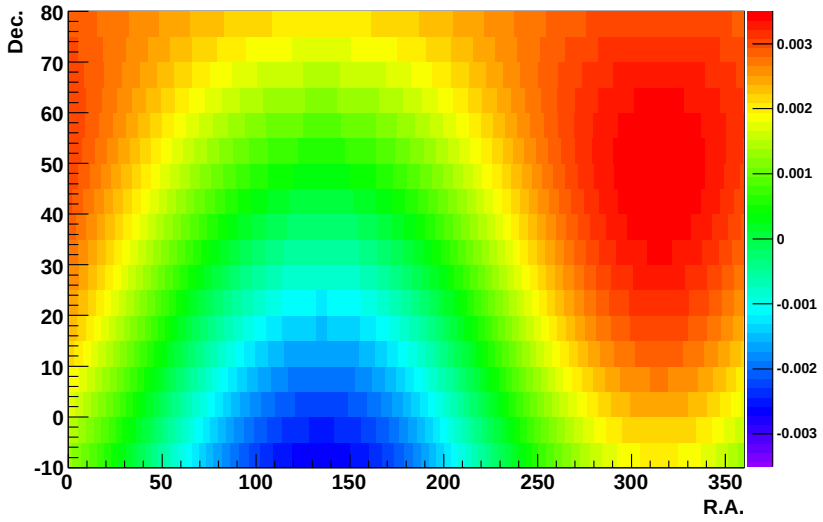

Figure 4.23: Map of the expected Galactic Compton-Getting effect as calculated from theory. See text for the parameters used.

This theoretical map is used as input to the monte carlo and the resulting one

year of simulated data is analyzed as the actual data would be. Figure 4.24 shows the result of this analysis.

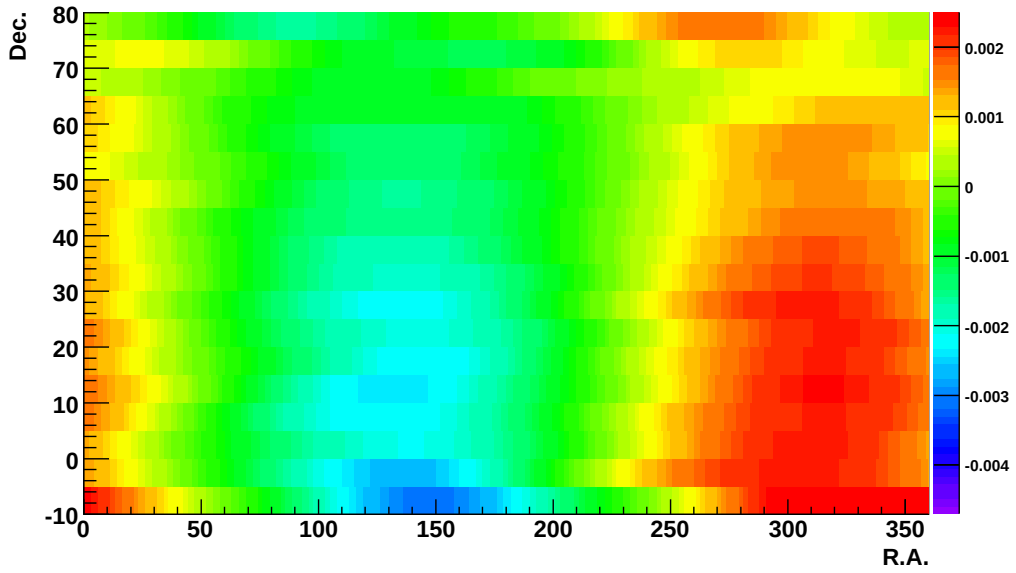

Figure 4.24: Map of the expected Galactic Compton-Getting effect created using one year of simulated data.

As can be seen, the dipole structure remains intact. The effect of looking at projections reduces the magnitude (to $\sim 0.14\%$) but retains the maximum and minimum directionality. Given that the dipole structure is not lost it is possible to test for the Galactic C-G effect by fitting a single dipole to the sidereal map. However, there is a large signal at lower declinations which would obstruct seeing this effect directly. To try and reduce effects from the central-deficit region, the dec. range from 50° to 60° is considered. Fitting a single harmonic to this region gives a $\chi^2/d.o.f. = 11505/998$ which is clearly a poor fit. Although this suggests that the observed anisotropy is not dominated by the galactic Compton-Getting effect,

its contribution to the anisotropy cannot be ruled out. It may be possible to remove other effects with measurements at high enough energy since the C-G effect is energy independent whereas the anisotropy in the central-deficit region appears to reduce with increasing energy.

Chapter 5

Systematic Checks

5.0.1 Monte Carlo Checks of the Analysis Method

To test the stability of the analysis method, monte carlo (MC) simulations, using the method described in Appendix A, were performed. All of the following MCs are simulations of one year's worth of data.

The first test run was a sky with no anisotropy. The output shows consistency with zero in all three time systems. There is some structure which appears in the highest declination band but from the profiles it is shown to be consistent with zero due to the large statistical errors. This fact supports what we suspect from the observed data in that the statistical power is limited in the highest and lowest dec. bands.

Taking the three year (2001-2003) sidereal map as input (Figure 4.4), the output is given in the following figure. There are no significant deviations between the two as can be seen also from the profile plots. The UT and AST time analyses are both

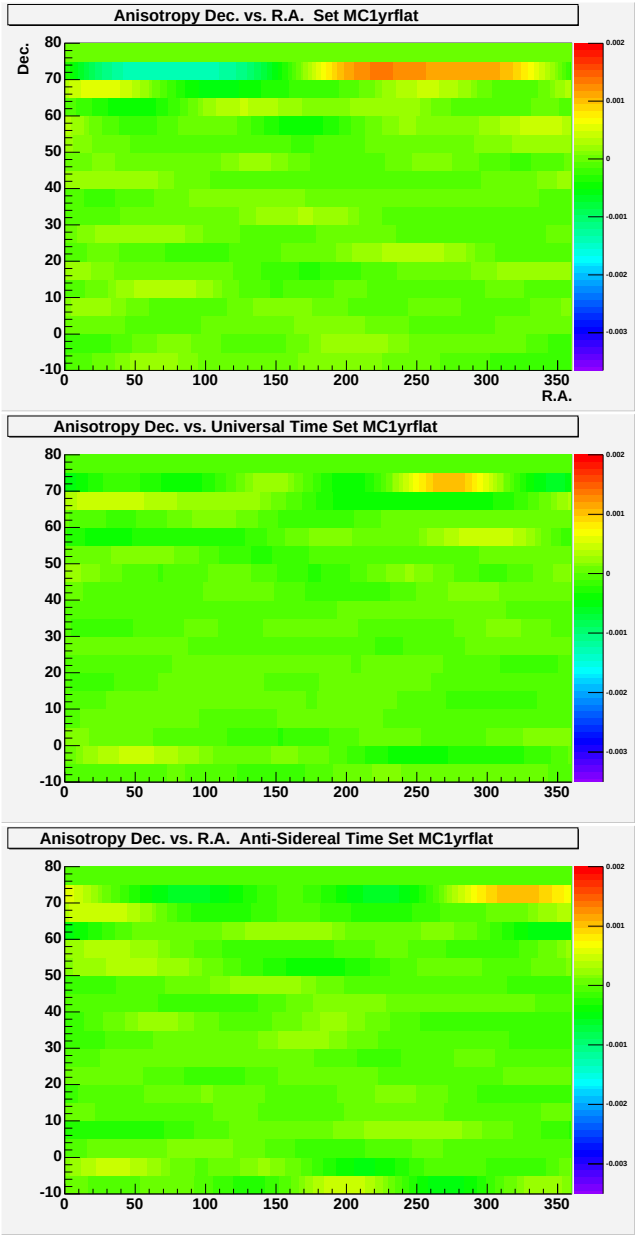

Figure 5.1: Sky maps of the fractional anisotropy generated using one year of monte carlo simulated data assuming no anisotropy. Top, middle and bottom are sidereal, universal and anti-sidereal respectively.

flat which is what one would expect from the fact that there was no UT or AST structure input in the MC and due to the use of one full year of simulated data.

The next MC is designed to check for induced effects caused by large input signals. As input the three year map in used in the previous test has every point scaled by a factor of five. The output shown in Figure 5.3 is consistent with the input.

In another Milagro analysis [30], an excess of gamma-rays is seen coming from the inner galaxy, dubbed the "Galactic Ridge". There is expected to be an enhancement in extensive air showers coming from this direction which could affect this analysis. To see how this Galactic Ridge enhancement affects the anisotropy, a MC input map is created with a 0.1 % anisotropy $\pm 5^{\circ}$ around the inner galactic plane. The output shows a slight effect, but it is smaller than that which was input. From this it is confirmed that the analysis method is less sensitive to features of the anisotropy which have small extent in r.a. This also shows that the flux from the galactic plane is not going to have a significant effect on the sidereal analysis.

To check on the possibility of the analysis inducing symmetry in the sky map, the three year map (2001-2003) is taken as input and altered so that everything located at an r.a. larger than 250° is equal to zero. The result reproduces the input showing that the symmetry observed in the seven year sidereal map is not a product of the analysis method.

The next tests involve creating a square hole of size -0.003 at Dec. $-10^{\circ} - 30^{\circ}$ and R.A. $150^{\circ} - 210^{\circ}$. This will give us a test of how the analysis deals with discontinuous features as well as gives a well controlled input with which to test UT effects. The sidereal square hole is shown Figure 5.6. The positive values of

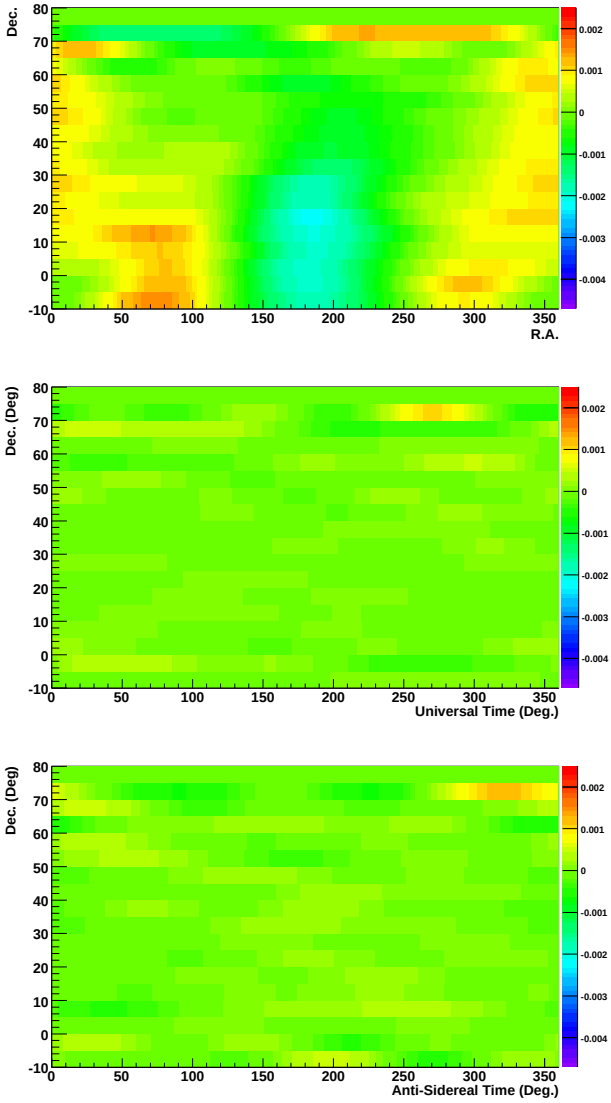

Figure 5.2: Sky maps for sidereal, universal and anti-sidereal time (top to bottom respectively) generated from one year of monte carlo data using the sky map of the first three years (Figure 4.4) as the true anisotropy.

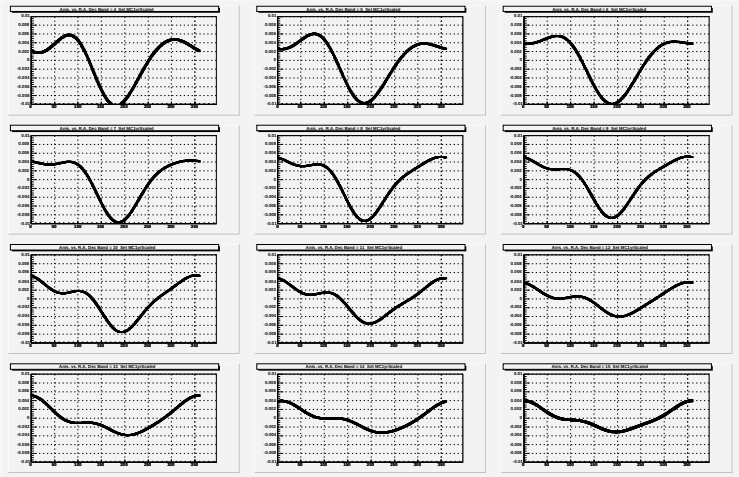

Figure 5.3: Dec. profiles of one years worth of monte carlo data using the first three years map (Fig. 4.4) scaled by five as input.

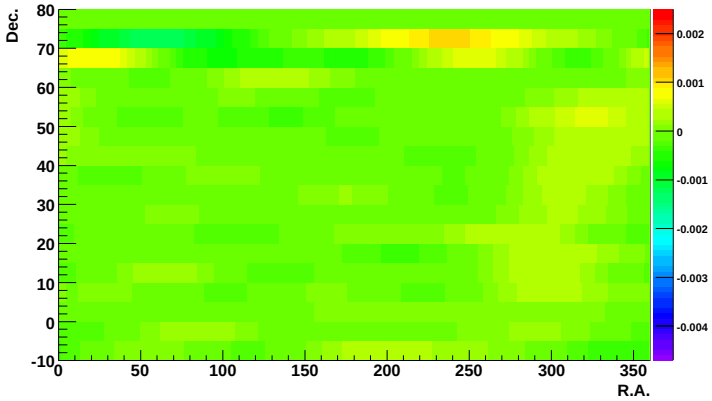

Figure 5.4: Anisotropy of one years worth of MC data taking as input a 0.001 fractional excess $\pm 5^{\circ}$ around the inner galactic plane.

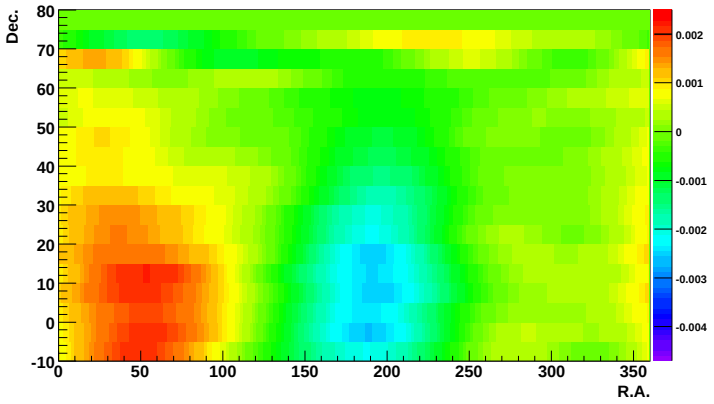

Figure 5.5: Monte carlo of first three year map with the anisotropy of the region with r.a. larger than the central valley set to zero.

the anisotropy in places where none was input are just artifacts of the discontinuity stemming from the use of three harmonics as is expected from Fourier theory.

Given that this plot was generated with one full year of simulated data we expect the sidereal effect to wash out in UT and AST. Any fixed point in sidereal time traverses the entire UT sky in one year and the AST sky in half a year. When we normalize each Dec. band these effects should disappear. Indeed they do as seen in Fig. 5.7. With this controlled input it is possible to explicitly see what happens on shorter time scales. The plots for $1/3$ year sections are given. Here we can see some of the sidereal structure “leaking” into the ”sidebands”, in the parlance of radio. The effect however is diminished and smeared out in r.a. as is expected. It is also clear in these three that when they are added together, forming a set of an integral number of years, the effect of structure on the sidebands will average to zero.

To see the effect of seasonal variations one final MC was run where the square

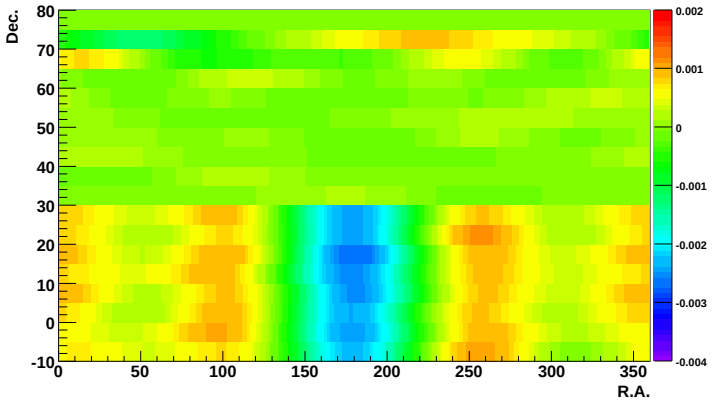

Figure 5.6: Sidereal map of m.c. data with a square hole of depth -0.003.

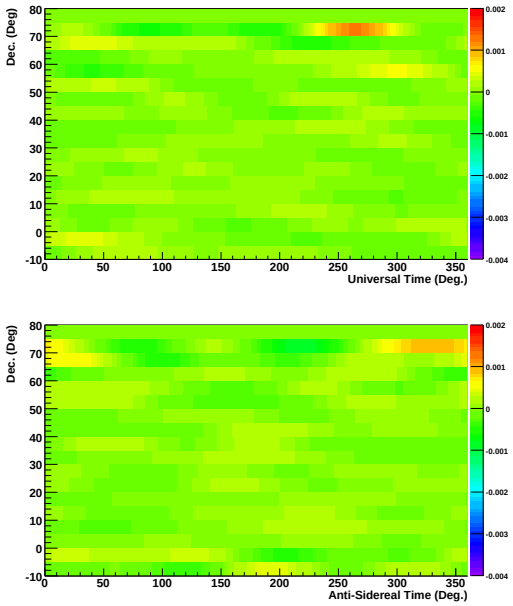

Figure 5.7: Universal and anti-sidereal maps from m.c. data using the sidereal square hole input.

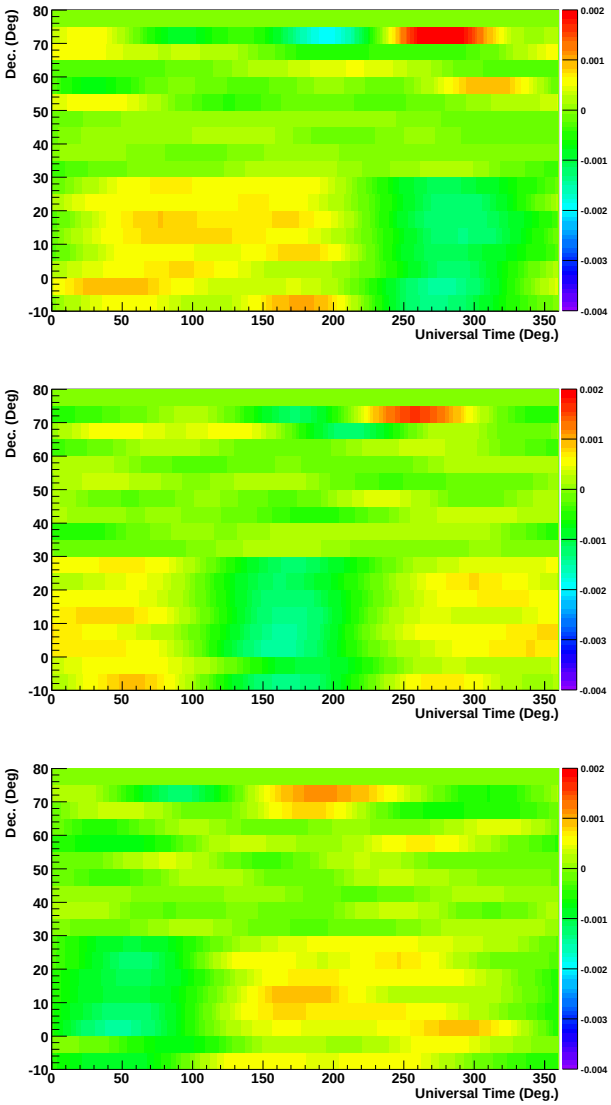

Figure 5.8: The same data as in the previous universal time plot but split into three four month periods.

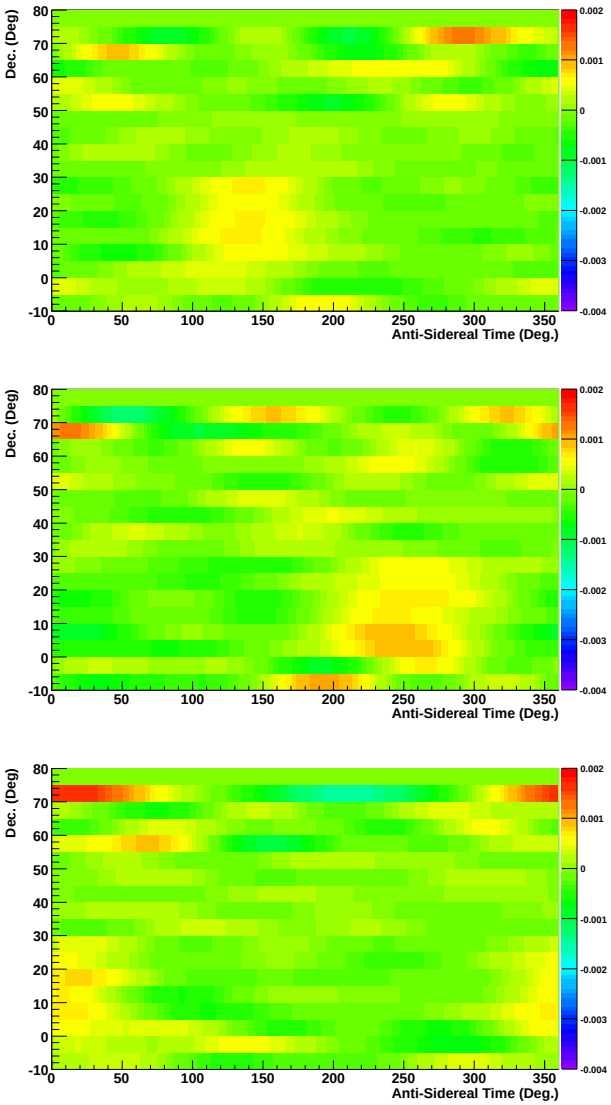

Figure 5.9: The same data as in the anti-sidereal plot above but split into three four month periods.

hole above is taken as a UT input rather than a ST input. The seasonal variation is modeled as a sine wave modulation of the amplitude with a period of one year. The depth of the square hole was chosen to range from 0.000 to -0.006 so that the mean value for one year would be about the same as the observed sidereal effect. From the plots we can see that now rather than the effect cancelling out in sidereal and AST plots there is some (small) residual effect. The consequence of this is that there will be some contamination of the sidereal plots due to weather effects. But the effect will be subdominant to the actual sidereal sky signal unless there is a tendency for the weather effects to "conspire" over the six year period to be coherent in sidereal time. From checks on the actual data this appears to be very unlikely. This does however show that a time dependent UT signal has the ability to contaminate the anisotropy present in the ST and AST time frames. This contamination is at the same level in both of these time frames but the phases are different. Since the AST time frame has no definite physical definition the phase is indeterminate. For this reason the contamination cannot be directly removed from the sidereal signal, but does allow for a way to estimate errors in the sidereal signal arising from UT systematic variations. This systematic error estimation will be explored in Section 5.0.6.

5.0.2 Stability of Fitting Procedure

In order to check the possibility that the large changes in the anisotropy are the result of an instability in the fitting procedure the data were split into two sets. The first is created by taking the odd numbered events and the second by taking the even. This splitting of the data yields two statistically independent data sets which

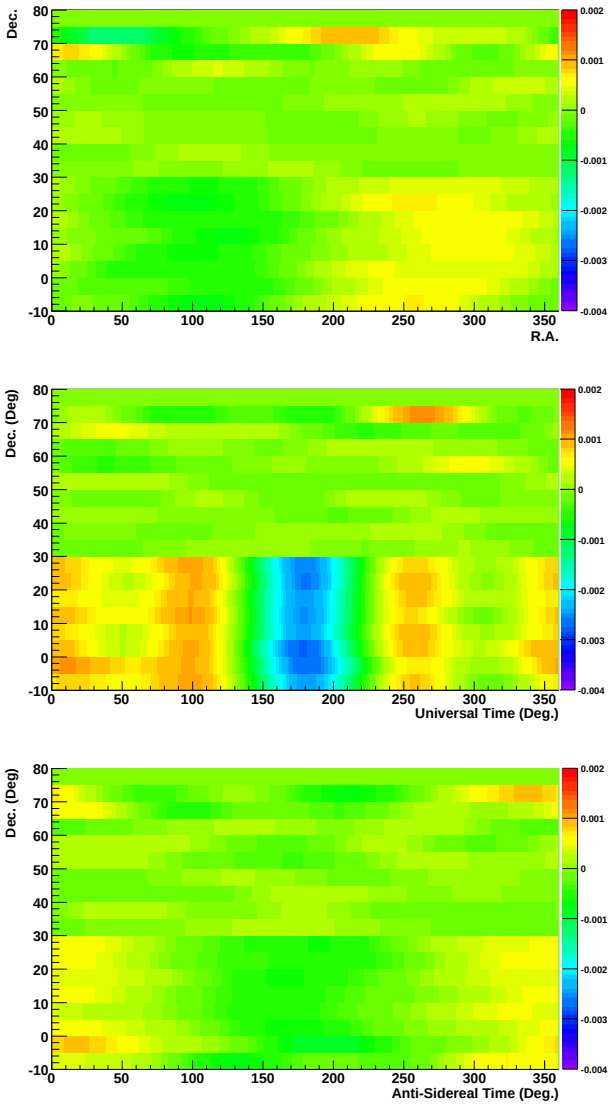

Figure 5.10: ST, UT and AST time maps for an amplitude modulated universal time square hole input. The AM has a period of one year and a range 0.000 to -0.006.

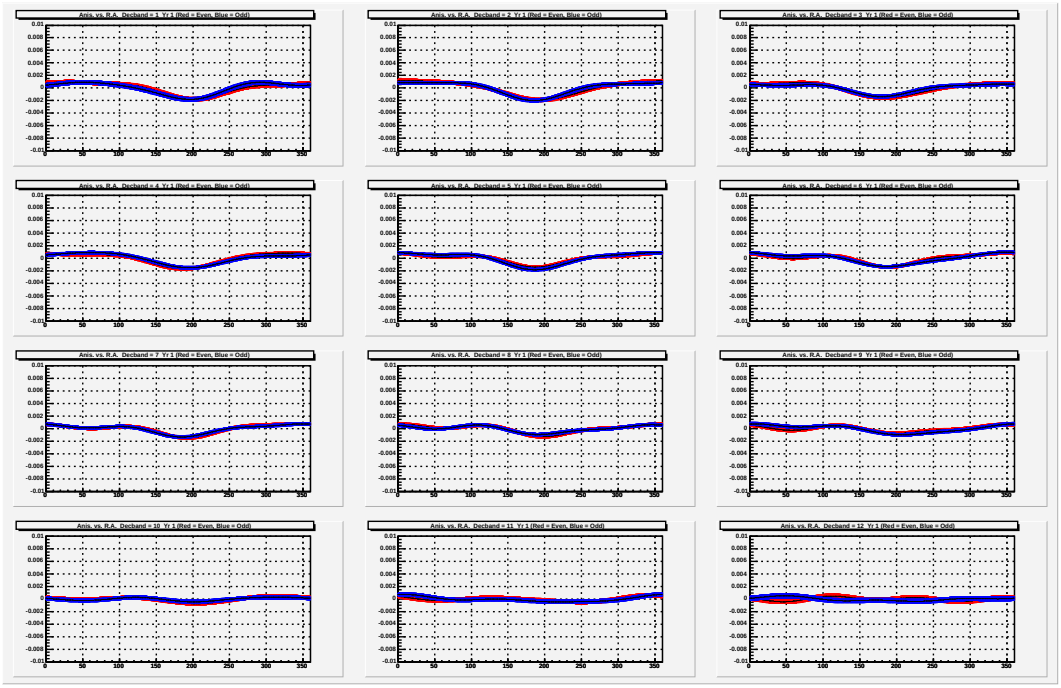

Figure 5.11: Declination profiles of the anisotropy for the first year of data. The red line is the even numbered events and the blue is the odd events.

are guaranteed to have been taken with the same signal and systematic effects. The profiles are given with the odd set as blue and the even as red for both the first and last years worth of data.

In both figures the anisotropy results of the two independent sets are identical with no differences larger than the statistical error (width of the curves). I conclude that the fitting procedure produces statistical errors which are reasonable when executed with data taken under the same conditions. This also implies that the changes in amplitude of the anisotropy observed are due to changes in the either the sky-signal or the atmosphere.

In Section 3.5 it is mentioned that the analysis method averages over differ-

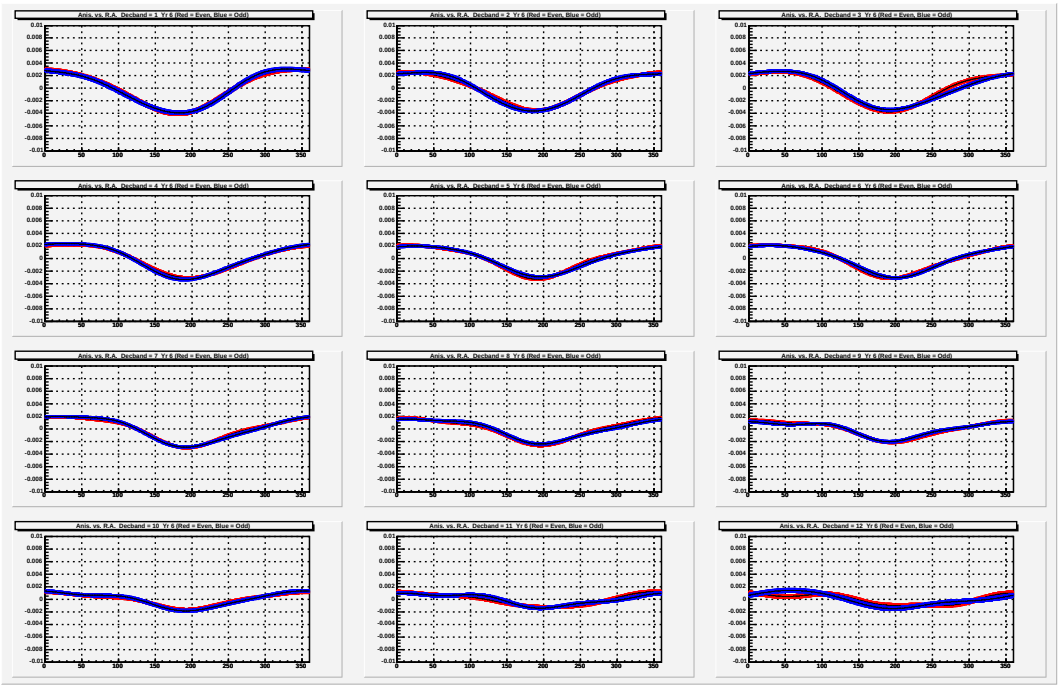

Figure 5.12: Declination profiles of the anisotropy for year six data. With red being even and blue being odd numbered events.

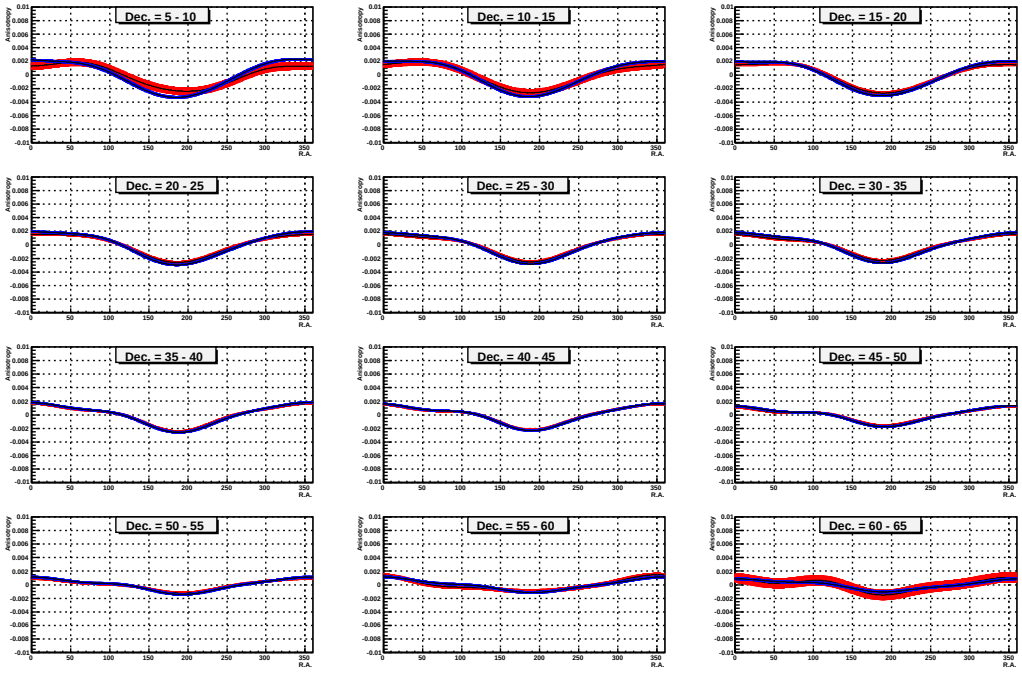

Figure 5.13: Declination profiles of the anisotropy for seven years worth of data. The red curve shows the result of the analysis for events with ξ from 0° to 25°. The blue shows the result for ξ from 25° to 50°.

ent values of the zenith angle ξ. Since the atmospheric depth is dependent on ξ (lower values of ξ translate to less atmospheric overburden than higher values), this amounts to an averaging over energy of the primary cosmic rays. To see if this has an effect on the analysis, the seven-year data were split into two sets: one containing events with a range in ξ from 0° to 25°, and the other with ξ from 25° to 50°. Figure 5.13 shows a comparison of the analysis results for these two sets. There is no difference between the two sets within statistical errors, therefore the procedure of averaging over ξ is considered well justified.

5.0.3 Stability of Sidereal Signal

In order to determine whether or not the observed sidereal signal (with it's constant phase) is an actual sidereal time effect, the minimum value of the anisotropy is examined in universal as well as anti-sidereal time for two month periods. In a two month period the differences would be expected to be slight, with a sidereal effect being "smeared" in universal time by about 60 degrees. In other words, taking a constant position in sidereal time, we can calculate where this point falls in universal and anti-sidereal time for a given two month period. Below are the plots of the minima in universal and anti-sidereal time with the theoretical prediction superimposed.

As can be seen the data agrees well with the expectation of a dominant sidereal effect. If, on the other hand, the UT (or AST) variations were dominant, there should be no correlation between the observed minima and the predicted "saw-tooth" curves. There are some deviations from the predicted values which could be attributed to weather or possibly solar effects. These systematic effects will be discussed in a later section.

5.0.4 Seasonal Effects

In order to check for coherent seasonal effects in the sidereal signal, I split the seven years worth of data into three "seasons". Winter-Spring (wisp) corresponds to the period between November and April. Spring-Summer (spsu) corresponds to April through July. Summer-Fall (sufa) corresponds to July through November. This particular definition of "seasons" was chosen as the three sets reflect average local

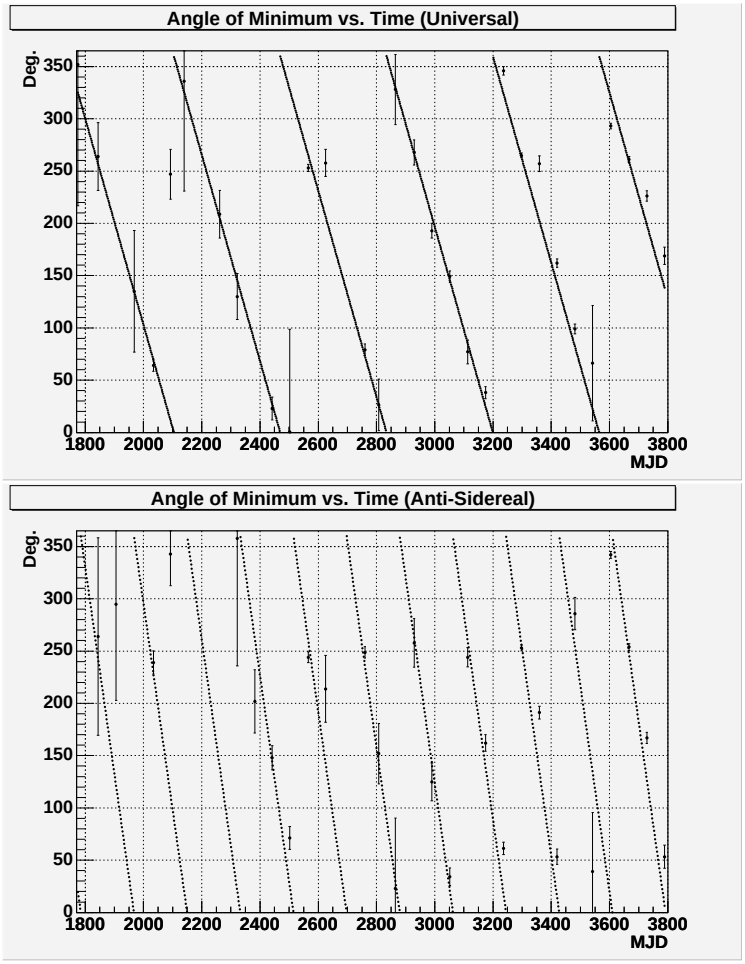

Figure 5.14: Universal and anti-sidereal plots of minimum vs. date for two month periods. The dotted lines are the theoretical prediction of an effect which is a constant in sidereal time located at 188° r.a.

weather periods of: ice and snow, warm with low precipitation, and high precipitation respectively. We can see in the sidereal plots that there is some difference between the seasons. The spsu period has a smaller overall effect than the others. Looking at the plots directly comparing projections of the anisotropy for the different seasons we see that these variations are not statistically significant.

5.0.5 Day/Night Separation

One can ask the question of how does the analysis differ when looking at data taken during daylight hours from data taken during nighttime hours? There is almost certainly a difference expected given the change in atmospheric conditions between these two periods. In fact, splitting the data like this should introduce a very large fake anisotropy. The two periods are set to be 10am-10pm ($\pm$1 hour) for daytime and 10pm-10am ($\pm$1 hour) for nighttime. Given these 12 hour sets are fixed in UT, this separation cannot be analyzed in the UT frame since a full 48 half hours is required for the analysis method to work. This analysis can be performed in ST and AST. As explained in Section 3.4, the data are organized in two month sets, each containing 48 half hour histograms in the ST and AST frames. The 24 half hour histograms, for the ST or AST frames, corresponding to the above day/night sets can be calculated for each two month period. Since a fixed point in UT traverses a full 24 hours in one year in both the ST and AST frames, by combining the appropriate 24 half hour histograms for each two month period over an entire year, the resulting data sets will be guaranteed to contain a full 48 half hours (in ST or AST) consisting of data collected only during daytime (or nighttime) hours. Figures 5.19 & 5.20 show declination profiles comparing the result of the sidereal (in red)

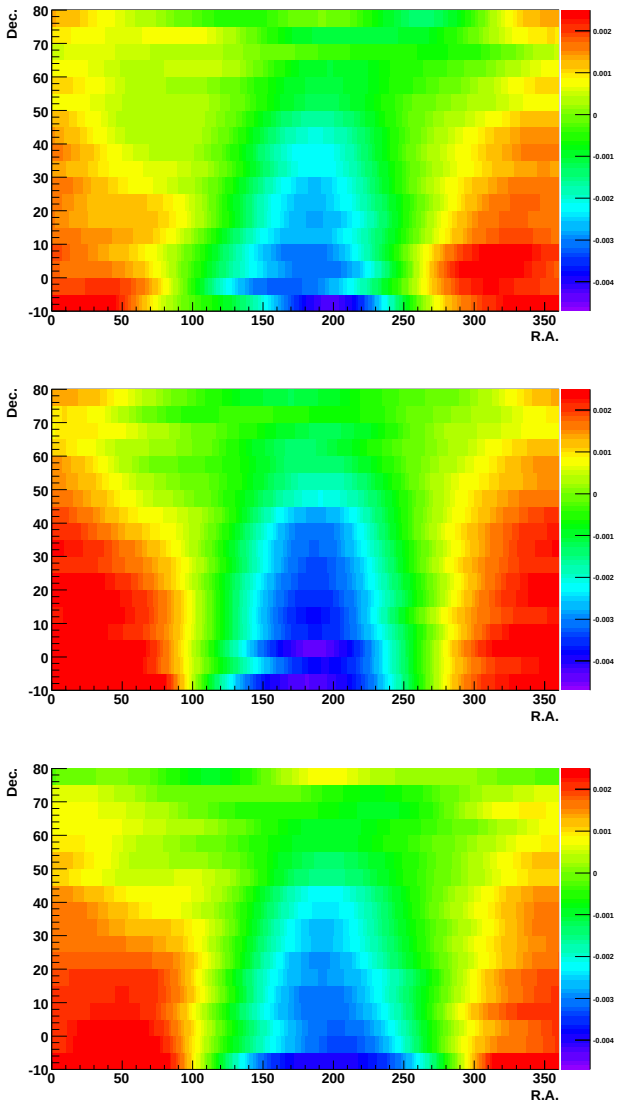

Figure 5.15: Sidereal time maps of seasonal data for the seven year data set. The maps are winter-spring, spring-summer, and summer-fall respectively.

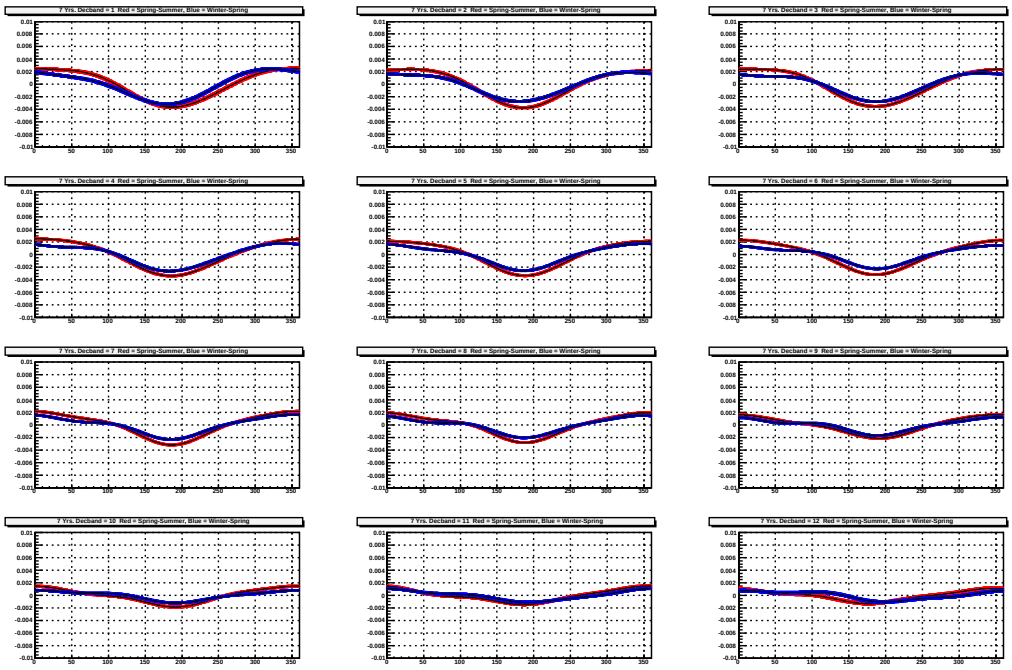

Figure 5.16: Sidereal profiles comparing seasonal data for the seven year data set. The red line is the winter-spring data. The blue curve is the spring-summer data.

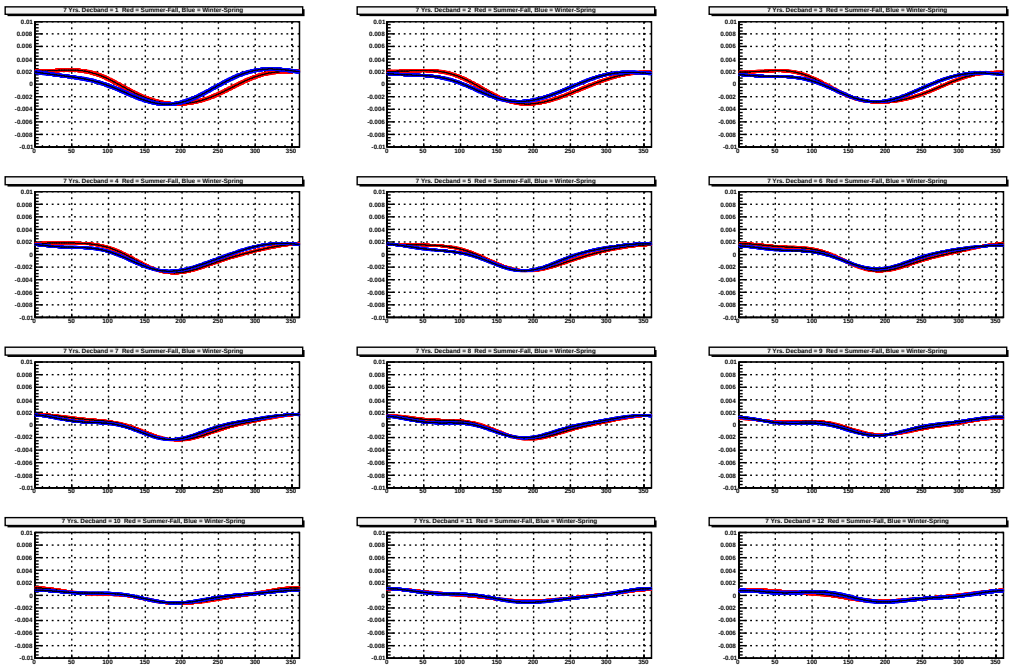

Figure 5.17: Sidereal profiles comparing seasonal data for the seven year data set. The red line is the winter-spring data. The blue curve is the summer-fall data.

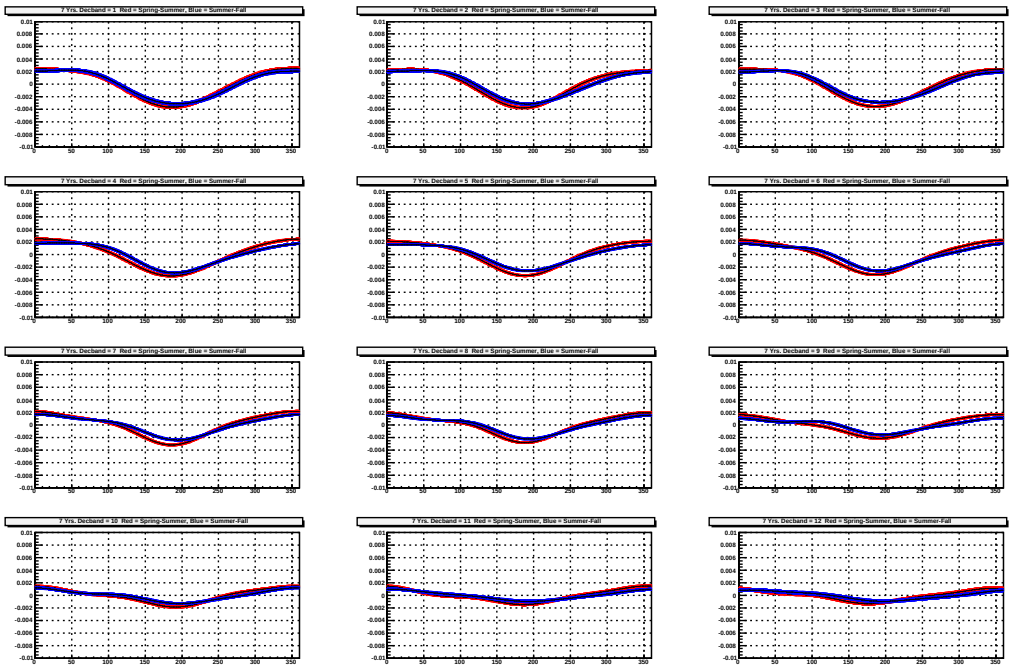

Figure 5.18: Sidereal profiles comparing seasonal data for the seven year data set. The red line is the spring-summer data. The blue curve is the summer-fall data.

and anti-sidereal (in blue) analyses for daytime and nighttime respectively using data from 2006 (as an example). In these plots the X axis serves dual purpose for both ST and AST and are plotted together to show the relationship between the signals. As can be seen the sidereal anisotropy has changed by a large amount, in both amplitude and phase. Also the anti-sidereal strength roughly reflects the magnitude of this difference for the expected year six amplitude ($\sim 0.35\%$). The reason for this change is that by splitting the data into these sets, there has been an introduction of a bias. The event rate independence of the FB method has been destroyed. Take for example a seasonal drift of event rate, due to the appearance of ice for part of the year for instance, since this drift is not averaged out by using a full 24 hours (of ST or AST data) during this period, an artificial anisotropy is induced by this rate drift since a given set of 24 ST half hours (or AST half hours) comes from different parts of the year. The important result of this analysis is that it confirms that time dependent systematic effects leading to an artificial sidereal signal will also lead to an analogous anti-sidereal signal. The use of the anti-sidereal signal in the estimation of the systematic errors is the topic of the next section.

5.0.6 Systematic Error Estimation

There are two sources of fake anisotropy signals in the averaged data, both from atmospheric effects. Coherent and seasonally varying UT variations, discussed in Sections 5.0.1 and 5.0.4, and the residual anisotropy due to the daily, random atmospheric effects. Both will show up with the same signal size in the AST and ST frames.

In Sections 3.2 & 5.0.1 it is explained that the anti-sidereal analysis should

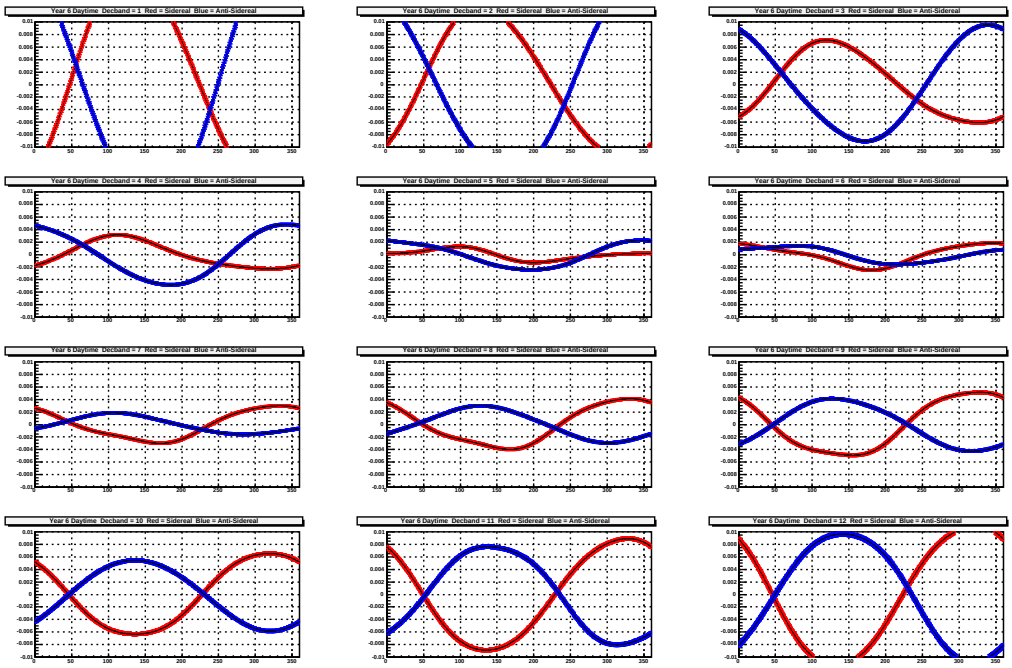

Figure 5.19: Declination profiles of the anisotropy for the year 2006 using data collected between the hours of 10am and 10pm ± 1 hour local UT. The red curve is the sidereal signal and the blue the anti-sidereal.

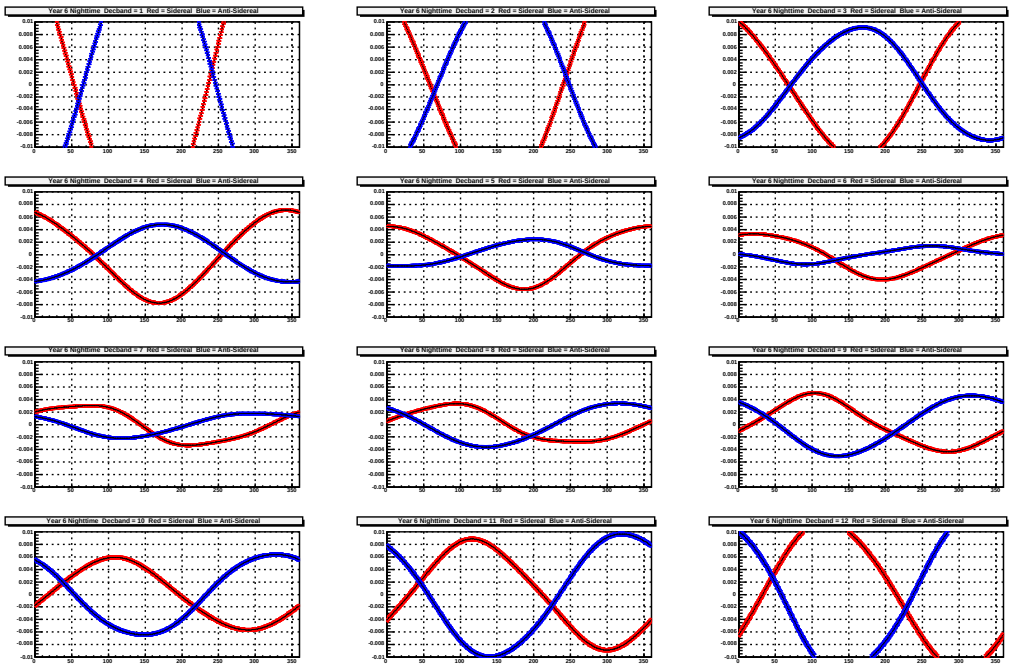

Figure 5.20: Declination profiles of the anisotropy for the year 2006 using data collected between the hours of 10pm and 10am ± 1 hour local UT. The red curve is the sidereal signal and the blue the anti-sidereal.

show no structure given that AST corresponds to no physical co-ordinate system. If there are large UT effects that are localized in time there will be some signal that could ”leak” into this time frame and that this signal can be used to estimate the systematic error. Since the observed sidereal signal is fairly stable and only shows a variation over long time scales, any AST signal is expected to be mainly due to UT (or random) effects. The plot below shows there to be some structure of the order of $\pm 10^{-4}$. for the seven year data set, much smaller than the sidereal signal.

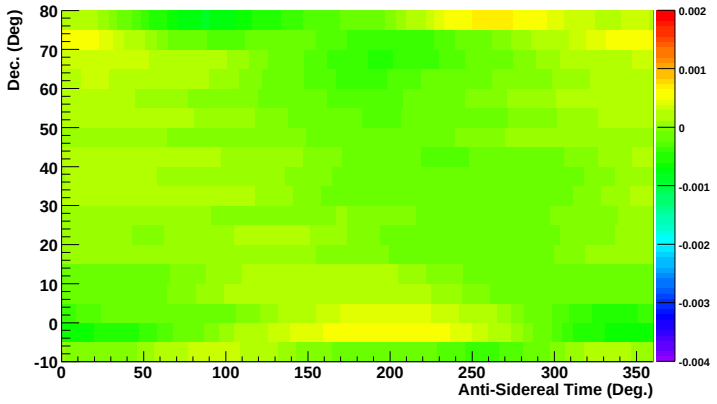

Figure 5.21: Map of the anti-sidereal time anisotropy for seven years worth of data.

Since the known AST signal cannot be directly translated to ST, given the unknown phase difference, all possible phases are considered. To convert this AST signal to a systematic error on the sidereal signal we project the AST signal for a given dec. band along the anisotropy axis and take the r.m.s. An example for $35^\circ \leq$ dec. $\leq 40^\circ$ is shown in Figure 5.22. The systematic error estimated is seen to be of the same order as the statistical error on the sidereal signal. This is further confirmation that the analysis method is effective at dramatically reducing structure due

to detector variations.

To better understand the behavior of the systematic effects, the data were split into sets of different time lengths. Figure 5.23 shows a sample of nine consecutive single day anisotropy projections for $35^\circ \leq$ dec. $\leq 40^\circ$. On this time scale there is no discernible difference between ST, UT, and AST in this analysis given that each of these time frames differ by $\sim 1^\circ$ in hour angle. It is seen that the variations are almost an order of magnitude larger than the observed sidereal signal. These variations are interpreted as being due to changes in the detector (including atmospheric variations) and form an unavoidable systematic error in the results of the longer data sets. Since these variations are largely incoherent the residual error arising from them should exhibit $1/\sqrt{N_{days}}$ behavior as expected from basic statistical analysis.

The systematic error can be estimated for sets containing an integral number of years by using the AST procedure previously described, which in essence randomizes the phases of the ST signal. For smaller time periods another method must be used given the contamination from other time frames. In this instance I have taken 60 single day anisotropy projections and averaged them together after randomizing their phases. Any coherent signal will be lost and only the random variations should remain. The r.m.s. of these variations are interpreted as the systematic error for the two month time period. Figure 5.24 shows the observed systematic error for multiple time scales as well as the expected error calculated by extrapolating the seven year value to shorter scales using the $1/\sqrt{N_{days}}$ behavior. The rough agreement between the expected and observed errors show that this is the dominant systematic error in the anisotropy results.

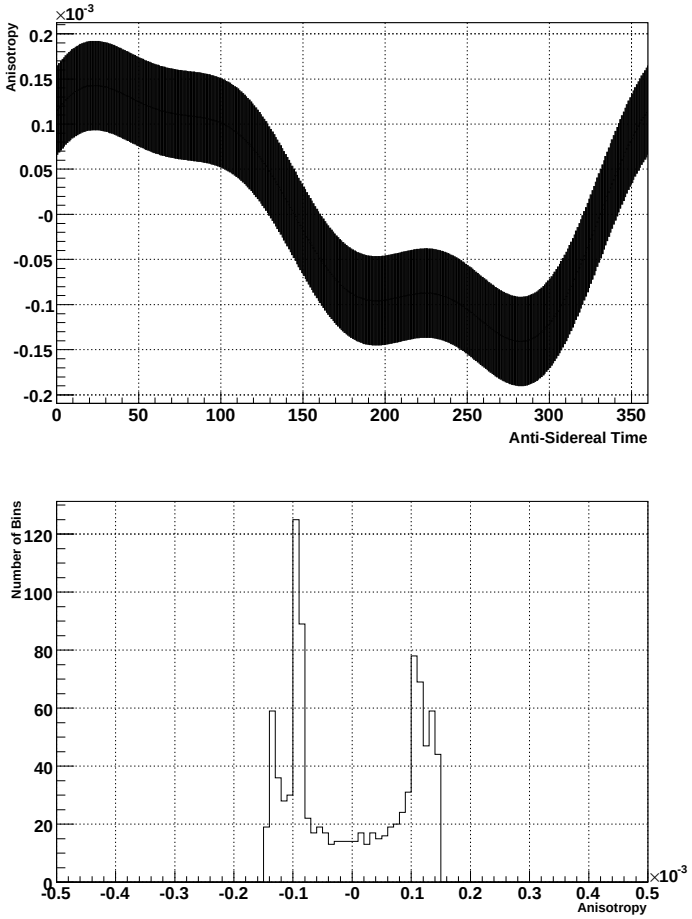

Figure 5.22: Top: Profile of the anti-sidereal time anisotropy for seven years worth of data at dec. from 35° to 40°. Bottom: Projection of above signal onto anisotropy axis. The r.m.s. of this plot is 1.00×10^{-4} which gives the estimate of systematic error for this dec. band.

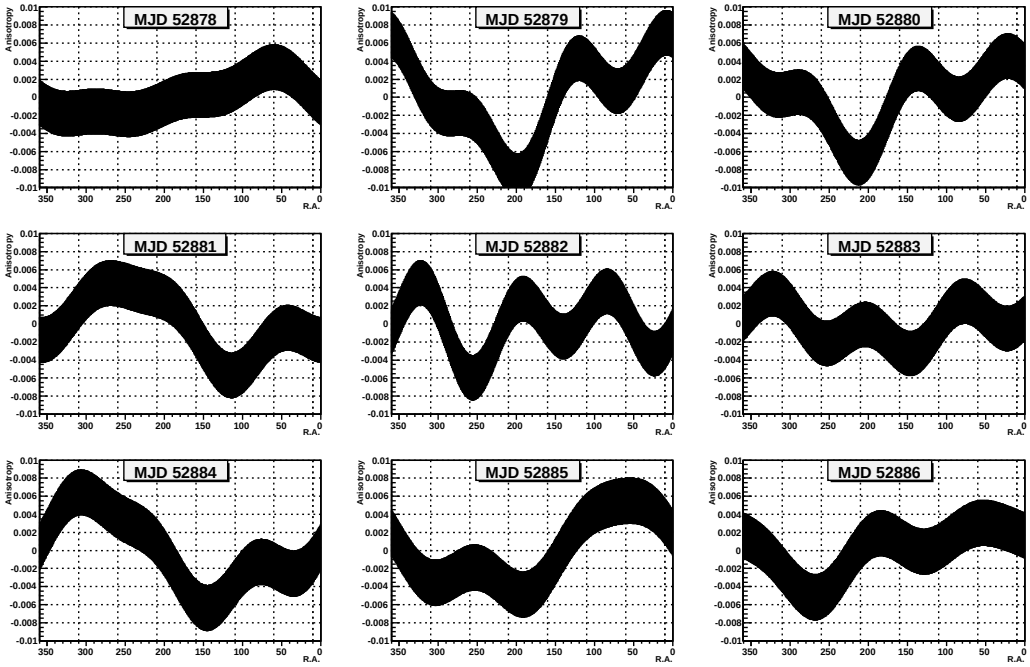

Figure 5.23: Anisotropy analysis for dec. $\sim 36^{\circ}$ for a 9 consecutive day sample. The width of the lines correspond to the statistical errors on the fit function. The scale is $\pm 1\%$. These plots show the large daily variations present due to weather effects.

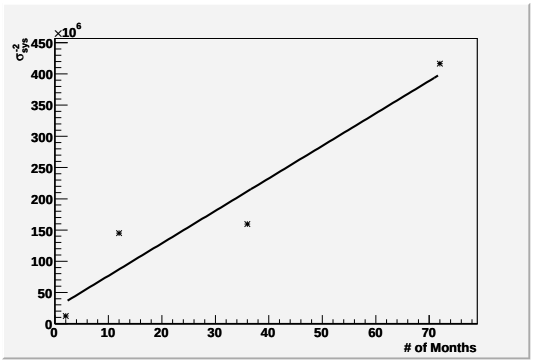

Figure 5.24: Plot showing σ_{sys}^{-2} vs. number of months calculated using real data. The dashed line is the extrapolation of the error according to the expected $1/\sqrt{N_{days}}$ behavior.

5.0.7 Temporal Evolution

The time evolution of the signal in the central-deficit region is an unexpected result and requires a number of checks to rule out the possibility that it is simply an artifact of time dependent detector effects. This section will address this concern.

For most years of operation, Milagro had a shutdown lasting on the order of ten days during the month of September. To look for a possible effect induced by this down time, a much larger period was removed (Sept- Nov.) from each of the yearly sets. Figure 5.25 shows the time evolution of the yearly data with and without the artificially large amount of down time. The difference in the signals is clearly insignificant.

The trigger threshold of the Milagro detector is not constant over time. There are long term rate variations that can be seen in Figure 5.26. In this plot there can be seen a temporal evolution, however this evolution does not correlate with the observed time dependence of the anisotropy. In order to test for a possible dependence on trigger threshold, the data were constrained by requiring each event to have hit some number of PMTs in the top layer (AS) of the pond in order to be counted. Figure 5.27 shows the average value for six years worth of data in the central-deficit region for eight values of this constraint. As can be seen, the depth is relatively independent of this constraint up to large values. Figure 5.28 shows the time evolution, over six years, for these two particular values (90 and 260) of this constraint. The relevant message of these plots is that although at higher values of the trigger cut the statistics get worse, the anisotropy is stable and the yearly trend does not disappear. Given the large difference between these trigger cuts,

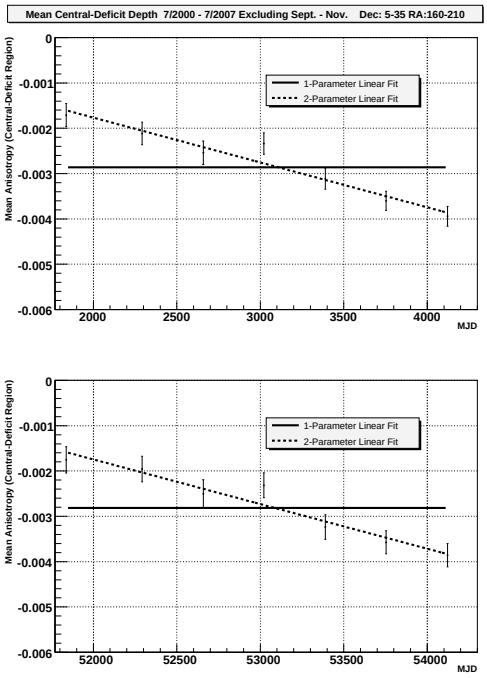

Figure 5.25: Top: Yearly mean central-deficit value with simulated down time of two months (Sept.-Nov.). Bottom: Yearly mean central-deficit value using the full data set (same as Fig. 4.9).

the variation in time cannot be caused by the comparatively small variations in the Milagro trigger.

To check that this effect is in fact strictly a sidereal effect and not something which is a general characteristic of the detector we look at yearly projections of the UT and AST signals. These signals are seen in Figures 5.29 & 5.30 and do not show a consistent year-to-year trend as the sidereal signal does.

The combination of these tests gives good evidence that the monotonic increase in the magnitude of the sidereal anisotropy seen over the seven years cannot be accounted for simply by time dependent detector effects.

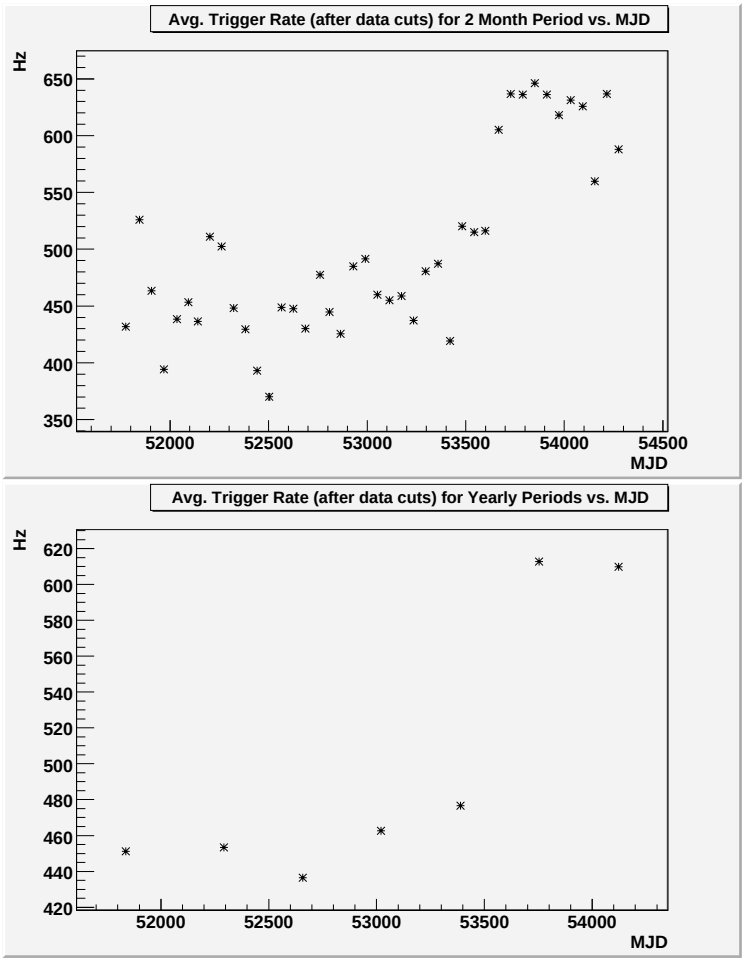

Figure 5.26: Average trigger rate vs. time for two month and yearly periods (top and bottom respectively). The average is calculated including down time and data cuts.

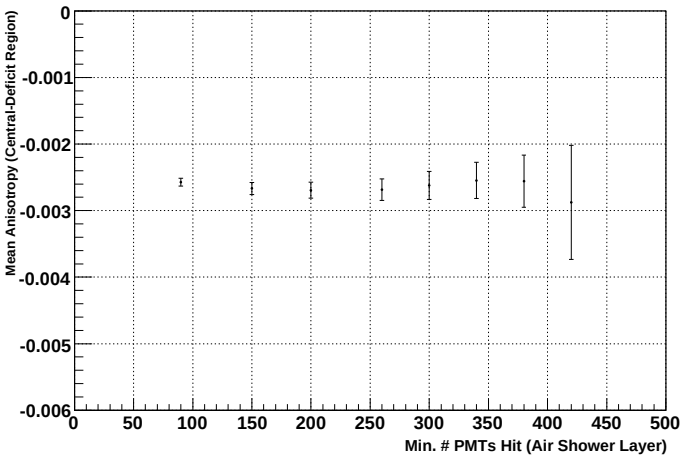

Figure 5.27: Mean central-deficit value for six years of data for events hitting at least some given number of PMTs in the top layer. The error bars are statistical only.

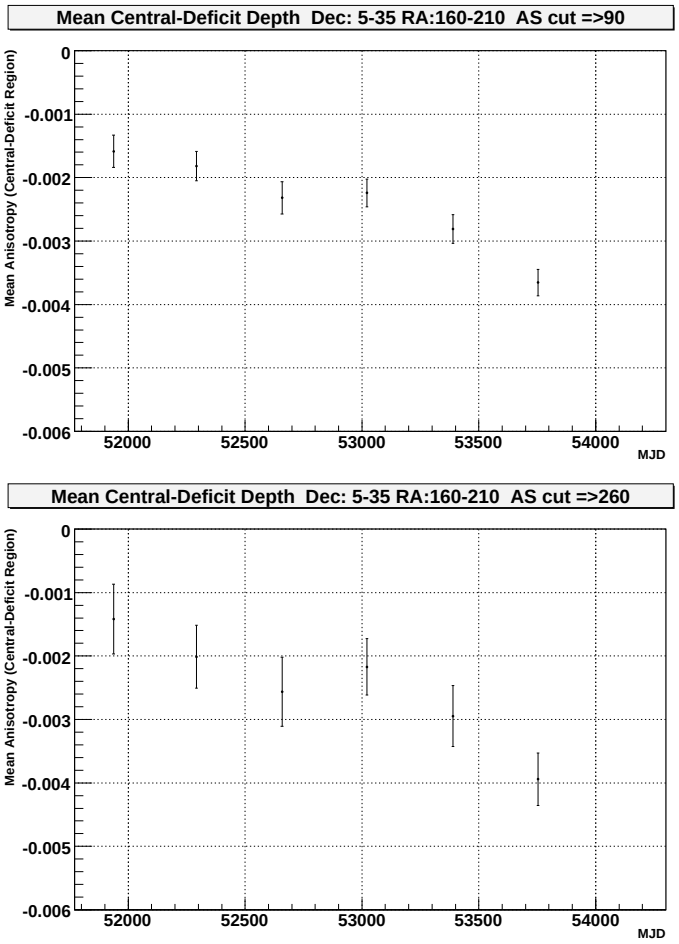

Figure 5.28: Yearly mean central-deficit value for six years for top layer cuts of 90 PMTs and 260 PMTs (top and bottom respectively). The error bars are statistical only.

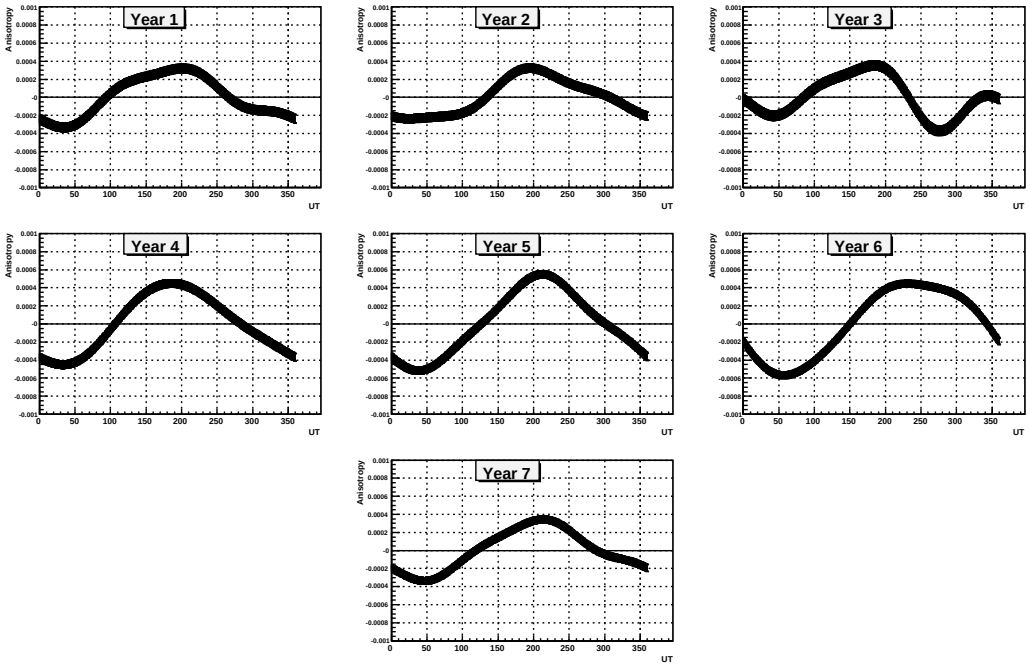

Figure 5.29: Yearly profiles of anisotropy vs. UT obtained by analyzing the projection of the 18 dec. bands.

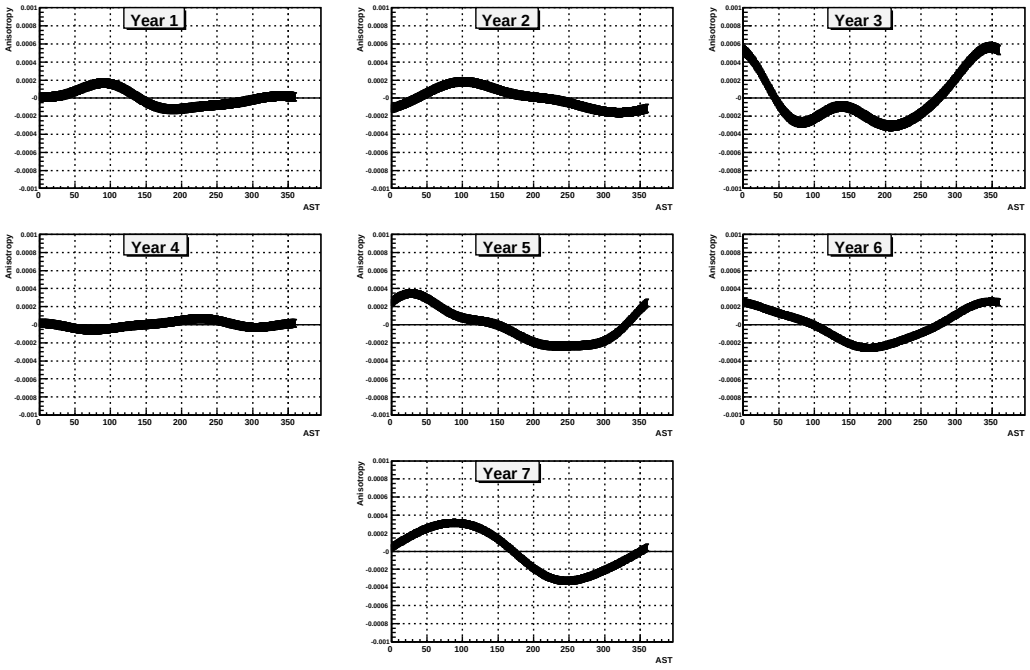

Figure 5.30: Yearly profiles of anisotropy vs. AST obtained by analyzing the projection of the 18 dec. bands.

5.0.8 Universal Time Energy Dependence

The energy dependence of the sidereal signal examined in Section 4.3 shows a specific change in the value of the anisotropy in the central-deficit region over time. It is therefore also important to look at the energy dependence of the UT signal to be sure that this change is not a detector effect. Figure 5.31 shows an analysis of the 18 declination band projection for the eight ln(fOut) bins used in the energy analysis of the sidereal signal. In this case looking at the value of the anisotropy at the maximum, which for the Compton-Getting effect is calculated to be 3.8×10^{-4} and is energy independent, does not show a significant dependence on this parameter.

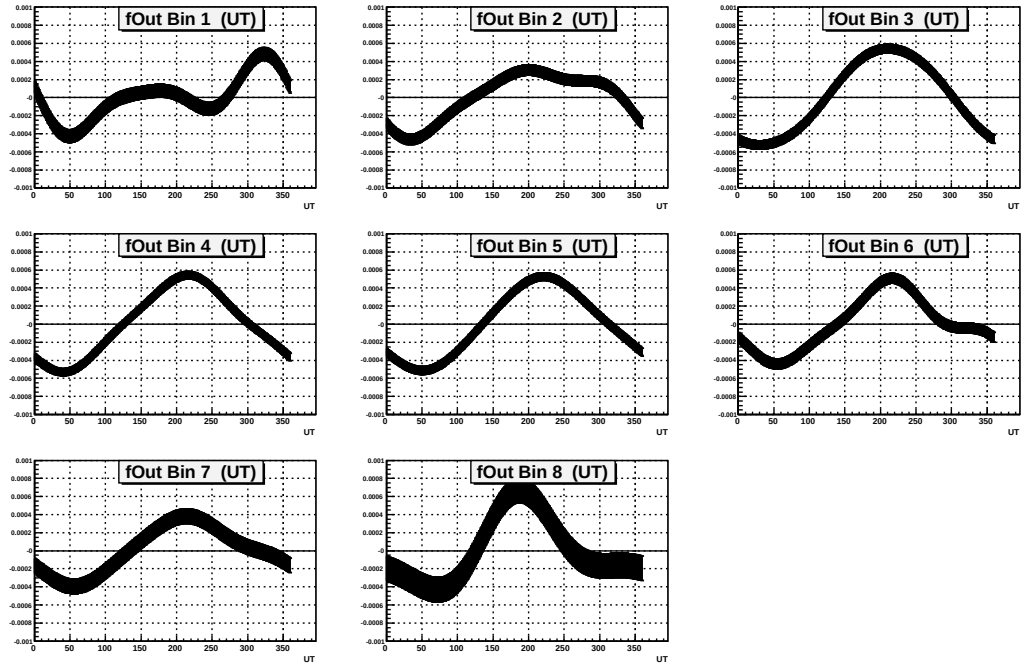

Figure 5.31: Anisotropy vs. UT for the last four years of data created by analyzing the projection of the 18 dec. bands for the eight fOut bins defined in Section 4.3.

5.0.9 Coronal Mass Ejections

One possible effect that may obscure our analysis which we studied was coronal mass ejections(CMEs). CMEs are thought to produce large anisotropies as they pass around the earth. To examine the effect on our data we picked three large CMEs that happened within our data set. The dates of these CMEs are: 4/12/2001, 10/29/2003 and 1/20/2005. When a CME reaches the earth there is what is called a Forbush decrease. This can be seen clearly in neutron monitor data as a decrease in neutron rates starting about 12 hours before the event followed by a period of relaxation lasting for about 36 hours. We cut out the section corresponding to the large deviations in neutron rates as read off of the data from the Jung Frau Joch monitoring station. There were no noticeable changes to the large scale anisotropy. From this we determined that it was acceptable to not correct our data for CMEs. Looking at the data that was excised in the case of the 2001 CME however, there was evidence of a significant difference in the anisotropy before and after the event. This is something worth investigating further.

Chapter 6

Conclusions

Results have been presented of a harmonic analysis of the large scale cosmic-ray anisotropy for the observational period between July 2000 to July 2007. A 2-D map of anisotropy projections in r.a. was generated using the 9.59×10^{10} cosmic-ray events collected during this period, which have a median energy of 6 TeV. The dominant feature is a central-deficit region of depth $(-2.85 \pm 0.06$ stat. ± 0.08 syst.$) \times 10^{-3}$ in the direction of the Galactic North Pole with a range in declination of -10 to 45 degrees and 150 to 225 degrees in right ascension.

Observations of the sidereal anisotropy at TeV energies done by previous experiments have identified two coincident regions of interest: an excess located at $\sim 75^{\circ}$ r.a. or "tail-in" anisotropy, and a deficit at $\sim 200^{\circ}$ r.a. or "loss-cone" anisotropy. Both of these regions are consistent with the observation presented here. The "loss-cone" is coincident with the central-deficit region seen in this analysis. The "tail-in" region is more clearly defined in another Milagro analysis sensitive to features with smaller extent in r.a. Also, a number of experiments have done harmonic analy-

ses of the anisotropy. Table 6.1 shows the first harmonic results for a few of these experiments.

Experiment	Amplitude ($\times 10^{-3}$)	Phase (Deg.)	Energy (TeV)
Poatina (um) [31]	0.81 ± 0.13	60.0 ± 9.0	1
Baksan (um) [32]	1.20 ± 0.20	30.0 ± 7.5	3
Milagro (as)	1.99 ± 0.01	9.0 ± 0.4	6
Super-K (um) [21]	0.53 ± 0.12	40.0 ± 14.0	10
Tibet (as) [33]	1.13 ± 0.07	24.0 ± 3.0	12
Mt. Norikura (as) [22]	0.74 ± 0.04	12.0 ± 4.5	15
MACRO (um) [34]	1.10 ± 0.36	-12.0 ± 19.5	30
Musala (as) [35]	1.05 ± 0.30	51.0 ± 15.0	60
EAS-TOP (as) [36]	0.36 ± 0.04	64.5 ± 7.5	100

Table 6.1: Amplitudes and phases of fundamental harmonic fits to the sidereal cosmic-ray anisotropy for a sample of experiments at different energies. The amplitudes are divided by $cos(dec.)$ to account for differences in the declination of each experiment. The abbreviations after the experiment names indicated the type of detector: um - for an underground muon detector and as - for an extensive air shower detector.

The energy dependence of the signal in the central-deficit region has been studied and shows evidence that the spectral index differs from that of the nominal cosmic-ray background at the level of 5σ. The spectrum of this anisotropy was modeled as a broken power-law and the best fit to data gives a break energy of $E_{break} = 2^{+1.3}_{-1.0}$ TeV, $\delta = -2.7^{+2.1}_{-0.3}$ for energies below the break, and $\delta = 0.1 \pm 0.07$ for energies above the break where δ is the difference between the spectral indices of the nominal cosmic-ray background and the anisotropy. The determination of these parameters is however not very significant given the poor energy resolution.

The signal expected due to the Galactic Compton-Getting effect cannot be identified given the large contribution from the observed signal in the central region. It may be possible to make a more definitive statement about this effect with a mea-

surement at higher energies since the Compton-Getting effect is energy independent while the anisotropy in the central-deficit region appears to decrease with increasing energy.

The Compton-Getting effect expected from the Earth's motion around the sun is observed as a dipole with a maximum amplitude of $(3.6 \times 10^{-4}$ at 7.5 hr universal time. This maximum occurs 1.5 hrs later than expected and requires more study to understand possible systematic effects.

A unique result to this analysis is the observation of a strengthening, by a factor of two, of the depletion in the central-deficit region over this seven year period. It is noted that the minimum anisotropy occurs at solar maximum, and the maximum anisotropy occurs as the solar minimum approaches. The simplest hypothesis for this time dependence is that when solar activity is high, the heliosphere has the capability to isotropize cosmic-rays with higher efficiency than when solar activity is low. It is as of yet unclear how the heliosphere can have such an effect on cosmic-rays at TeV energies. One possibility for this observation is that, given the poor energy resolution, this is simply an effect coming from low energy events. Collecting more years of data is an obvious step in seeing if the correlation between the solar cycle and anisotropy magnitude holds. A large improvement in energy determination is also necessary in order to help understand the time dependence and the possible origins of this anisotropy.

Appendix A

Monte Carlo of Anisotropy for Analysis Method Tests

In order to better understand the analysis method and possible systematic effects, it was necessary to develop a monte carlo (MC) method which would simulate data coming from the Milagro detector with the proper statistics and an arbitrary, user defined anisotropy.

This MC takes two inputs: a 2-D histogram of the detector acceptance, and a 2-D histogram of the desired anisotropy. The detector acceptance histogram is used to ensure that the MC events have the same declination and hour angle dependencies that the Milagro detector has over a 30 minute period of time. This histogram is generated by averaging all of the 48 half-hour dec. vs. HA histograms described in Section 3.4 for data accumulated over seven years. This averaging is done to remove any signal (forward-backward asymmetry) that is present in any given 30 minute interval while retaining any inherent detector asymmetries.

The second histogram used as input is simply a 2-D anisotropy map as seen throughout this work. One may use the output from an analysis of actual data or create a unique anisotropy.

These histograms are normalized and treated as probability distributions as in any MC. The way events are generated is by stepping though time in five minute intervals. In each interval a uniform distribution of random time stamps (in UT) is generated. For each time stamp, an event is created with a random dec. and r.a. (also uniformly distributed). The r.a. of this event is converted to an HA and checked against the acceptance histogram. Passing this check, the event is then checked against the anisotropy map. If the event passes both tests it is treated as any normal event would be and goes through the analysis as described starting in Section 3.4.

In order to have the correct statistics, this generation of events continues until the number of passing events collected over the five minute period corresponds to the average Milagro trigger rate ($\sim$ 1500Hz). This rate may be fixed or randomly varied if so desired. This process then continues for each five minute interval present in the desired number of simulated days. The performance of this MC can be seen in Section 5.0.1.

Bibliography

[1] P. Sokolsky, *Introduction to Ultrahigh Energy Cosmic Ray Physics* (Westview Press, 2004).

[2] `http://interstellar.jpl.nasa.gov/interstellar/probe/interaction/interaction.html`.

[3] T. C. Weeks, *High Energy Astrophysics* (Chapman and Hall, London, 1972).

[4] L. Fleysher, *Search for Relic Neutralinos with Milagro*, PhD thesis, New York University, 2003.

[5] `http://astronomy.swin.edu.au/cosmos/E/Equatorial+Coordinate+System`.

[6] R. Schlickeiser, *Cosmic Ray Astrophysics* (Springer, 2002).

[7] M. Shapiro and L. Koch-Miramond, Space Science Reviews **38**, 183 (1984).

[8] C. Grupen, *Astroparticle Physics* (Springer, 2005).

[9] A. W. Strong, I. V. Moskalenko, and V. S. Ptuskin, Annual Review of Nuclear and Particle Science **57**, 285 (2007), arXiv:astro-ph/0701517.

[10] F. C. Jones, A. Lukasiak, V. Ptuskin, and W. Webber, ApJ **547**, 264 (2001), arXiv:astro-ph/0007293.

[11] V. S. Berezinskiĭ *et al.*, *Astrophysics of Cosmic Rays* (North-Holland, 1990).

[12] M. Simon, In *DuVernois, M.A. (ed.): Topics in cosmic-ray astrophysics*.

[13] V. Ptuskin, F. Jones, E. Seo, and R. Sina, Adv. Space Res. **37**, 4 pages (2006).

[14] A. D. Erlykin and A. W. Wolfendale, Astroparticle Physics **25**, 183 (2006), arXiv:astro-ph/0601290.

[15] S. Thoudam, Mon. Mot. R. Astron. Soc. **378**, 48 (2007), arXiv:astro-ph/0703176.

[16] R. Schlickeiser, U. Dohle, R. C. Tautz, and A. Shalchi, ApJ **661**, 185 (2007).

[17] A. H. Compton and I. A. Getting, Phys. Rev. **47**, 817 (1935).

[18] L. J. Gleeson and W. I. Axford, Astrophys. & Space Sci. **2**, 431 (1968).

[19] T. Antoni *et al.*, ApJ **604**, 687 (2004), arXiv:astro-ph/0312375.

[20] M. Amenomori *et al.*, Science **314**, 439 (2006).

[21] G. Guillian *et al.*, Phys. Rev. D **75**, 17 pages (2007).

[22] K. Nagashima *et al.*, Il Nuovo Cimento C **12**, 54 (1989).

[23] M. Rao and B. Sreekantan, *Extensive Air Showers* (World Scientific, 1997).

[24] `http://www-ik.fzk.de/corsika/`.

[25] http://geant4.web.cern.ch/geant4/.

[26] A. Abdo, *Discovery of Localized TeV Gamma-Ray Sources and Diffuse Gamma-Ray Emission from the Galactic Plane with Milagro Using a New Background Rejection Technique*, PhD thesis, Michigan State University, 2007.

[27] B. Allen *et al.*, Energy Spectrum of Gamma Rays from the Crab Nebula from 1 to 100 TeV with the Milagro Telescope, in *30th International Cosmic Ray Conference, Merida, Mexico, July 3-11*, 2007.

[28] A. D. Panov *et al.*, (2006), astro-ph/0612377.

[29] H. R. Band *et al.*, Phys. Rev. Lett. **59**, 415 (1987).

[30] R. Atkins *et al.*, Phys. Rev. Lett. **95**, 251103 (2005), astro-ph/0502303.

[31] K. B. Fenton, A. G. Fenton, and J. E. Humble, Sidereal Variations at High Energies - Observations at Poatina, in *24th International Cosmic Ray Conference, Tsukuba, Japan, August 28 - September 8*, 1995.

[32] Y. M. Andreyev *et al.*, Cosmic Ray Sidereal Anisotropy Observed by Baksan Underground Muon Telescope, in *20th International Cosmic Ray Conference, Moscow, Russia, August 2 - 15*, 1987.

[33] M. Amenomori *et al.*, ApJ Letters **626**, L29 (2005).

[34] M. Ambrosio *et al.*, Phys. Rev. **D67**, 042002 (2003), astro-ph/0211119.

[35] T. Gombosi *et al.*, Nature **255**, 687 (1975).

[36] M. Aglietta *et al.*, The Cosmic Ray Anisotropy between 10^{14} and 10^{15} eV, in *28th International Cosmic Ray Conference, Tsukuba, Japan, July 31 - August 7*, 2003.